Modelling glacier mass-balance and climate sensitivity in a context of sparse observations: application to Saskatchewan Glacier, western Canada ~~Mass balance modelling and climate sensitivity of Saskatchewan Glacier, western Canada~~

Christophe Kinnard[1], Olivier Larouche[1,2], Michael N. Demuth[3~~2~~], Brian Menounos[4~~3~~]

[1] Centre de Recherche sur les Interactions Bassins Versants—Écosystèmes Aquatiques (RIVE), Département des Sciences de l'Environnement, Université du Québec à Trois-Rivières, Québec, G8Z 4M3, Canada ~~Département des Sciences de l'environnement, Université du Québec à Trois Rivières, Trois-Rivières, G87R7, Canada~~
[2] Centre d'Études Nordiques (CEN), Québec, G1V 0A6, Canada

[3~~2~~] Geological Survey of Canada; currently, University of Saskatchewan Cold Water Laboratory, Canmore, T1W 3G1, Canada
[4~~3~~] Natural Resources and Environmental Studies Institute and Geography, University of Northern British Columbia, Prince George, British Columbia, Canada

Correspondence to: Christophe Kinnard (christophe.kinnard@uqtr.ca)

Abstract. Glacier mass balance models are needed at sites with scarce long-term observations to reconstruct past glacier mass balance and assess its sensitivity to future climate change. In this study, North American Regional Reanalysis (NARR) data ~~are~~ were used to force a physically-based, distributed glacier mass balance model of Saskatchewan Glacier for the historical period 1979-2016 and assess it sensitivity to climate change. A two-year record (2014-2016) from an on-glacier automatic weather station (AWS) and ~~a homogenized~~ historical precipitation records from nearby permanent weather stations were used to downscale air temperature, relative humidity, wind speed, incoming solar radiation and precipitation from ~~the nearest~~ NARR ~~gridpoint~~ to the ~~glacier~~station sites ~~AWS site~~. The model was run with fixed (1979, 2010) and time-varying (dynamic) geometry using a multi-temporal digital elevation model ~~(DEM)~~ dataset. The model showed a good performance against recent (2012-2016) direct glaciological mass balance observations as well as with cumulative geodetic mass balance estimates. The simulated mass balance was little sensitive to the NARR spatial interpolation method, as long as station data was used for bias correction. The simulated mass balance was however ~~showed a large sensitivity~~ sensitive to the biases in NARR precipitation and ~~solar radiation~~air temperature, as well as to the prescribed precipitation lapse rate and ice aerodynamic roughness lengths, showing the importance of constraining these two parameters with ancillary data. The glacier-wide simulated energy balance regime showed a large contribution (57%) of turbulent (sensible and latent) heat fluxes to melting in summer, higher than typical mid-latitude glaciers in continental climates, which reflects the local humid 'icefield weather' of the Columbia Icefield. ~~The difference between the static (1979) and dynamic simulations showed small differences (mean = 0.06 m w.e. a^{-1} or 1.5 m w.e. over 37 yrs), indicating minor effects of elevation changes on the glacier specific mass balance.~~ The static mass balance sensitivity to climate was assessed for prescribed changes in regional mean air temperature between 0 to 7 °C and precipitation

between -20 to +20%, which comprise the spread of ensemble ~~IPCC representative concentration pathways~~RCP climate scenarios for the mid (2041-2070) and late (2071-2100) 21st century. The climate sensitivity experiments showed that future changes in precipitation would have a small impact on glacier mass-balance, while the temperature sensitivity increases with warming, from -0.65 to -0.93 m w.e. °C^{-1}. The mass balance response to warming was driven by a positive albedo feedback (44%), followed by direct atmospheric warming impacts (24%), a positive air humidity feedback (22%) and a positive precipitation phase feedback (10%). ~~Increased melting accounted for 90% of the temperature sensitivity while precipitation phase feedbacks accounted for only 10%. Roughly half of the melt response to warming was driven by a positive albedo feedback, in which glacier albedo decreases as the snow cover on the glacier thins and recedes earlier in response to warming, increasing net solar radiation fluxes. About one quarter of the melt response to warming was driven by latent heat energy gains (positive humidity feedback).~~ Our study underlines the key role of albedo and air humidity in modulating the response of winter-accumulation type mountain glaciers and upland icefield-outlet glacier settings to climate.

1 Introduction

Global warming is expected to cause reduced snowfall in cold regions, earlier snowmelt in spring and a longer ice melt period in summer (e.g., Barnett et al., 2005)~~ {Barnett, 2005 #98}~~. ~~(Aygün et al., 2020a{Barnett, 2005 #98}).~~ Even if ~~the amount of~~ precipitation remains unchanged, warming alone will reduce snow and ice storage in catchments, affecting the seasonality of river streamflow regimes and accelerating water losses to the ocean (Escanilla-Minchel et al., 2020; Huss et al., 2017; Huss and Hock, 2018)~~ {Escanilla-Minchel, 2020 #44} {Escanilla-Minchel, 2020 #44}~~. ~~Glaciers act as natural reservoirs in mountain regions, contributing fresh water during periods of drought and buffering the hydrological regimes of rivers against extreme climate variability (Fountain and Tangborn, 1985; Jansson et al., 2003).~~ The transition from a nivo-glacial to a more pluvial river regime in response to warming ~~would~~ will change the timing and magnitude of floods, leading to altered patterns of erosion and sediment deposition and impacting biodiversity and water quality downstream (Déry et al., 2009; Huss et al., 2017). The impacts of the progressive loss of ice and snow surfaces and resulting alterations of the hydrological cycle can reach well beyond the glacierized catchments, affecting agriculture (Barnett et al., 2005; Comeau et al., 2009; Milner et al., 2017; Schindler and Donahue, 2006)~~ (!!! INVALID CITATION !!! (Barnett et al., 2005; Comeau et al., 2009; Milner et al., 2017; Schindler and Donahue, 2006))~~, fisheries (Dittmer, 2013; Grah and Beaulieu, 2013; Huss et al., 2017), hydropower and general ecological integrity (Huss et al., 2017). ~~Glaciers and ice caps (GIC) mass loss have also contributed to sea level rise over the last decades, with recent estimates of 0.48 ± 0.1 mm a^{-1} between 1992 and 2016 for GIC excluding Greenland and Antarctica peripheral ice caps and glaciers (PGIC) (Bamber et al., 2018), and 0.5 ± 0.4 mm a^{-1} (with PGIC) or 0.4 ± 0.3 mm a^{-1} (without PGIC) between 1961 and 2016 (Zemp et al., 2019). Mass loss from GIC could increase sea-level by 0.215 ± 0.021 m at the end of the 21st century under high-end climate change scenarios (Shannon et al., 2019), exacerbating coastal inundations and forcing population movement in several areas of the world (Cazenave and Cozannet, 2014).~~

The surface mass balance is the prime variable of interest to monitor and project the state of glaciers and their hydrological contribution under global warming scenarios (Hock and Huss, 2021). However, o~~O~~nly a few glaciers around the world have long term direct mass balance observations, because these measurements are time consuming and logistically complicated. For example, only 30 glaciers have uninterrupted mass balance records since 1976 (Zemp et al., 2009). ~~(Zemp et al., 2015) because these measurements are time consuming and logistically complicated.~~ Geodetic estimates provide a complementary picture of cumulative mass changes for a greater number of glaciers worldwide, but their coarser sampling interval (typically > 5years) makes their link with climate less direct (Cogley, 2009; Cogley and Adams, 1998; Menounos et al., 2019). For this reason, models are often ~~used~~ used to extrapolate scarce measurements, estimate unsampled glaciers and to assess glacier mass balance sensitivity to climate. ~~Several types of mass balance models have been used, whose complexity varies depending on the processes represented, the input data required and the spatial and temporal resolution of the models. The so-called~~

~~‘~~T~~t~~emperature-index~~’ or ‘degree-days’~~ models, which use ~~only~~ air temperature as sole predictor of ablation (Hock, 2003), ~~. These models~~ have been extensively used to project regional and global glacier mass balance under climate change scenarios, due to their simple implementation and readily available global precipitation and temperature forcing data (Hock et al., 2019; Huss and Hock, 2015; Marzeion et al., 2012; Radić et al., 2014). Enhanced ~~temperature-index models~~temperature-index models, which ~~-~~include additional predictors such as potential (Hock, 1999) or net (Pellicciotti et al., 2005) solar radiation~~, to estimate melt. They offer a useful trade-off between the simple temperature-index models and the more complex energy-balance models~~ have also been ~~used and~~ shown to ~~and have been shown to~~ improve glacier melt simulation and to be ~~be~~ more transferable outside their calibration interval (Gabbi et al., 2014; Réveillet et al., 2017). ~~Simple~~ These empirical models contain few parameters ~~that~~ which simplifies their application, but ~~but they~~ they must be calibrated ~~with~~ on observations, which makes model extrapolation ~~. The extrapolation of parameters in time and space, i.e.,~~ in a different climate ~~outside their calibration conditions~~questionable ~~, is therefore questionable~~ (Carenzo et al., 2009; Gabbi et al., 2014; Hock et al., 2007; Wheler, 2009). ~~Alternatively~~Hence,~~,~~ spatially-distributed, energy balance ~~physically-based~~ models that ~~rely on energy balance calculations~~ better represent the physical processes ~~which drive~~driving glacier ablation ~~and~~ are ~~thus~~ more suited to simulate glacier mass balance outside of present-day climate conditions (Hock et al., 2007; MacDougall and Flowers, 2011), given that accurate forcing data is available (Réveillet et al., 2018). ~~to explicitly account for all energy exchanges between the glacier surface and atmosphere~~ ~~This makes physically-based distributed models an ideal tool to estimate glacier climate sensitivity, i.e., the mass balance response to a change in climate conditions (Braithwaite and Raper, 2002; Che et al., 2019; Ebrahimi and Marshall, 2016; Engelhardt et al., 2015; Hock et al., 2007; Klok and Oerlemans, 2004; Oerlemans et al., 1998).~~

Energy-balance glacier models ~~. They are more complex~~ require several input observations and contain ~~several~~ multiple parameters that are sometimes difficult to measure or estimate ~~and require several input observations~~ (e.g. Anderson et al., 2010; Anslow et al., 2008; Arnold et al., 1996; Ayala et al., 2017; Gerbaux et al., 2005; Hock and Holmgren, 2005; Klok and Oerlemans, 2002; Marshall, 2014; Mölg et al., 2008). ~~However, these models better represent the physical processes which drive glacier ablation and are thus more suited to simulate glacier mass balance outside of present-day climate conditions (Hock et al., 2007; MacDougall and Flowers, 2011), given that accurate forcing data is available (Réveillet et al., 2018). This makes physically-based distributed models an ideal tool to estimate glacier climate sensitivity, i.e., the mass balance response to a change in climate conditions (Braithwaite and Raper, 2002; Che et al., 2019; Ebrahimi and Marshall, 2016; Engelhardt et al., 2015; Hock et al., 2007; Klok and Oerlemans, 2004; Oerlemans et al., 1998).~~

~~Glaciological~~Glacier mass balance models have been mostly forced with observations from automatic ~~meteorological~~ weather stations (AWS) on, or near glaciers. However, the management of weather stations networks in mountainous areas poses financial and logistical challenges. At sites with scarce or missing data, outputs from meteorological forecasting models (Bonekamp et al., 2019; Mölg et al., 2012; Radic et al., 2018), regional climate models (Machguth et al., 2009; Paul and

Kotlarski, 2010) and ~~downscaled~~ reanalysis data (Clarke et al., 2015; Hofer et al., 2010; Østby et al., 2017; Radić and Hock, 2006) ~~have~~ have been ~~been~~ used to force ~~physically-based~~glacier models. In particular, climate reanalyses provide consistent and readily available gridded estimates of past atmospheric states at sub-daily intervals, which constitute a useful alternative to drive glaciological and hydrological models in data-scarce regions (Hofer et al., 2010). Reanalyses ~~Reanalyses~~ are produced by retrospective numerical weather model simulations that assimilate long-term and quality-controlled observations. ~~and provide consistent gridded estimates of past atmospheric states at sub-daily intervals. They offer useful alternatives to drive glaciological and hydrological models in data-scarce regions (Hofer et al., 2010). However, reanalysis data are typically produced at longer time intervals and coarser spatial resolutions than observations, e.g. from 4-times daily and ~210 km for NCEP/NCAR Reanalyses (Kistler et al., 2001), to hourly and ~30 km for the recent ERA-5 product (Hersbach and Dee, 2016).~~ Regional products like the North American Regional Reanalysis (NARR) ~~were~~ have been developed to enhance the spatial and temporal resolution of reanalyses at the continental scale (Mesinger et al., 2006). Statistical downscaling of reanalysis data using on- or near-glacier meteorological observations ~~has been used~~is necessary ~~in order~~ to reduce biases resulting from this temporal and spatial scale mismatch as well as from structural and parameterizations errors in the reanalysis model (Hofer et al., 2010). Several methods can be used to correct those errors, such as a simple bias shift toward observations (scaling or delta method) or the matching of two probability distributions (e.g., quantile mapping) (Radić and Hock, 2006; Rye et al., 2010; Teutschbein and Seibert, 2012). This step is crucial, as uncertainties in climate forcing can be the main source of error in mass balance modelling (Østby et al., 2017).

Forcing physically-based glacier models with global or regional gridded climate data introduces additional uncertainties which add up to the structural and parameter uncertainties of the glacier model. In a context of spare in situ observations, the combination of poorly constrained model parameters, biases in meteorological forcings and limited validation data can result in biased long-term mass balance reconstructions and an incorrect appraisal of glacier-climate relationships (Anslow et al., 2008; Machguth et al., 2008; Zolles et al., 2019). A careful application, validation and sensitivity analysis of the model becomes crucial in these situations. Paradoxically, glaciers with spare or no observations are typically those where longer-term model reconstructions of mass balance are often most sought (e.g. Kinnard et al., 2020; Kronenberg et al., 2016; Sunako et al., 2019)~~{Kinnard, 2020 #133}~~. Saskatchewan Glacier (52.15 °N, -117.29 °E),~~,~~ one of the main outlet glaciers of the Columbia Icefield in the Canadian Rocky Mountains, ~~(52.15 °N, -117.29 °E),~~ is such a glacier with sparse mass balance observations ~~available only since 2012~~, which challenges the application of physically-based mass balance models. The Canadian Rocky Mountains support many glaciers which provide several ecosystem services, such as water provision for hydropower production and agriculture, and constitute iconic features highly valorized for tourism (Anderson and Radić, 2020; Comeau et al., 2009; Moore et al., 2009; Petts et al., 2006; Schindler and Donahue, 2006). However, only a few glaciers have been directly and continuously monitored for mass balance. Peyto Glacier (51.67 °N, -116.53 °E) is the only reference site with a long mass balance record (since 1966), and with the exception of 1996 and 2000, exhibits a consistent trend of negative annual balance beginning since the mid-1970's (Demuth, 2018; Demuth et al., 2006; Demuth and Pietroniro, 2002). Menounos et al. (2019) recently used multisensor digital elevation models from spaceborne optical imagery to calculate a mean mass balance of -0.410 ± 0.213 m w.e. a^{-1} for the 2000-2018 period in the Canadian Rocky Mountains, with accelerated mass loss between 2000-2009 and 2009-2018. A large-scale modelling study by Clarke et al. (2015) showed that the volume of western Canada's glaciers could decrease by more than 90% from 2005 to 2100 in the Canadian Rockies. Clarke et al. (2015) concluded that the main source of uncertainty in their simulations of glacier evolution at the mountain range scale was not the parameterisation of glacier flow but rather the simulation of surface mass balance. Thus, accurate models of surface mass balance are still needed at the scale of individual glaciers, to extend, and give context to, sparse mass balance observations as well as to characterize the mass balance sensitivity to climate change.

Well-validated glacier models are an ideal tool to estimate glacier climate sensitivity, i.e., the mass balance response to a change in climate conditions (Braithwaite and Raper, 2002; Che et al., 2019; Ebrahimi and Marshall, 2016; Engelhardt et al., 2015; Gerbaux et al., 2005; Hock et al., 2007; Klok and Oerlemans, 2004; Mölg et al., 2008; Oerlemans et al., 1998; Yang et al., 2013). These and other studies have reported on the varying sensitivity of mass-balance to warming air temperatures, however often without unraveling the respective contributions of atmospheric warming, surface feedbacks and precipitation phase feedbacks on the temperature sensitivity. Distributed energy-balance models offer the ability to resolve the changes in energy fluxes that underpin the sensitivity of mass balance to warming air temperatures, shedding light on the driving processes of ablation under a changing climate (e.g. Anderson et al., 2010; Rupper and Roe, 2008).

~~The Canadian Rocky Mountains support many glaciers which provide several ecosystem services, such as water provision for hydropower production and agriculture, and constitute iconic features highly valorized for tourism (Anderson and Radić, 2020; Comeau et al., 2009; Moore et al., 2009; Petts et al., 2006; Schindler and Donahue, 2006). Bolch et al. (2010) compared satellite images from 1985 to 2005 and reported an 11% (± 3.8%) loss of glacier area in western Canada. A later study reported a 30% decrease in glacier surface area, representing 750 km^2 in the central and southern Canadian Rockies over the period 1919-2006 (Tennant et al., 2012), while Demuth et al. (2008) determined glacier area-wise losses of 22% and 36% in the North and South Saskatchewan River Basins respectively between 1978 and 1998. Only a few glaciers have been directly and continuously monitored for mass balance in the Canadian Rockies. Peyto Glacier (51.67 °N, -116.53 °E) is the only reference site with a long mass balance record (since 1966), and with the exception of 1996 and 2000, exhibits a consistent trend of negative annual balance beginning since the mid-1970's (Demuth, 2018; Demuth et al., 2006; Demuth and Pietroniro, 2002). No other long-term records exist to assess mass balance variations and trends in the region. Menounos et al. (2019) recently used multisensor digital elevation models from spaceborne optical imagery to calculate a mean mass balance of 0.410 ± 0.213~~

~~m w.e. a^{-1} for the 2000-2018 period in the Canadian Rocky Mountains, with accelerated mass loss between 2000-2009 and 2009-2018. A recent large-scale modelling study showed that the volume of western Canada's glaciers could decrease by 70% (± 10%) from 2005 to 2100, and could exceed 90% in the Rockies region (Clarke et al., 2015). Clarke et al. (2015) concluded that the main source of uncertainty in their simulations of glacier evolution at the mountain range scale was not the parameterisation of glacier flow but rather the simulation of surface mass balance. Thus, accurate models of surface mass balance are still needed at the scale of individual glaciers, to extend, and give context to, sparse mass balance observations as well as to characterize the mass balance sensitivity to climate change. Saskatchewan Glacier, one of the main outlet glaciers of the Columbia Icefield in the Canadian Rocky Mountains (52.15 °N, -117.29 °E), is such a glacier with sparse mass balance observations available only since 2012, which challenges the application of physically-based mass balance models.~~

This study uses a physically-based, distributed mass balance model in the context of sparse observations to reconstruct long-term glacier mass changes and spatiotemporal patterns of energy and mass fluxes, and to investigate the glacier mass balance sensitivity to climate change. The main issues addressed in this study are (i) how to constrain a physically-based mass balance model forced by reanalysis data in a context of spare observations; and (ii) quantify the ~~While the climate sensitivity of mass-balance has been investigated in several previous studies, the present study addresses the comparatively unexplored topics of the~~ respective contributions of ~~ablation~~ energy balance ~~versus~~ and precipitation phase feedbacks to the ~~temperature~~ mass balance climate sensitivity ~~of glaciers, and of the changing contribution of energy fluxes driving the changes in glacier melt under~~ warming scenarios.

2 Study area

The Columbia Icefield is located in the Canadian Rocky Mountains and straddles the border between Alberta and British Columbia (Figure 1a). The Columbia Icefield is accessible via the Icefields Parkway which is surrounded by two national parks (Jasper, and Banff), which makes the Columbia Icefield a highly-valued cultural and touristic site (Sandford, 2016).

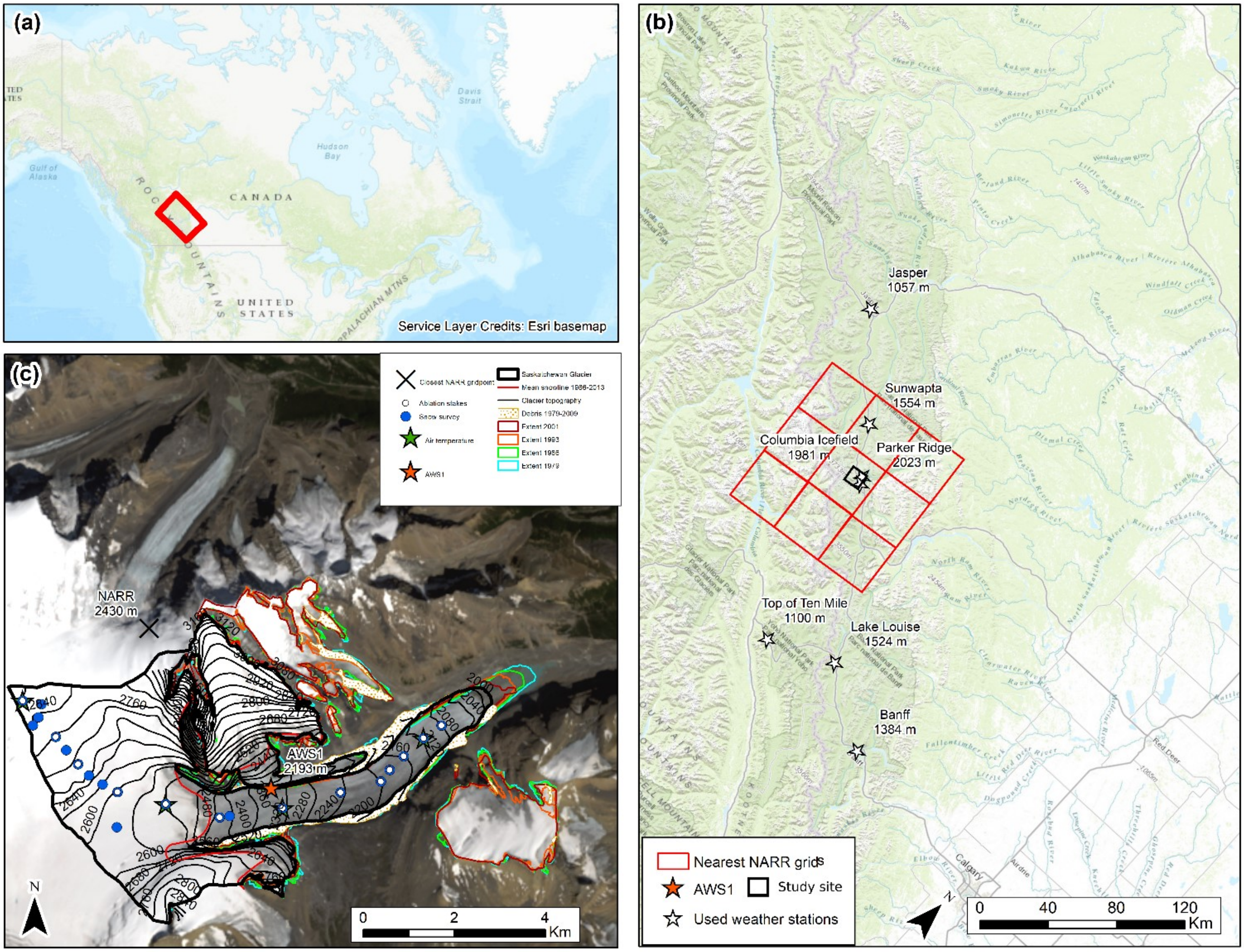

(a)
CANADA
UNITED STATES
Hudson Bay
Gulf of Alaska
Davis Strait
Service Layer Credits: Esri basemap
(b)
Jasper
1057 m
Sunwapta
1554 m
Columbia Icefield
1981 m
Parker Ridge
2023 m
Top of Ten Mile
1100 m
Lake Louise
1524 m
Banff
1384 m
Nearest NARR grids
AWS1
Study site
Used weather stations
0 40 80 120
Km
(c)
Closest NARR gridpoint
Ablation stakes
Snow survey
Air temperature
AWS1
Saskatchewan Glacier
Mean snowline 1986-2013
Glacier topography
Debris 1979-2009
Extent 2001
Extent 1993
Extent 1955
Extent 1979
NARR
2430 m
AWS1
2193 m
0 2 4
Km
N

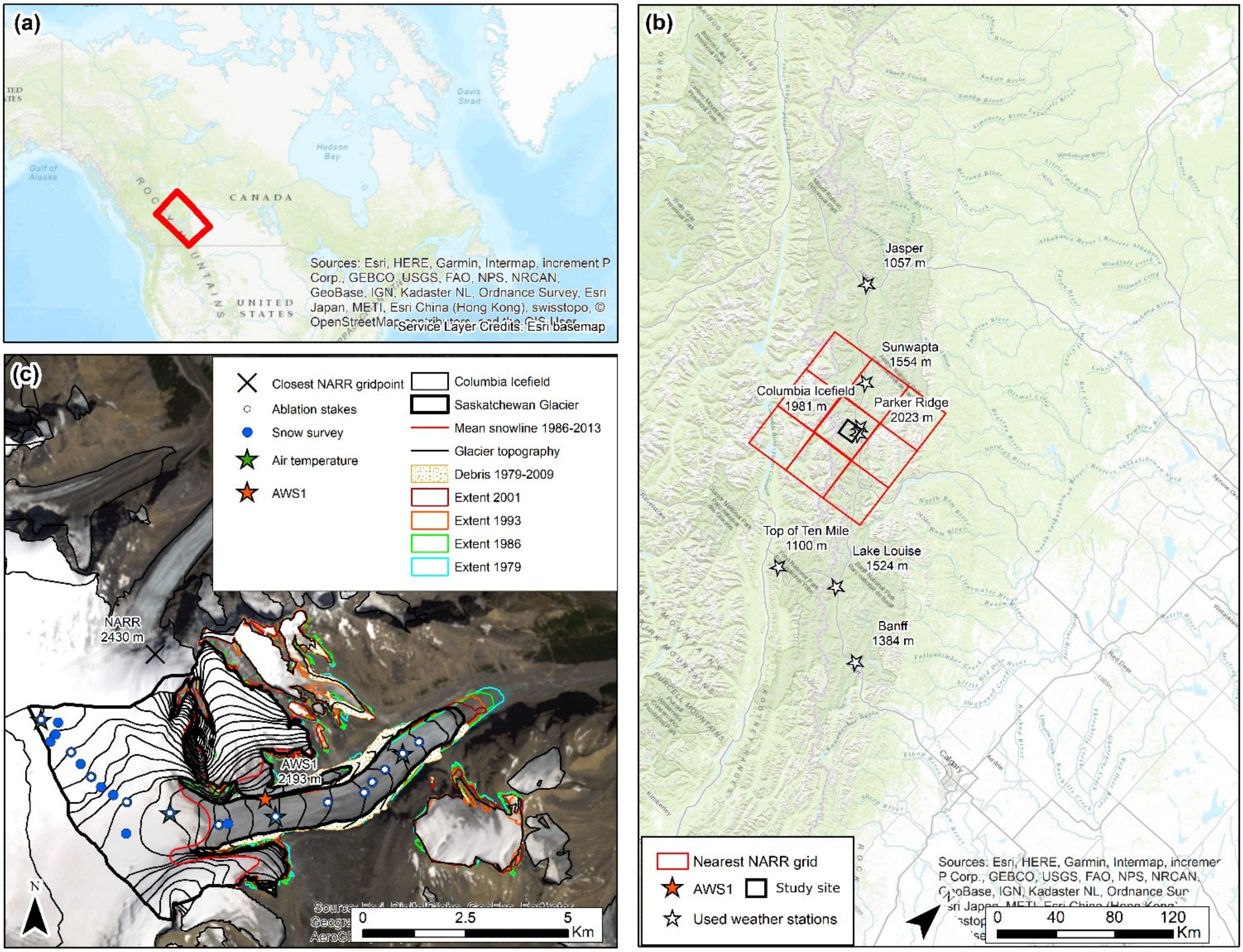
(a)
CANADA
UNITED STATES
Hudson Bay
Davis Strait
Gulf of Alaska
Sources: Esri, HERE, Garmin, Intermap, increment P Corp., GEBCO, USGS, FAO, NPS, NRCAN, GeoBase, IGN, Kadaster NL, Ordnance Survey, Esri Japan, METI, Esri China (Hong Kong), swisstopo, © OpenStreetMap
Service Layer Credits: Esri basemap
(b)
Jasper
1057 m
Sunwapta
1554 m
Columbia Icefield
1981 m
Parker Ridge
2023 m
Top of Ten Mile
1100 m
Lake Louise
1524 m
Banff
1384 m
Nearest NARR grid
AWS1
Study site
Used weather stations
0 40 80 120 Km
(c)
Closest NARR gridpoint
Ablation stakes
Snow survey
Air temperature
AWS1
Columbia Icefield
Saskatchewan Glacier
Mean snowline 1986-2013
Glacier topography
Debris 1979-2009
Extent 2001
Extent 1993
Extent 1986
Extent 1979
NARR
2430 m
AWS1
2193 m
N
0 2.5 5 Km

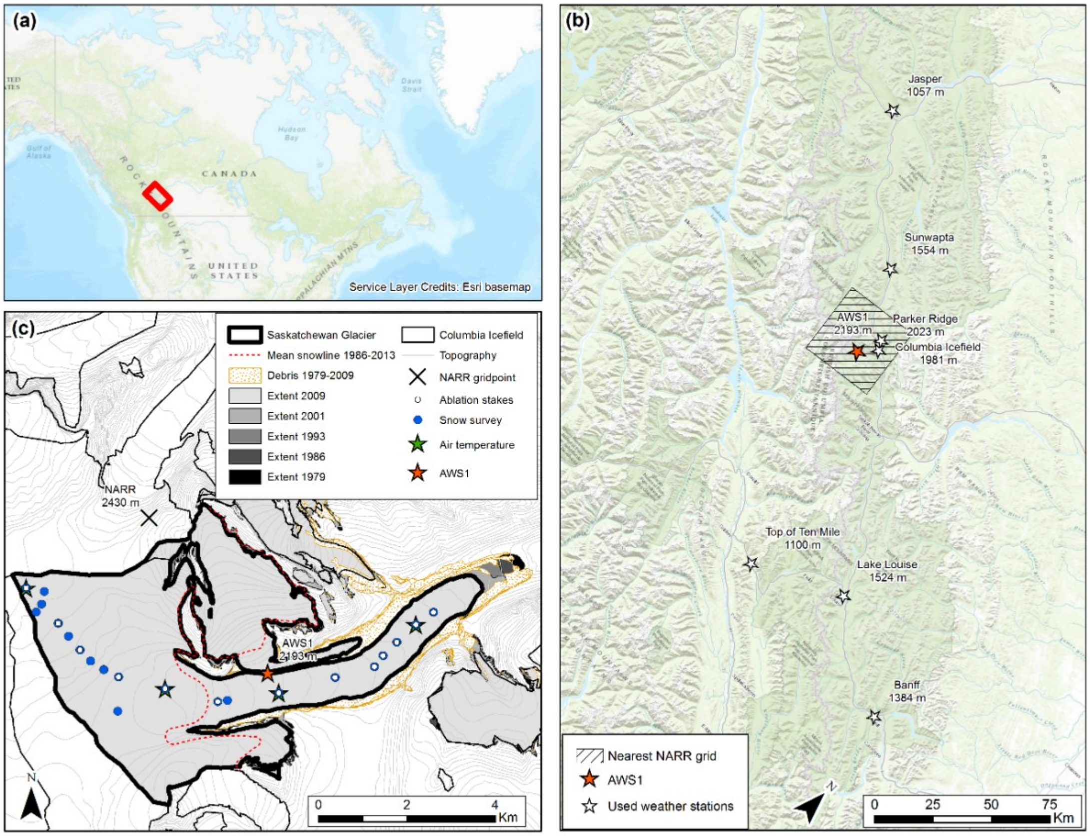

Figure 1. Study area map. (a) Location of the Columbia Icefield in the Canadian Rockies; the red rectangle shows the area of panel b. (b) Weather stations from the permanent network used to calculate temperature and precipitation lapse rate. The ~~nearest~~ nine NARR gridcells~~point~~ closest to Saskatchewan Glacier are shown as ~~(hatched~~ red squares~~) is located directly above neighbouring Athabasca Glacier and encompasses Saskatchewan Glacier~~. (c) Map of Saskatchewan Glacier showing the location of ablation stakes and additional snow survey points, and air temperature sensors used to determine the diurnal lapse rate over the glacier. The mean end of summer snow line position (1986-2013) is shown by a red ~~dotted~~ line. A Landsat 8 scene from August 22, 2013, is used for map background.

The plateau lying at ~2800 meters above sea level (m a.s.l) intercepts moist air masses originating from the Pacific Ocean, which results in large snow accumulation and the formation of glacial ice flowing downward through several outlet glaciers (Demuth and Horne, 2018). The Columbia Icefield is of crucial importance to the region's water budget, as it feeds three different continent-scale watersheds flowing towards the Arctic, Pacific and Atlantic oceans (Figure 1a). The main and largest outlet glaciers are located east of the icefield (Saskatchewan and Athabasca Glacier), draining ~60% of the eastern Columbia Icefield to the North Saskatchewan River (Hudson/Atlantic) and the Sunwapta-Athabasca River (Arctic) (Marshall et al., 2011). Tennant and Menounos (2013) used historical aerial photographs and satellite images to reconstruct the extent and volume changes of the Columbia Icefield. The area of the Columbia Icefield was estimated to be 265.1 ± 12.3 km² in 1919.

By 2009 the icefield had declined by 59.6 ± 1.2 km^2 (22 ± 0.5 %) ~~in 2009 at a rate of -0.66 ± 0.01 km^2 a^{-1}~~. Saskatchewan Glacier is the largest outlet glacier of the icefield and the source of the North Saskatchewan River; i~~I~~ts area was~~, presently covering an area of roughly~~ 23 km^2 in 2017 ~~and ranging in~~with elevations ranging from 1784 to 3322 m, the summit of Mount Snow Dome - the hydrological apex of western Canada (Ednie et al., 2017). Saskatchewan Glacier experienced the greatest absolute area loss among the icefield glaciers, at 10.1 ± 0.6 km^2 ~~a^{-1}~~ since 1919 (Tennant and Menounos, 2013). At the catchment scale, Demuth et al. (2008) reported glacier area-wise losses of 22% for the whole North Saskatchewan River Basins between 1978 and 1998.

3 Data and Methods

3.1 Topographic data

The main topographic data used in this study is a 1-meter resolution digital elevation model (DEM) derived from two WorldView-2 (WV2) satellite stereo images acquired on July 31, 2010, covering the lower glacier and September 18, 2010, covering the upper glacier. The DEM was mosaiced with tiles from the Canadian Digital Surface Model (CDSM) (20-meter resolution) to include all topography adjacent to the glacier that could cast shadows on the glacier. The merged DEM was resampled to 100 meters resolution to allow faster calculation with the mass balance model. The firn area was delimited by a mean snowline delineated from Landsat satellite images from year 1986 to 2013 (Figure 1c). Eighteen cloud-free images were chosen near the end of the hydrological season (September 30) and used to map the mean transient snowline position at the end of summer, which was used as a proxy for the equilibrium line altitude (ELA). Image dates ranged between August 22 and October 2, necessary to find cloud-free images capturing the transient snow line near the end of the ablation period.

To take into account historical glacier contraction in mass balance simulations, multi-temporal DEMs and glacier boundaries from Tennant and Menounos (2013) (hereafter 'TM2013') were used to update the glacier geometry over time in the mass balance model. TM2013 derived DEMs and glacier extents from aerial stereo photographs from 1979, 1986 and 1993. For 1999, they used the Shuttle Radar Topography Mission (SRTM) DEM of February 2000, which they attributed to best represent the glacier surface at the end of the 1999 summer ablation season, due to the penetration of the radar wave in the following year's winter snowpack. The glacier extent in 1999 was derived from the closest cloud-free, 30 m resolution Landsat 5 Thematic Mapper (TM) image in September 2001. The 2009 DEM and glacier extent from TM2013 were derived from Satellite Pour l'Observation de la Terre 5 (SPOT 5) stereo images with a resolution of 2.5 m. Points matched on stereoscopic image pairs were gridded to a 100 m resolution in the ablation area and to 200 m in the accumulation area where low contrasts resulted in a smaller number of elevation points, and varying amounts of data gaps. We re-interpolated all TM2013 DEMs to continuous

100 m resolution using shape-preserving linear interpolation. The 2010 WV2 DEM was used instead of the 2009 DEM from TM2013, which particularly suffered from extensive gaps in the accumulation zone, but the glacier extent of August 2009 was conserved as boundary for the 2010 WV2 DEM. The slope, aspect and sky-view factors were derived from all DEMs to be used as inputs for the mass balance model. A more recent, 2-m resolution DEM was built from a stereo pair of Pleiades Satellite panchromatic images acquired in September 2016 and using the NASA Ames Stereo Pipeline (ASP) (Shean et al., 2016). This DEM was used to update the geodetic mass balance from TM2013 (Supplementary Material). Since the 2010 WV2 DEM has the highest resolution and few gaps, it was considered the most reliable and used for model calibration and climate sensitivity experiments.

Two static ~~static (Huss et al., 2012)mass~~ balance simulations were performed, one using the 1979 DEM as initial boundary condition, and the other with the 2010 DEM~~s~~. These were compared with a dynamical simulation in which the glacier geometry was adjusted with the multitemporal DEMs, to consider the impact of glacier recession on mass balance. The TM2013 glacier boundaries were used but two ice masses, disconnected from Saskatchewan Glacier since 1979, were excluded from the original TM2013 outlines (see Figure 1c). The lateral, debris-covered moraines were also excluded from the glacier outlines (see Figure 1c). The term ‘reference mass balance’ (B_{a_r})~~A more recent, 2-m resolution DEM was built from a stereo pair of Pleiades Satellite panchromatic images acquired in September 2016 and using the NASA Ames Stereo Pipeline (ASP) (Shean et al., 2016). This DEM was used to update the geodetic mass balance from TM2013 (Supplementary Material). Since the 2010 WV2 DEM has the highest resolution and few gaps, it was considered the most reliable and used for model calibration and climate sensitivity experiments.~~ is used hereafter to refer to glacier-wide mass balance simulated with a fixed reference geometry while the term ‘conventional mass balance’ (B_{a_c}) is used for the simulation with adjusted glacier geometries (Huss et al., 2012).

3.2 Meteorological data~~a~~

3.2.1 On-glacier automatic weather station

An automatic weather station (AWS) was deployed in August 2014 on the medial moraine of Saskatchewan Glacier at an ~~altitude~~ elevation of 2193 m a.s.l., collecting near-continuous hourly data for a two-year period, until June 2016 (Figure 1c). Recorded variables include air temperature (T_a), relative humidity (RH), incoming global (G) and reflected ($SW\uparrow$~~out~~) solar radiation, and wind speed (WS) and direction (WD). *HOBO*™ air temperature sensors were installed by the ~~GSC~~ Geological Survey of Canada (GSC) on five ablation stakes (Figure 1c) and operated between May to August 2015. The *HOBO* sensors were~~,~~ shielded from solar radiation using naturally ventilated gill shields.

~~The data were used to calculate a mean diurnal cycle for the air temperature lapse rate on the glacier, diurnal lapse rate variations having been shown to affect glacier melt simulations (Petersen and Pellicciotti, 2011). The mean diurnal glacier~~

~~lapse rate cycle was combined with a mean monthly lapse rate estimated from the permanent weather station network (c.f. Sect. 3.2.2).~~

3.2.2 Meteorological data from permanent weather monitoring network

Seven ~~Mean monthly air temperature lapse rates and a constant precipitation lapse rate were calculated from the permanent weather monitoring network maintained by Environment and Climate Change Canada. Seven~~ weather stations were chosen from the permanent weather monitoring network maintained by Environment and Climate Change Canada~~with available air temperature data during the study period were chosen~~, in order to calculate temperature and precipitation lapse rates. The stations~~,~~ ~~ranging~~ ranged in elevation from 1050 to 2025 m a.s.l. (Figure 1b). As precipitation was not measured at the AWS site, a historical precipitation record was produced using data from the two weather stations closest to Saskatchewan Glacier (Parker Ridge, 2023 m a.s.l. and Columbia Icefield, 1981 m a.s.l., see Figure 1b). The Columbia Icefield station was only operated between May and November while Parker Ridge was operated mostly in winter and sometimes all year-round depending on road accessibility. Both discontinuous records were merged by averaging them. ~~A mean monthly lapse rate was calculated by linear regression of mean temperature against elevation, using a minimum of 5 stations for each month depending on available data. Mean diurnal anomalies in the glacier lapse rate, described in the previous section, were added to the monthly lapse rates.~~ ~~As precipitation was not measured at the AWS site, a homogenized historical precipitation record was produced using data from the two weather stations closest to Saskatchewan Glacier (Parker Ridge, 2023 m a.s.l. and Columbia Icefield, 1981 m a.s.l., see Figure 1b). The Columbia Icefield station was only operated between May and November while Parker Ridge was operated mostly in winter and sometimes all year-round depending on road accessibility. Both discontinuous records were combined into a single homogenised record. Because data gaps remained, reanalysis data corrected with the homogenised precipitation record was used instead to force the mass balance model (c.f. Sect. 3.2.3).~~ ~~As the glacier mass balance model only considers a constant precipitation lapse rate, a mean lapse rate of 15.6% 100 m^{-1} was calculated from the weather station network for the months of November to March, when snow precipitation is most abundant on the glacier and the relation between precipitation and elevation is strongest (Supplementary Material). The standard deviation (±4% 100 m^{-1}) was used to examine the sensitivity of modelled mass balance to the precipitation lapse rate.~~

3.2.3 Reanalysis data

While the precision of the on-glacier AWS data is useful to characterize the glacier microclimate, ~~its~~ the short and discontinuous record is not adequate to drive a physically-based, distributed glacier mass balance model for periods of a decade or more. Meteorological reanalysis data were thus used to force the mass balance model over the period 1979-2016, and the AWS data was used to apply a first-order bias correction to the reanalysis data. Data from the North American Regional

Reanalysis (NARR) (Mesinger et al., 2006) were chosen for this study because of its higher temporal (3 h) and spatial (32 km) resolution compared to other commonly used products, such as ERA interim and NCEP reanalyses. ~~The newer and higher resolution ERA5 reanalyses were not available at the time of analysis; moreover ERA5 reanalyses may also overpredict snowfall (Orsolini et al., 2019).~~ NARR precipitation have been found to be superior to other global reanalysis products in the US (Bukovsky and Karoly, 2007) and to represent well air temperature and humidity at high ~~altitude~~ elevation sites in southern BC, Canada (Trubilowicz et al., 2016). Chen et al. (2017)~~—~~ also showed that NARR reproduced well the seasonality of precipitation and temperature for 12 catchments across US and Canada. ~~ERA5 reanalyses were not available at the time of analysis; moreover ERA5 reanalyses may also overpredict snowfall (Orsolini et al., 2019).~~

NARR data ~~for the nine gridcells closest to the on-glacier AWS~~ ~~data for the gridpoint closest to Saskatchewan Glacier (see Figure 1)~~ were acquired from the National Center for Environmental Prediction (NCEP) at the National Centers for Atmospheric Research (NCAR) for the nine gridcells closest to the on-glacier AWS (see Figure 1b).~~.~~ The ~~The~~ NARR gridpoint whose center point is closest to the on-glacier AWS has an elevation of ~~elevation is~~ 2430 m a.s.l., i.e. 237 m higher than ~~the elevation of~~ the ~~glacier~~ AWS.~~-~~ ~~(see)used to downscale the data.~~ The following NARR variables were used: (i) instantaneous values of air temperature and relative humidity at 2 m above the surface (TMP2m-ANL, RH2m-ANL), (ii) wind speed vectors at 10 m above the model surface (U and V wind components: UGRD10m-ANL, VGRD10m-ANL), (iii) surface 3-hourly accumulated precipitation (APCPsfc-ACC), and (iv) 3~~3~~-hourly averaged surface downward shortwave radiation fluxes (DSWRFsfc-AVE). ~~and (v) instantaneous values of total cloud cover (CC: TCDCclm-3hr).~~

~~The 33-hourly data were interpolated to an hourly interval using linear interpolation and compared with the glacier AWS observations from 2014-2016.~~ Three~~3~~-hourly NARR variables were interpolated to the center of the hourly averaging interval used by the AWS datalogger. For instantaneous variables (ANL) the concurrent time tag was used for the interpolation while for averages (AVE) the time at the center of the averaging interval was used. Linear interpolation was used for relative humidity and wind speed. However, ~~The 3-hourly accumulated (ACC) precipitation totals were disaggregated to hourly values by dividing the 3-hour totals into three exact quantities.~~ b~~B~~oth incoming solar radiation and air temperature have strong diurnal cycles at the AWS site. Over the year, solar noon varies between 12 h 41 to 12 h 56~~-~~ and sunshine duration varies between 7.75 to 16.75 hours. The 3-hourly NARR data could thus underestimate the daily peaks in solar radiation and air temperature, especially since the midday NARR 3~~-~~-hourly average value spreads between 11 h 00 and 14 h 00. However, g~~G~~iven that solar noon occurs near the middle of this interval, ~~however,~~ the NARR midday solar radiation average may in fact well approximate the peak mid-day value, while the 14 h 00 instantaneous temperature value is close to the time of maximum daily temperature. Nevertheless, to reduce the probability of the diurnal cycle being attenuated in the interpolated NARR data, a shape-preserving piecewise cubic interpolation was used to interpolate ~~these variables~~air temperature and solar radiation to an hourly interval.

The 3-hourly accumulated (ACC) precipitation totals were disaggregated to hourly values by dividing the 3-hour totals into three exact quantities.

3.2.4 Downscaling NARR to weather stations

Downscaling the NARR variables to the glacier model grid involved two steps: (1) interpolation of the NARR gridded data to the reference weather stations; (2) bias correction of the interpolated NARR data.~~;~~ Two interpolation methods were used and compared to extract NARR time-series. The first one is a simple nearest neighbour interpolation, i.e., the NARR grid point whose center point is closest to the reference stations (the on-glacier AWS and the merged Parker Ridge/Columbia precipitation station: see Figure 1 for locations) was used. The second method used bilinear interpolation from the nine NARR grid points closest to the weather stations.

~~The NARR meteorological variables (Ta, RH, WS, G) were downscaled to the AWS site using~~ A~~a~~ simple bias correction procedure (Teutschbein and Seibert, 2012) was used to correct NARR biases. ~~using the MeteoLab (ML) Matlab® Toolbox (Cofiño et al., 2004).~~ Air temperature, relative humidity, wind speed and solar radiation from the interpolated NARR time series were corrected relative to the on-glacier AWS. ~~Because~~ Since precipitation was not measured at the glacier AWS, the NARR precipitation were corrected with the merged historical precipitation record from the Parker Ridge/Columbia stations~~homogenized historical precipitation record~~. Several data gaps remained in the merged record, and no observations were available after 2008. Hence only days with observations were used for bias correction over the period when NARR overlapped the merged precipitation record (1980-2008). ~~was used to downscale the NARR precipitation data.~~ Two simple bias correction methods were tested and compared, namely ~~: i)~~ scaling and ~~ii)~~ empirical quantile mapping (EQM) (e.g. Teutschbein and Seibert, 2012; Wetterhall et al., 2012).~~,~~ ~~were applied and compared.~~ The scaling method is the simplest, in which the NARR outputs are scaled with the difference (additive correction) or quotient (multiplicative correction) between the mean NARR and mean of observations. An additive correction ~~is~~ was used for unbounded variables ($T_{a,NARR}$~~Ta~~) and a multiplicative correction for strictly positive variables (RH_{NARR}~~G~~, WS_{NARR}, G_{NARR} and P_{NARR}) as it also preserves the frequency. Because errors in incoming solar radiation can originate from improper representation of the atmospheric transmissivity and cloud cover in NARR and/or shading differences between the NARR smoothed topography and the real topography surrounding the AWS, a time-varying scaling method was used to correct the NARR global shortwave radiation data (G_{NARR}). A mean diurnal multiplicative correction factor was calculated by scaling the mean observed diurnal G cycle with that of the hourly-interpolated NARR. A separate diurnal correction factor was calculated for each month of the year, to account for the seasonality in sun angle and related errors between NARR and observations.

The bias correction methods were evaluated against the glacier AWS data using split sample cross-validation, and compared with the baseline performance, i.e., without corrections to the NARR variables. The AWS data was split into two one-year sub-periods on which downscaling methods were respectively calibrated and validated; then both sub-periods were inverted, and the mean validation statistics calculated. For precipitation the entire historical record was used, so validation sub-periods are longer than for other variables. The cross-validated Pearson correlation coefficient (*r*~~R~~), mean error (bias) and~~,~~ root mean square error (RMSE) ~~and mean absolute error (MAE)~~ were used for performance assessment. The performance of ~~downscale~~ bias-correction ~~performance~~ was evaluated at both hourly and daily time intervals.

3.2.5 Extrapolation of NARR data to the glacier DEM

The downscaled NARR data was extrapolated from the reference stations to the glacier DEM. Because data gaps remained in the merged Parker Ridge/Columbia precipitation record, the downscaled NARR precipitation record was used to force the mass-balance model. As the glacier mass balance model only considers a constant precipitation lapse rate, a mean lapse rate of 15.6% 100 m^{-1} was calculated from the weather station network for the months of November to March, when snow precipitation is most abundant on the glacier and the relation between precipitation and elevation is strongest (Supplementary Material). The extrapolated total precipitation was split between rain and snowfall according to a threshold temperature ($T0$) of 1.5 °C, at which 50% of the precipitation falls as snow and 50% as rain. This value corresponds to a typical rain-snow temperature threshold for continental mountain ranges and was inferred from the relative humidity at the AWS site (83%) following Jennings et al. (2018). A linear interpolation of the rain/snow fraction is performed between $T0$-1 °C (100% snow) and $T0$+1 °C (100% rain).

A mean monthly air temperature lapse rate was calculated from the permanent weather station network. ~~(cf. section 3.2.2).~~ Lapse rates were calculated by linear regression of mean temperature against elevation, using a minimum of five stations for each month, depending on available data. Since diurnal lapse rate variations can affect glacier melt simulations (Petersen and Pellicciotti, 2011), the on-glacier *HOBO* sensors were used to calculate a mean diurnal air temperature lapse rate cycle on the glacier. Diurnal anomalies were produced by subtracting the mean on-glacier lapse rates from this diurnal cycle, and were then added to the mean monthly lapse rates estimated from the permanent weather station network. Hence, the lapse prescribed to the model varied on a diurnal as well as on a seasonal (monthly) scale, and was used to extrapolate air temperature to the glacier DEM.

In the absence of constraining data, wind speed and relative humidity were assumed spatially invariant, as ~~done~~done in earlier modelling studies off mountain glaciers (e.g. Anderson et al., 2010; Anslow et al., 2008; Arnold et al., 1996; Arnold et al., 2006; Hock and Holmgren, 2005; Mölg et al., 2008). Wind speed can be expected to be relatively constant down-glacier due to the presence of a katabatic wind or an ‘ice field breeze’ wind, as found on the neighboring Athabasca outlet glacier (Conway et al., 2021); however, it is possible that the more open accumulation zone of Saskatchewan Glacier could have~~s~~ higher winds than measured at the mid-glacier AWS ~~mid-glacier~~ (Figure 1). Global solar radiation ~~(G)~~ from the downscaled NARR (G_{NARR}) was separated into direct (I) and diffuse (D) components, which were then extrapolated individually to each gridcell considering terrain effects of the multitemporal DEMs. Further details are given in the model description in section 3.3. ~~Total precipitation is extrapolated to the model grid from the altitude of the homogenized reference station (2000 m a.s.l.) using the constant gradient calibrated from weather stations (c.f. Sect. 3.2.2). Total precipitation is split between rain and snowfall according to a threshold temperature ($T0$) of 1.5 °C, at which 50% of the precipitation falls as snow and 50% as rain. This value corresponds to a typical rain-snow temperature threshold for continental mountain ranges and was inferred from the relative humidity at the AWS site (83%) following Jennings et al. (2018). A linear interpolation of the rain/snow fraction is performed between $T0$-1 °C (100% snow) and $T0$+1 °C (100% rain).(Conway et al., 2021)(Anderson et al., 2010; Anslow et al., 2008; Arnold et al., 1996; Arnold et al., 2006; Hock and Holmgren, 2005; Mölg et al., 2008)~~

3.3 Mass balance model

The physically-based, distributed glacier mass balance model DEBAM (Hock and Holmgren, 2005) was used to simulate the mass balance of Saskatchewan Glacier over the period 1979-2016. The surface mass balance is expressed as:

$$b(t) = P_s \cancel{Ps}(t) - M(t) - S(t) \quad (1)$$

Where $b(t)$ is the point surface mass balance at time t, P_s ~~Ps~~ is snow precipitation, M is melt and S is sublimation. ~~Total precipitation is extrapolated to the model grid from the altitude of the homogenized reference station (2000 m a.s.l.) using the constant gradient calibrated from weather stations (c.f. Sect. 3.2.2). Total precipitation is split between rain and snowfall according to a threshold temperature ($T0$) of 1.5 °C, at which 50% of the precipitation falls as snow and 50% as rain. This value corresponds to a typical rain-snow temperature threshold for continental mountain ranges and was inferred from the relative humidity at the AWS site (83%) following Jennings et al. (2018). A linear interpolation of the rain/snow fraction is performed between $T0$-1 °C (100% snow) and $T0$+1 °C (100% rain).~~

The model calculates the distributed mass and energy balance on each 100 x 100 m grid cell from the hourly downscaled NARR meteorological forcing data including air temperature, relative humidity, precipitation, wind speed and incoming shortwave global radiation ~~(SWin~~~~G)~~. The energy at the surface available for melt on the glacier, Q_M (W m^{-2}), was calculated according to Eq. (2) and converted into meltwater equivalent M (m w.e.~~m~~ h^{-1}) using the latent heat of fusion:

$$Q_M + Q_G + Q_R + Q_L + Q_S \cancel{Q_H} \cancel{+ L\uparrow} + LW_S \downarrow + LW_T \downarrow + LW \uparrow + (1-\alpha)(I + D_S + D_T) = 0 \quad (2)$$

where I is the direct (beam) incoming shortwave solar radiation, D_S and D_T are the diffuse sky and terrain shortwave radiation, respectively, α is the albedo, $LW_S \downarrow$ and $LW_T \downarrow$ are the longwave sky and terrain irradiance, respectively, $LW \uparrow$ is longwave outgoing radiation, Q_S ~~Q_H~~ is the sensible-heat flux, $Q_{\cancel{E}L}$ is the latent-heat flux and Q_R is the energy supplied by rain (Hock and Holmgren, 2005). The ground heat flux in the ice or snow, Q_G~~,~~, is often small for temperate glaciers and was neglected (e.g., Hock, 2005; Yang et al., 2021). ~~{{Hock, 2005 #102}Yang, 2021 #156}.~~ Fluxes are positive towards the glacier surface and measured or calculated in W m^{-2}. The model allows for different parameterizations for calculating energy balance components, depending on the availability of forcing data ~~and calculation speed~~. The parameterizations used in this work are ~~detailed~~detailed ~~in the next subsections.~~in the next sections.

3.3.1 Shortwave incoming radiation

~~The global solar radiation (G) from NARR downscaled at the AWS location is separated into the direct (I) and diffuse (D) components, which are then extrapolated individually to each gridcell considering terrain effects of the multitemporal DEMs.~~ Following Hock and Holmgren (2005), the separation of the downscale NARR global radiation (G_{NARR}~~G~~) into direct (I) and diffuse (D) radiation is based on an empirical relationship between the ratio of measured global radiation to top-of-atmosphere radiation, G_{NARR}~~G~~$/I_{TOA}$, and the ratio of diffuse to global radiation, D/G_{NARR}~~G~~. Total diffuse radiation D calculated at the AWS is then subtracted from the global radiation to yield the direct solar radiation at the AWS site, I_S. Topographic shading is calculated at each hour and for each gridcell from the path of the sun and the effective horizon. If the AWS is shaded by surrounding topography, any measured global radiation is assumed diffuse. Direct radiation I is obtained at each gridcell following Hock and Holmgren (2005) as:

$$I = \frac{I_S}{I_{SC}} I_C \qquad (3)$$

where the subscript s refers to the location of the climate station and c denotes clear-sky conditions. I_C is the potential clear-sky direct solar radiation which accounts for the effects of slope and aspect of each grid cell, as well as shading from surrounding topography. The ratio I_S/I_{SC} measured at the AWS accounts for deviations from clear-sky conditions, expressing the reduction of potential clear-sky direct solar radiation mainly due to clouds. The ratio~~,~~ ~~and~~ is assumed to be spatially constant, which is reasonable given the large (~400 km) correlation length scale of cloud cover (Jones, 1992). Eq. (3) can not be applied when the AWS is shaded, since I_C = 0. In this case and for glacier grid cells that remain illuminated, the last ratio that could be obtained before the AWS grid cell become shaded is applied, which assumes that cloud conditions remain constant until the climate station is illuminated again (usually the next morning). The constant ratio was applied to 57% of the glacier surface which was sunlit while the AWS was shaded, for a mean and maximum duration of 0.73 and 2.16 hours, respectively. The impact on the radiative balance is thus considered to be small because this situation occurs in the mornings and end of days at low sun illumination angles, and also because the temporal correlation length scale of cloud cover is a few hours ~~The impact of this assumption on the radiative balance is considered to be small because this situation occurs at low sun illumination angles, and also because the temporal correlation length scale of cloud cover is a few hours~~ (Jones, 1992). ~~.~~The total diffuse radiation (D) is calculated as:

$$D = D_0 F + \alpha_m G_{NARR} \cancel{G} (1 - F) \tag{4}$$

where the first righthand term represents sky radiation (D_S) and the second term terrain radiation (D_T). D_0 is diffuse radiation from an unobstructed sky calculated at the AWS and is considered spatially constant. F is the grid cell sky-view factor defined by Oke (1987) and G_{NARR} is the downscaled NAAR global radiation at the AWS. The mean albedo (α_m) of the surrounding terrain obtained for every hour is the arithmetic mean of the modelled albedo of all grid cells for the entire glacier (Hock and Holmgren, 2005).

3.3.2 Albedo

The albedo parameterisation of Oerlemans and Knap (1998) was used to simulate the albedo (α):

$$\alpha_{snow}(t) = \alpha_{firn} + (\alpha_{frsnow} - \alpha_{firn}) exp\left(\frac{s-t}{t^*}\right) \tag{5}$$

$$\alpha(t) = \alpha_{snow}(t) + \alpha_{ice} - \alpha_{snow}(t)\ exp\left(\frac{d}{d^*}\right) \tag{6}$$

where $\alpha_{snow}(t)$ is snow albedo, $\alpha(t)$ the final glacier albedo at time t, α_{firn} is the characteristic albedo of firn, α_{frsnow} is the characteristic albedo of fresh snow and α_{ice} is the characteristic albedo of ice. The time scale (t^*) determines how fast the snow albedo decays over time (days) and approaches the firn albedo after a fresh snowfall, d^* is a characteristic snow depth scale (cm) controlling the transition from snow albedo to ice albedo, s is the day of the last snowfall and d is snow depth (cm). The constant, characteristic albedo values were set to α_{frsnow} = 0.9 for fresh snow based on observations at the AWS. Ice albedo was mapped using 17 of the 18 cloud-free, end-of-summer Landsat images used to delineate the mean snowline position. Atmospherically corrected surface reflectance from the Landsat 5 ETM and Landsat 7 ETM+ sensors were converted to broadband albedo following Knap et al. (1999)~~-~~. A median albedo map was produced, from which the distribution of ice albedo values was extracted in a region of interest extending below the mean snowline and excluding the glacier margins where shade effects were noticed (Supplementary Material). The median of the distribution (0.24) was used as the representative ice albedo (α_{ice}). ~~and the standard deviation (0.03) used as uncertainty range for sensitivity analysis.~~ The characteristic time (t^*) and depth (d^*) scales were calibrated using snow depth and albedo measurements at the AWS. Since the AWS was on a moraine the value for α_{ice} was set instead to the measured soil albedo for calibration purposes. The optimum values used in the model, found by minimizing the RMSE of the simulated albedo, were ~~of~~ t^* = 14 day and d^* = 3 cm. ~~were used in the model.~~

3.3.3 ~~Atmospheric incoming~~ L~~l~~ongwave calculation

~~As~~Since no observations of incoming longwave radiation were available at the AWS for bias-correction, NARR longwave radiation was not used for model forcing because it would carry an elevation bias and would not account for terrain effects. Instead, t~~T~~he ~~atmospheric~~ incoming sky longwave radiation ($LW_S\downarrow$~~in~~) was~~is~~ calculated based on~~–~~ the Stefan-Boltzmann equation~~the parameterisation of Konzelmann et al. (1994)~~, which relies on independent variables of air temperature and atmospheric emissivity ~~, vapour pressure and cloud cover~~ according to Eq. (7):

$$LW_S \downarrow \cancel{LWin} = F\varepsilon_{NARR}\cancel{[\varepsilon_{cs}(1-n_{NARR}n^{p})+\varepsilon_{oc}n_{NARR}n^{p}]}\sigma T_{a,NARR}\cancel{Ta}^{4} \qquad (7\cancel{a})$$

$$\cancel{\varepsilon_{cs} = 0.23 + 0.443\left(\frac{e}{Ta}\right)^{1/8}} \qquad \cancel{(7b)}$$

Where F is the skyview factor, ε_{NARR}~~ε_{cs} is the clear-sky emissivity, n_{NARR} n is the fractional cloud cover fraction (0-1) derived from NARR cloud cover,~~ is the atmospheric emissivity from NARR, σ is the Stefan-Boltzmann constant (5.67×10^{8} m^{-2} K^{-4}) and~~,~~ $T_{a,NARR}$ is the downscaled NARR air temperature in Kelvin. ~~and $T_{a,NARR}$ Ta is the downscaled NARR air temperature in Kelvin. The overcast sky emissivity (ε_{oc} = 0.968) and exponent p = 2, were left to default values in DEBAM.~~ We adjusted the ~~emissivity~~ $LW_S\downarrow$ calculation in DEBAM to include the spatial variability in air temperature, i.e., by using $T_{a,NARR}$ ~~T_a~~ extrapolated to the glacier DEM, since the default parameterisation only used air temperature ~~T_a~~ ~~Ta~~ measured at the AWS location for the entire glacier area. This led to an overestimation of melt in the accumulation zone and an underestimation in the ablation zone – both corrected when including the distributed $T_{a,NARR}$ ~~T_a~~ ~~Ta~~ in Eq. 7~~a~~. Terrain longwave irradiance, $LW_T\downarrow$, was calculated using the parameterization by Plüss and Ohmura (1997) for snow covered alpine terrains ~~(Plüss and Ohmura, 1997)~~:

$$LW_T \downarrow = (1-F)\pi(L_b + aT_{a,NARR}\cancel{Ta} + bT_s) \qquad (8)$$

where F is the sky view factor, L_b= 100.2 Wm^{-2} sr^{-1} is the emitted radiance of a 0° black body, T_s is the temperature of the emitting surface and a = 0.77 Wm^{-2} sr^{-1} and b = 0.54 Wm^{-2} sr^{-1} are coefficients calibrated for snow-covered alpine environments (Plüss and Ohmura, 1997).

Outgoing longwave radiation ($LW\uparrow$) is calculated from the Stefan ~~Boltzman~~Boltzmann equation and the simulated surface temperature (T_s). T_s is obtained in an iterative process by lowering surface temperatures in case of negative energy balances until the energy balance equals zero (Hock and Holmgren, 2005).

3.3.4 Turbulent heat fluxes

The turbulent sensible (Q_S) ~~Q_H~~ ~~a~~and latent ($Q_{\cancel{E}L}$) heat fluxes were calculated from the bulk aerodynamic method (Hock and Holmgren, 2005) based on air temperature ($T_{a,NARR}$ ~~T_a~~ ~~Ta~~), wind speed (WS_{NARR} ~~WS~~) and vapour pressure (e ~~e_z~~) at height z = 2 m ~~(z)~~ above the surface:

$$Q_S \cancel{Q_H} = \rho C_p \frac{k^2}{\left[In\left(\frac{z}{z_{0W}}\right)-\psi_M\left(\frac{z}{L}\right)\right]\left[In\left(\frac{z}{z_{0T}}\right)-\psi_M\left(\frac{z}{L}\right)\right]} WS_{NARR} \cancel{WS} \cancel{WS_z} (T_{a,NARR} - T_s \cancel{T_a} \cancel{Ta_z} \cancel{- T_{s0}}) \quad (8)$$

$$Q_{\cancel{E}L} = L_v \frac{0.623\rho_0}{P_0} \frac{k^2}{\left[In\left(\frac{z}{z_{0W}}\right)-\psi_M\left(\frac{z}{L}\right)\right]\left[In\left(\frac{z}{z_{0e}}\right)-\psi_M\left(\frac{z}{L}\right)\right]} WS_{NARR} \cancel{WS} \cancel{WS_z} (e \cancel{e} \cancel{e_z} - e_{s\cancel{0}}) \quad (9)$$

where ρ is air density at sea level (1.29 kg m^{-3}), P_0 is the mean atmospheric pressure at sea level (101 325 Pa), C_p is the specific heat capacity of air (1005 J kg^{-1} K^{-1}), k is the von Kármán's constant (0.4), $T_{s\cancel{0}}$ is the surface temperature in Kelvin, e is the air vapour pressure as defined before~~derived from downscaled NARR relative humidity and air temperature~~ , $e_{s\cancel{0}}$ is the surface vapour pressure in Pa and~~,~~ z_{0W}, z_{0T} and z_{0e} are the roughness lengths for the logarithmic profiles of wind speed, temperature and water vapour, respectively, ψ_M, ψ_H and ψ_E are the stability functions, L is the Monin–Obukhov length, and L_v is the latent heat of evaporation (2.514 × 10^6 J kg^{-1}) or sublimation (2.849 × 10^6 J kg^{-1}), depending on surface temperature and the direction of the latent heat flux. If $Q_{\cancel{E}L}$ is positive, condensation occurs if the surface is melting, or deposition if the surface is frozen. Sublimation occurs when $Q_{\cancel{E}L}$ is negative. The aerodynamic roughness length (z_0) for snow and ice influences the intensity of turbulent fluxes at the glacier surface. Typical z_0 values for glacier snow (z_{0_snow}) range between 0.5 and 6 mm (Brock et al., 2006; Fitzpatrick et al., 2019; Munro, 1989), while z_0 for smooth glacier ice surfaces (z_{0_ice}) typically range between 0.1 and 6 mm (Brock et al., 2006). Munro (1989) measured z_0 values between 0.67 and 2.48 mm along and across the grain of the ice, respectively, and 5-6 mm for snow on nearby Peyto Glacier, which has a similar ice facies morphology as the Saskatchewan Glacier, based on our field observations. A mean z_{0_ice} of 1.58 mm and z_{0_snow} of 5.5 mm ~~were~~ was thus used in the model. ~~, with an uncertainty range of ±1 mm used for sensitivity analysis.~~ The roughness length for temperature and water vapour were both considered to be two orders of magnitude less than roughness lengths for wind (Hock and Holmgren, 2005).

3.4 Model validation and ~~parameter~~ uncertainty analyses

The simulated mass balance was validated at the point-scale against available seasonal and annual glaciological mass balance observations since 2012, and at the glacier scale using the reconstructed geodetic mass balance from 1979 to 2016. These data are described in detail in the Supplementary Material. The sensitivity of the reconstructed mass balance was tested with respect to (i) the NARR interpolation method; (ii) the NARR bias-correction method; (iii) ~~the type of~~replacing NARR ~~variable~~forcings by their AWS counterpart; ~~used for forcing;~~ (iv) uncertain model parameters. For (i), the model was run with NARR forcings respectively interpolated with the nearest neighbour and bilinear methods. For (ii), the model ~~run~~forced with the bias-corrected

NARR forcings was compared with a model ~~run~~forced with raw ~~in which only the interpolated~~ NARR, but correcting for the elevation difference between NARR and the reference stations ~~air temperature and precipitation were lapsed to the elevation of the weather stations,~~ using ~~the~~the mean measured temperature and precipitation lapse rates ~~raw NARR inputs after adjusting the air temperature and precipitation for the elevation difference between the NARR gridpoint and the reference weather stations, using the mean calculated temperature and precipitation lapse rates~~ (e.g. Fiddes and Gruber, 2014). For (iii), the NARR forcings ($G_{NARR}, T_{a,NARR},$ ~~$(T_a, RH, G,$~~ WS_{NARR}, RH_{NARR} ~~WS~~) were replaced one-at-a-time by the AWS observations and the simulated point mass balances compared with stakes observation for 2015, the only year with continuous AWS data and concurrent glaciological observations. For (iv), w~~W~~hile the physical nature of the model did not require formal calibration, four uncertain model parameters were subjected to a sensitivity analysis to characterize their impact ~~of their uncertainty~~ on the modelled mass balance. The precipitation lapse rate was varied within ± 4% 100 m^{-1}, which corresponds to the standard deviation of the precipitation lapse rate calculated from the permanent weather network (~~see section~~see Sect. 3.2.5 and Supplementary Material). The ~~(c.f. section 3.2.2),~~ ice albedo (α_{ice}) was varied within ± 0.03, which corresponds to the spatial standard deviation of ice albedo observed from satellite images (~~c.f. see section~~see Sect. 3.3.2). The ~~, and the~~ aerodynamic roughness lengths for ice (z_{0_ice}) and snow (z_{0_snow}) were varied within ± 1 mm, which covers the range of values by Munro (1989) on nearby Peyto glacier (~~c.f. see section~~see Sect. 3.3.4). The sensitivity to roughness lengths was also extended to ± one order of magnitude, as an extreme case. ~~The sensitivity of simulated mass balance to NARR downscaling was also examined by forcing the model with the raw NARR inputs after adjusting the air temperature and precipitation for the elevation difference between the NARR gridpoint and the reference weather stations, using the mean calculated temperature and precipitation lapse rates (e.g. Fiddes and Gruber, 2014).~~

3.5 Climate sensitivity

The validated DEBAM model was used to perform a ~~static (e.g. with fixed 2010 glacier geometry)~~ climate sensitivity analysis of the reference mass balance (with respect to the 2010 glacier hypsometry: ~~,~~ $B_{r,\ 2010}$) ~~(Oerlemans, 2001)~~ to potential changes in air temperature (ΔT_a ~~Ta~~) ranging between 0 to 8 °C (1 °C interval) and precipitation (ΔP) ranging between -20 to +20% (5% interval). These warming and precipitation changes scenarios encompass~~e~~ mean annual changes projected by ensemble GCM simulations for the mid (2041-2070) and late (2071-2100) 21st century relative to the most recent 30-year climatological period (1981-2010) and under different Representative Concentration Pathway (RCP) scenarios (IPCC, 2013)~~(Stocker, 2014)greenhouse gases emission scenarios (IPCC, 2013)~~. The ensemble climate projections from the Coupled Model Intercomparison Project Phase 5 (CMIP5) were obtained from the KNMI Climate Change Atlas (Trouet and Van Oldenborgh, 2013) for ~~Representative Concentration Pathway (RCP) scenarios~~ RCP ~~+~~2.6 (n=32), ~~+~~4.5 (n=42), ~~+~~6.0 (n=25) and ~~+~~8.5 (n=39) for the gridpoint closest to the ELA of Saskatchewan Glacier (Figure 1). The number of simulations (n) depended on the availability of the CMIP5 models for each scenario (IPCC, 2013)~~(IPCC, 2013b)~~. The *IPCC AR5 Atlas* subset was used, which uses only a single realisation of each model and weights all models equally, where model realisations differing only in model parameter settings are treated as different models ~~-~~(IPCC, 2013)~~(IPCC, 2013b)~~. The DEBAM model was run 81 times for every combination of ΔT_a ~~Ta~~ and ΔP perturbation imposed on the $T_{a,NARR}$ ~~T_a~~ ~~Ta~~ and P_{NARR} records over the 30-year reference period 1981-2010. Changes in mass balance for each sensitivity run were plotted as response surfaces, which provide a simple way to assess climate sensitivity across a range of possible climate change scenarios (e.g. Aygün et al., 2020b; Prudhomme et al., 2010). Mean temperature and precipitation changes along with their 95% confidence intervals were overlained onto the response surfaces to show the most likely future climate trajectories given by the GCM projections.

4 Results

4.1 Meteorological observations

Daily and monthly averages of air temperature (T_a~~Ta~~), relative humidity (RH), incoming solar radiation (G) and wind speed (WS) measured at the glacier AWS show notable differences between the two years of observation (Figure 2). The winter of 2014-2015 was, overall, colder than 2015-2016, with frequent cold excursions below -15 °C and a winter absolute minimum of -27 °C vs. -17 °C in 2015-16, although conditions were warmer in December. Relative humidity ~~is~~ was generally high throughout the year (mean = 79%), illustrating the predominantly humid climate of the Columbia Icefield, but decreases noticeably in summer. The variability in daily RH is similar between the two years of measurements. The incoming solar radiation shows pronounced seasonality, varying between ~50 W m^{-2} in winter and ~300 W m^{-2} in summer, with daily variations between 50 W m^{-2} in winter and 150 W m^{-2} in summer caused by variable cloud cover. A gentle breeze blows on average on the glacier ~~The wind speed is generally high~~ (mean wind speed = ~~16~~ 4.46 m s^{-1}), but wind speed ~~and~~ shows significant day-to-day variations ~~,~~ as well as higher values in winter. A gradual increase in wind speed is notably observed from the lowest monthly mean value in May 2015 (1.76~~6~~ m s^{-1}) to a maximum in February (~~26~~ 7.13 m s^{-1}). The ~~homogenized~~ historical precipitation records from the Columbia Icefield and Parker Ridge stations contain~~s~~ several gaps but still ~~displays~~ portrays the seasonal and interannual variability in precipitation near the glacier (Figure 2e). The mean ~~monthly~~ annual accumulated precipitation throughout the historical period with complete data ~~is~~ was ~~73 mm month^{-1} (~~874 mm a^{-1} ~~)~~ but varied~~s~~ between ~~23 mm mo^{-1} (~~276 mm a^{-1}~~)~~ and ~~142 mm mo^{-1} (~~1704 mm a^{-1}~~)~~. ~~-~~ Precipitation are more abundant in winter, with 58% of precipitation falling between October to March, mostly as snow, and 42% falling during April-September, mostly as rain.

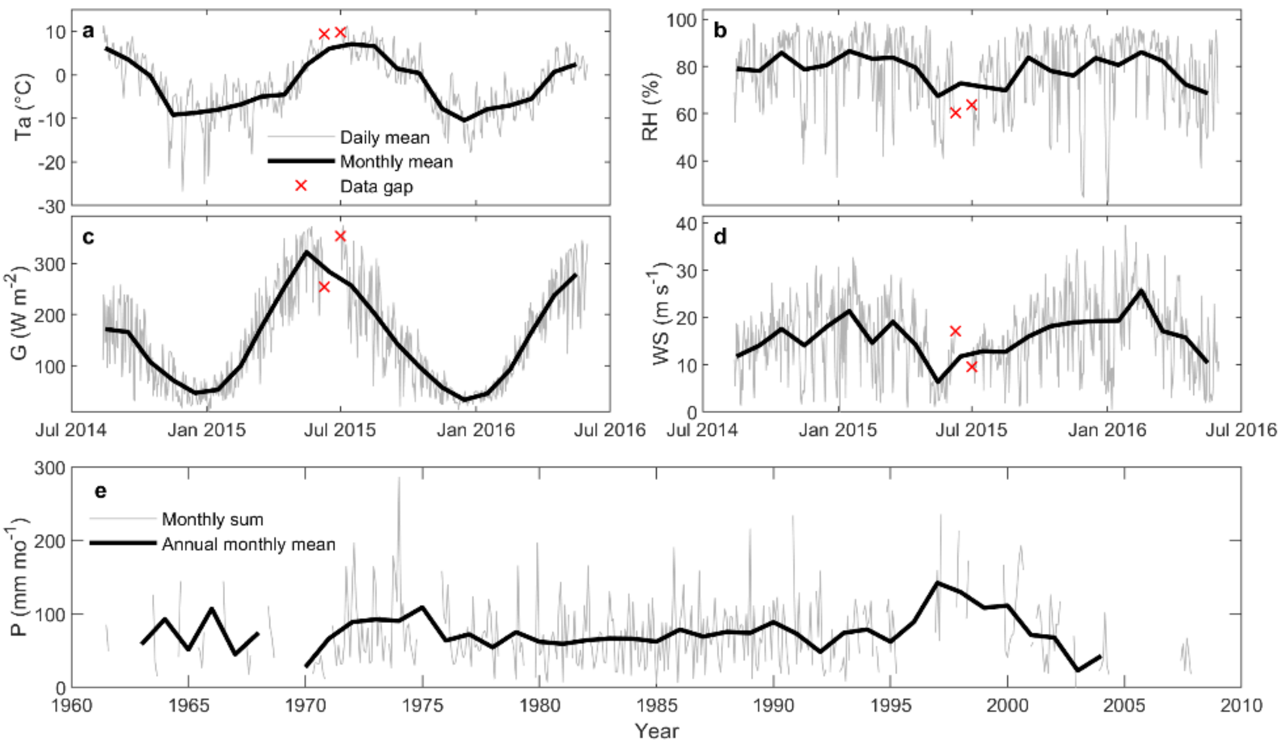

a
b
c
d
e
Ta (°C)
RH (%)
G (W m-2)
WS (m s-1)
P (mm mo-1)
Daily mean
Monthly mean
Data gap
Monthly sum
Annual monthly mean
Jul 2014
Jan 2015
Jul 2015
Jan 2016
Jul 2016
Year

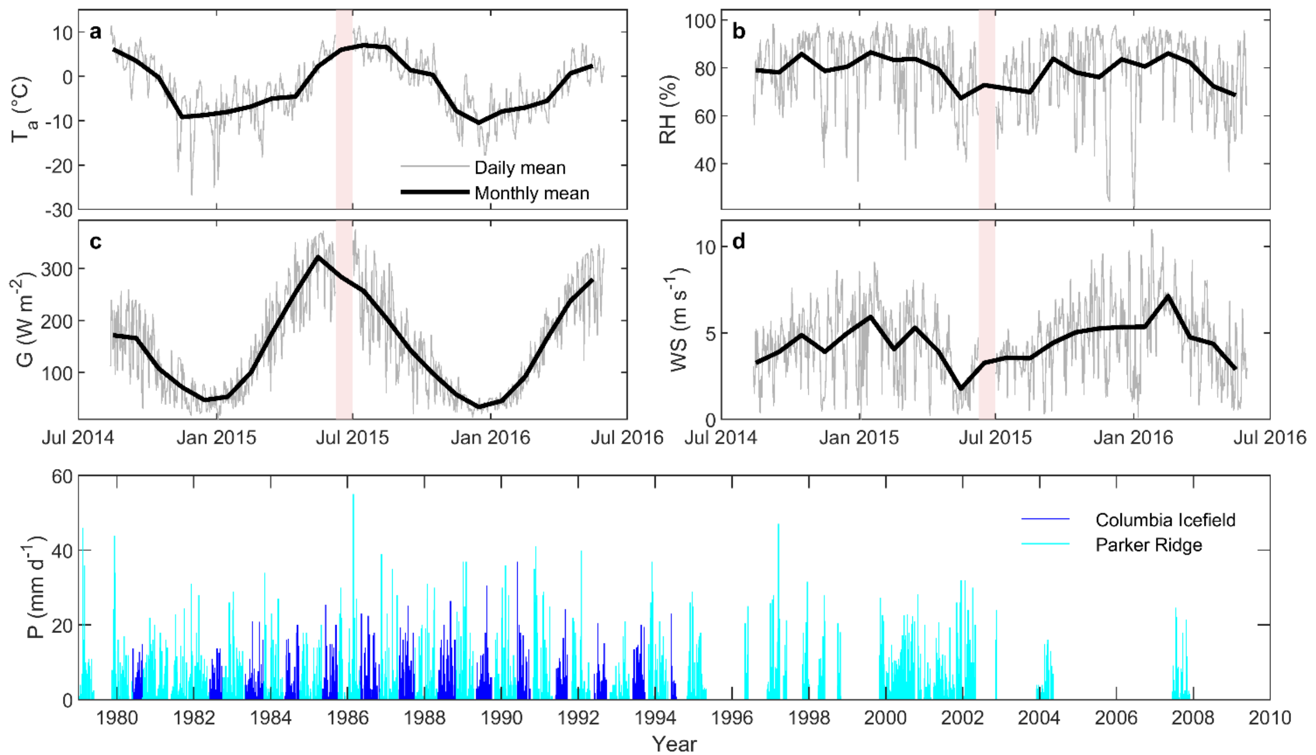
a
b
c
d
T$_a$ (°C)
RH (%)
G (W m^{-2})
WS (m s^{-1})
Daily mean
Monthly mean
Jul 2014
Jan 2015
Jul 2015
Jan 2016
Jul 2016
P (mm d^{-1})
Columbia Icefield
Parker Ridge
Year

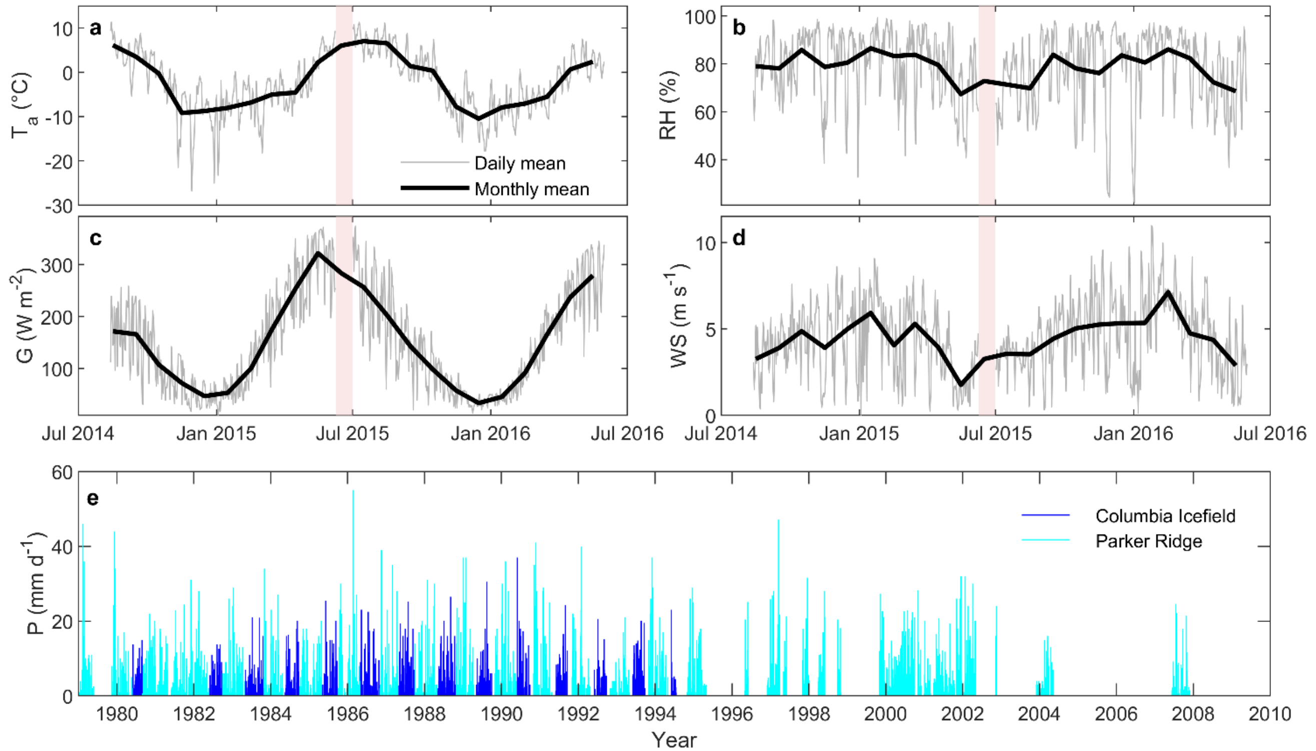

Figure 2. Two-year record from the Saskatchewan Glacier AWS (2014-2016). (a) Air temperature (T_a~~Ta~~); (b) relative humidity (*RH*); (c) incoming global solar radiation (*G*); (d) wind speed (*WS*). ~~The red crosses~~Pink shades delineate the data gap caused by the fall of the AWS (11 to 30 June 2015). (e) ~~Homogenized~~ Daily precipitation records from Parker Ridge and Columbia Icefield permanent stations. Note the several gaps after 1995 when the Columbia Icefield station was interrupted.

4.2 NARR downscaling~~bias correction~~

The NARR meteorological variables used to drive the glacier mass balance model were compared with data from the glacier AWS (2014-2016) and the 29-year long ~~nearby homogenized~~ merged daily precipitation record (Figure 3). ~~(Table 1). Results show that even~~Even ~~without~~ prior to applying bias correction, $T_{a,NARR}$, ~~T_a Ta~~ *RH*$_{NARR}$ and G_{NARR} show a good correlation with ~~the NARR~~ AWS ~~data~~ observations on a daily scale, for both NARR spatial interpolation methods. As expected, the correlation is poorer for WS_{NARR}, likely because the local glacier katabatic wind recorded by the AWS is not well represented in NARR due to its coarse grid resolution. The NARR precipitation is also rather poorly correlated with observations ($r = 0.30$). Biases in raw NARR variables are relatively small compared to the mean and range of values recorded (blue dots in Figure 3)~~(Figure 2)~~, except for G_{NARR} (30.4 W m^{-2}) and ~~*precipitation*~~ P_{NARR} (0.55 mm d^{-1}), which represent 15% and 25% of their mean measured values over their period of observation, respectively. The cold bias (-1.26 °C) observed for ~~NARR~~$T_{a,NARR}$ from the closest gridcell ~~T_a~~~~Ta~~ is consistent with the elevation difference between the AWS (2193 m) and the NARR ~~gridpoint~~ gridcell (2430 m) (ΔZ = 237 m), which results in an expected temperature difference of -1.19°C using the mean observed lapse rate of -0.5 °C 100 m^{-1} (~~c.f. see Sect~~see Sect.~~.~~ 4.3). Neither the scaling nor the EQM correction methods improved the Pearson correlation coefficient (r~~R~~) – primarily since it~~R~~ is a relative measure of the synchronicity between two-time series and is unaffected by the mean values. The EQM method was found to improve $T_{a,NARR}$ ~~T_a~~~~Ta~~ best, closely followed by the scaling method, while the scaling method was slightly superior for RH_{NARR}, WS_{NARR} and P_{NARR}~~.~~. However, scaling only slightly reduced the errors for WS_{NARR} and P_{NARR} and had no effect on RH_{NARR}, which had an initial low error. ~~. Validation statistics were significantly improved using the scaling technique for precipitation and WS, while~~ T~~t~~he diurnal scaling correction applied to G_{NARR} also reduced its errors. ~~Both methods did not improve the errors in relative humidity, which had an initial low error.~~ Overall, the scaling bias correction method was globally the more efficient approach across all variables and both NARR spatial interpolation methods, and ~~this method was thus~~was thus applied to all variables for consistency~~,~~ except for relative humidity, which ~~remained~~ was left uncorrected. Similar results, although with expectedly higher errors, were found for the interpolated NARR hourly data (Supplementary Table S3). The bilinear NARR interpolation method resulted in slightly lower RMSE and bias values for the raw variables, ~~i.e.~~i.e., before bias correction (blue bars and dots in Figure 3), except for the slightly higher bias for *RH*. However, after applying the station-based bias correction, the bias and RMSE values were very similar among the two methods. As such, the NARR forcings downscaled from the nearest NARR gridcell were used as primary model forcings for the mass balance reconstruction and climate sensitivity experiments, and the sensitivity of the reconstructed mass balance to NARR spatial interpolation method investigated in Section 4.6.

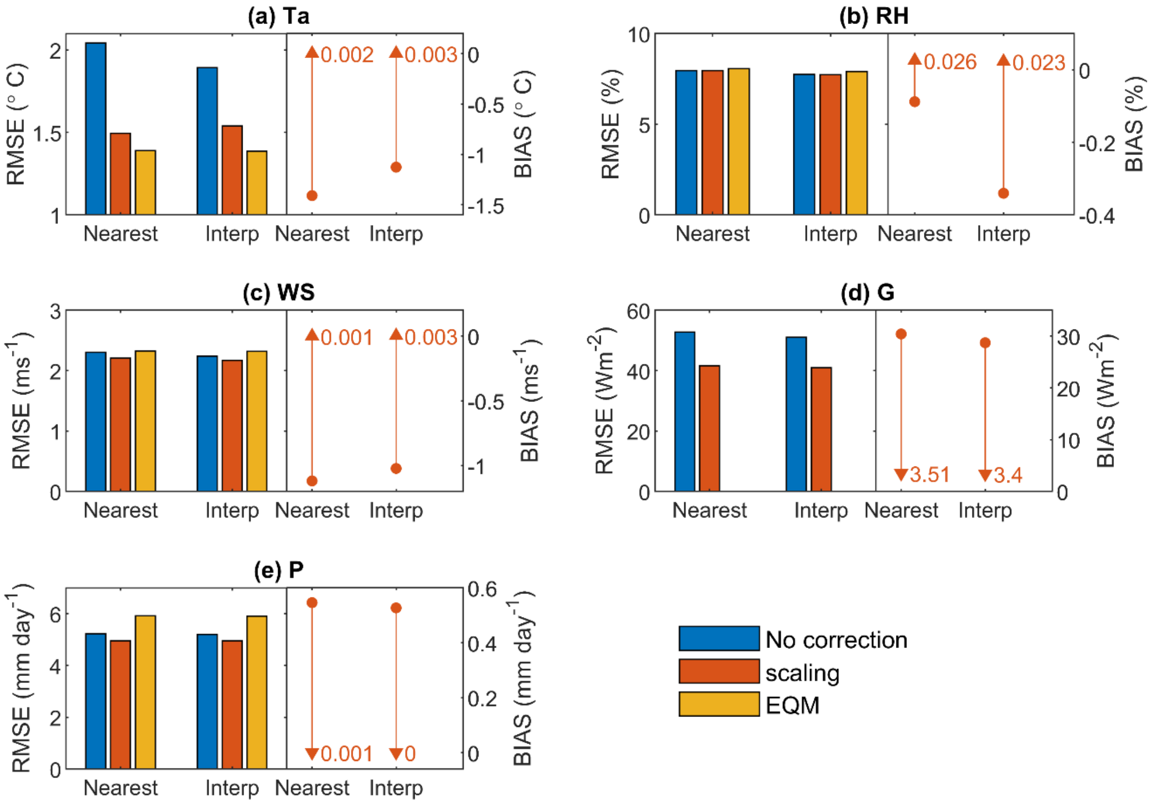

(a) Ta
RMSE (° C)
BIAS (° C)
0.002
0.003
(b) RH
RMSE (%)
BIAS (%)
0.026
0.023
(c) WS
RMSE (ms-1)
BIAS (ms-1)
0.001
0.003
(d) G
RMSE (Wm-2)
BIAS (Wm-2)
3.51
3.4
(e) P
RMSE (mm day-1)
BIAS (mm day-1)
0.001
0
Nearest
Interp
No correction
scaling
EQM

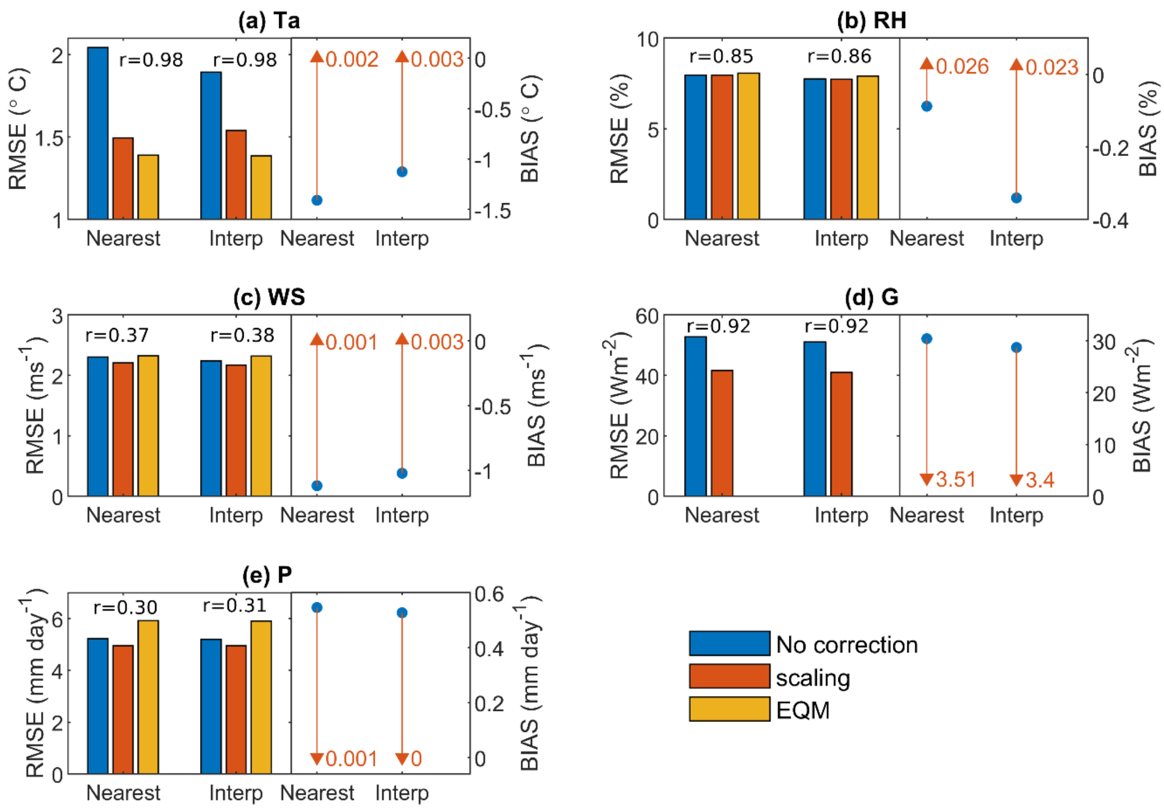

Figure 3. Comparison between NARR reanalyses and automated weather station (AWS) meteorological variables (2014-2016). Each panel shows the cross-validated root mean square error (RMSE) between daily NARR and AWS variables, before (blue) and after bias correction (red: scaling method; yellow: EQM method), for the ~~three~~ two NARR spatial interpolation methods (*Nearest*: nearest gridcell; *Interp*: bilinear interpolation). The cross-validated correlation coefficient (*r*), which changes little after bias correction, is shown on top of bars for each NARR interpolation method. Quivers on the left-hand side of ~~pannels~~panels show the cross-validated bias before (blue dot) and after (red triangle) applying the scaling bias correction method. ~~*Nearest*: nearest NARR gridcell; *Mean*: average of nine closest gridcells; *Interp*: IDW interpolation of nine closest gridcells).~~ (a) Air temperature; (b) ~~wind speed~~relative humidity; (c) ~~relative humidity~~wind speed; (d) incoming global solar radiation; (e) precipitation.

Monthly and annual averages of the ~~bias-corrected~~downscaled NARR variables from the nearest NARR gridcell ~~used to drive the mass balance model~~ are displayed in Figure 4. There is no visible trend in mean annual $T_{a,NARR}$ ~~T_a~~ ~~Ta~~ over the 30 years period except since 2010, but there is a noticeable increase in minimum temperatures, with e.g., only two years with a monthly mean colder than -15 °C in 2000-2015 compared to seven years prior to 2000. The positive trend seen in mean annual RH_{NARR} ~~RH~~ is driven by increasing annual minima while annual maxima show no trend, and so the seasonal amplitude decreases over time. The monthly RH_{NARR} ~~RH~~ averages decrease in July and August (mean = 72%) while winter months have higher values (mean = 80-82%) (Figure 4b). No ~~clear~~ noticeable trends occur in ~~annual~~ atmospheric emissivity ~~cloud cover~~ (ε_{NARR}~~CC~~) and G_{NARR}~~G~~, despite the observed trend in RH_{NARR} ~~RH~~ (Figure 4d, f). ~~The largest annual deviations in CC, e.g., after 2005, are reflected by inverse fluctuations in G, reflecting the attenuation of solar radiation by clouds.~~ A progressive decline in WS_{NARR}~~WS~~ occurs from ~~1979~~1984 onward, reaching the lowest annual value of the period in 1995 (~4.3 m s^{-1}) (Figure 4c). A more subdued increase in WS_{NARR}~~WS~~ occurs afterward until 2010, followed by a decline. Finally, mean monthly precipitation shows no long-term trend but significant seasonal and interannual variability (Figure 4e). ~~The seasonal amplitude decreases after 2000, driven by increasing seasonal minima and reduced maxima.~~ A slight increasing trend in P_{NARR}~~P~~ is noted in the last part of the record, since ~2000.

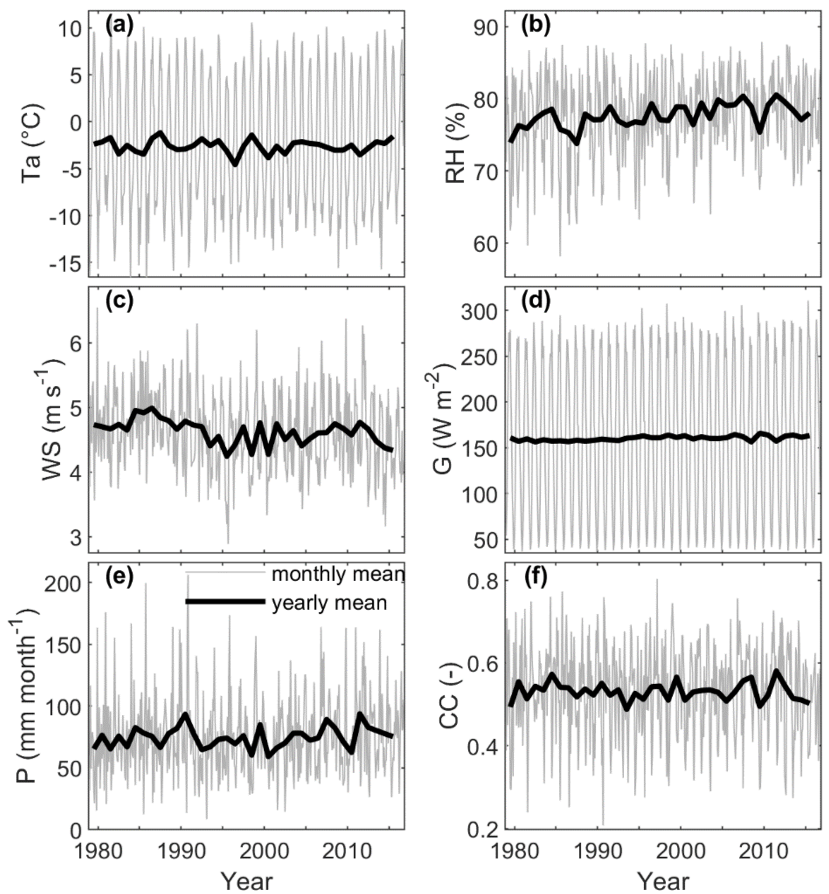
(a)
Ta (°C)
10
5
0
-5
-10
-15
(b)
RH (%)
90
80
70
60
(c)
WS (m s-1)
6
5
4
3
(d)
G (W m-2)
300
250
200
150
100
50
(e)
P (mm month-1)
200
150
100
50
0
monthly mean
yearly mean
(f)
CC (-)
0.8
0.6
0.4
0.2
1980
1990
2000
2010
Year

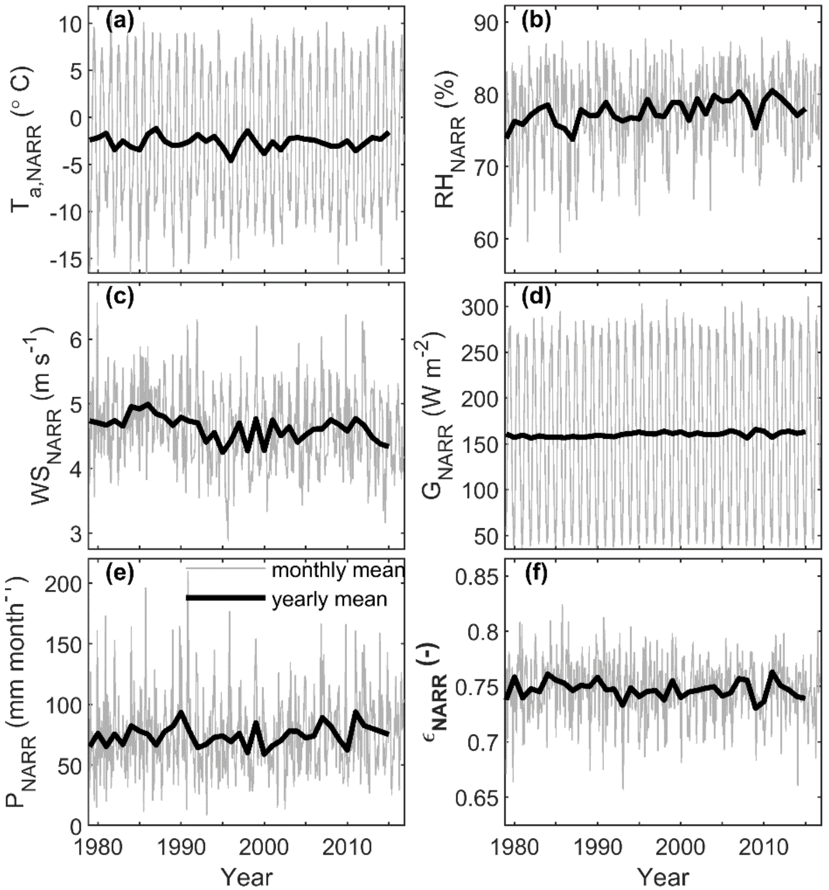

Figure 4. Downscaled NARR variables from the nearest NARR gridcell and used to drive the DEBAM model. Grey solid lines represent monthly means and black solid lines represent annual averages. (a) Air temperature; (b) relative humidity; (c) wind speed; (d) incoming global solar radiation; (e) total precipitation; (f) atmospheric emissivity.

4.3 Air temperature lapse rates

On-glacier diurnal air temperature lapse rates were found to vary between -0.55 °C 100 m^{-1} at night and to increase during the day, reaching a maximum of -0.34 °C 100 m^{-1} at midday (Figure 5a). The strength of the ~~temperature-elevation~~ linear relationship between air temperature and elevation, as measured by the correlation coefficient (*r*~~*R*~~), ~~is~~ is generally high (*r*~~*R*~~ > 0.95) but decreases slightly during daytime hours (*r*~~*R*~~ = 0.92). ~~Notably, the lapse rates were constant at night due to the absence of sunlight effects on surface temperature, while differential heating between the glacier tongue and the upper accumulation area and the associated local wind regimes (katabatic vs. valley wind) could explain the partial breakdown of the relationship and smaller lapse rates during the day.~~ While wind speed increased during the day, ~~katabatic~~ down-glacier winds prevailed, with little deviation of the wind direction within the day (Figure 5a). ~~On a monthly scale, the lapse rate, calculated from seven stations from the permanent network, varied between -0.58 °C 100 m^{-1} and -0.42 °C 100 m^{-1} without any systematic seasonal pattern (Figure 4b). The correlation for the monthly lapse rates is also more variable than for the diurnal lapse rates, varying between low values (R = 0.6) in winter to higher values (R = 0.94) in summer.~~ The wind blows dominantly down-glacier, ~~(katabatic)~~ with the relative wind direction showing a mixed contribution of the main accumulation area upwind of the AWS and the glacierized plateau North of the AWS. Stronger daytime down-glacier winds, possibly driven by a larger thermal gradient between the lower ice-free valley and the glacier, could result in down-glacier cooling and correspondingly shallower near-surface lapse rates, as shown on neighbouring Athabasca glacier (Conway et al., 2021). On a monthly scale, the lapse rate, calculated from seven stations from the permanent network, varied between -0.58 °C 100 m^{-1} and -0.42 °C 100 m^{-1} without any systematic seasonal pattern (Figure 5b). The correlation for the monthly lapse rates is also more variable than for the diurnal lapse rates, varying between low values (r~~R~~ = 0.6) in winter to higher values (r~~R~~ = 0.94) in summer. The mean on-glacier summer (May-August) lapse rate (-0.46°C 100 m~~Mean diurnal lapse rate anomalies, calculated as deviations from the average on-glacier lapse rate in Figure 5a, were added to the monthly lapse rates (Figure 5b) and used to distribute air temperature to the glacier surface.~~$^{-1}$) was very close to that calculated from the permanent weather station network for the same period (-0.49 °C 100 m^{-1}), which gives confidence in extrapolating the monthly lapse rates from the network to the glacier surface. Superimposing the on-glacier diurnal lapse rates anomalies onto the mean monthly lapse rates allowed to better represent the diurnal changes associated with the glacier wind.

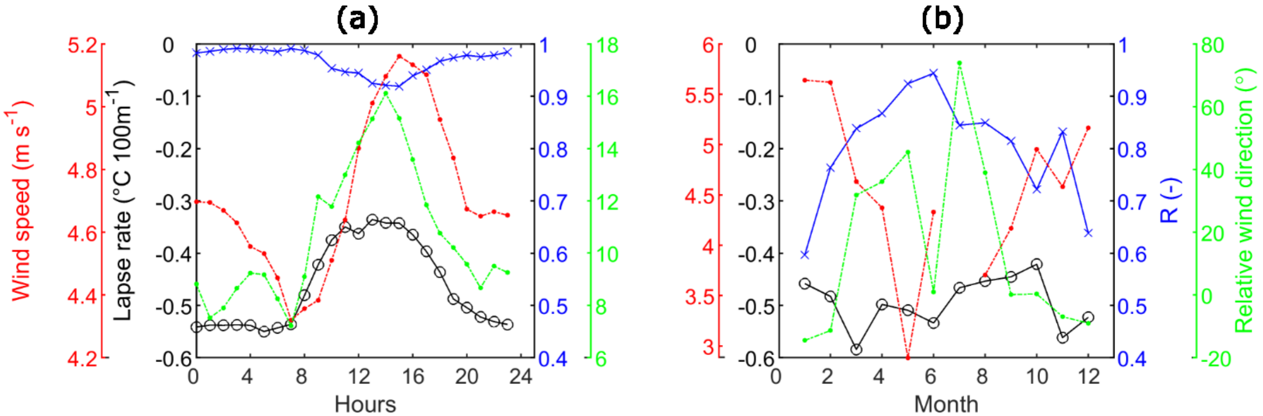

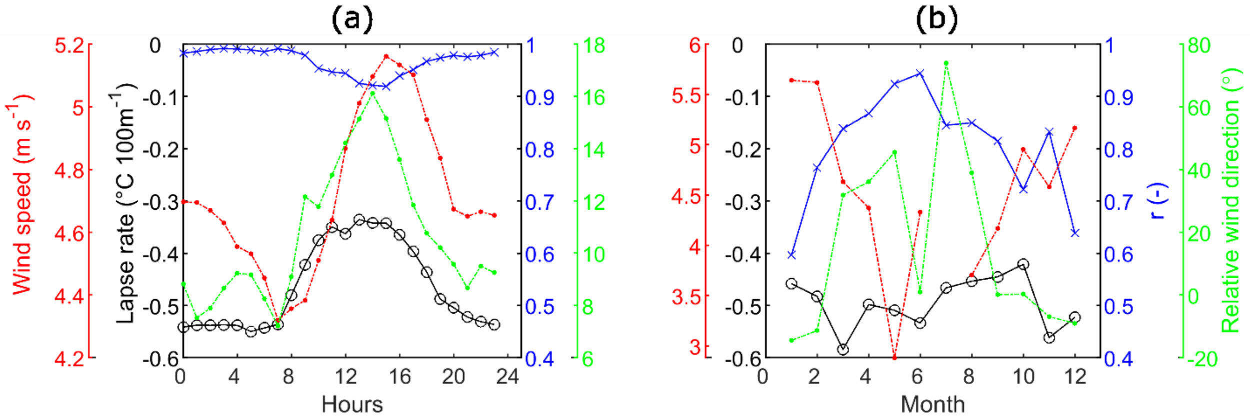

Figure 5. Calculated air temperature lapse rates. The black axis represents the air temperature lapse rate in °C 100 m^{-1}, the blue axis represents the correlation (*r*~~R~~) between air temperature and elevation, the red axis represents wind speed and the green axis the wind direction relative to the main glacier axis (0° = down~~up~~-glacier, 180° = ~~down~~up-glacier). (a) Diurnal temperature lapse rate from the five HOBO^{TM} microloggers installed on ablation stakes from May to August 2015 (See Figure 1). (b) Seasonal variation of the lapse rate derived from ~~seven~~ the permanent weather stations (see Figure 1). ~~The~~ W~~w~~ind speeds and directions ~~data~~ on both panels are from the glacier AWS.

4.4 Model performance

4.4.1 Comparison with glaciological mass balance

The mass balance simulated with DEBAM was compared with point glaciological mass balance observations available between 2012 and 2016. Overall, the seasonal and annual mass balance components are well simulated by the model, with most observations lying near the 1:1 line and with Nash-Sutcliffe Efficiency (NSE, Nash and Sutcliffe, 1970) coefficients of 0.84 for the winter balance (b_w, ~~(~~n=49), 0.83 for the summer balance (b_s, ~~(~~n=12) and 0.91 for the annual balance (b_a~~-~~, ~~(~~n=12) (Figure 6). Before the adjustment of the atmospheric emissivity calculation in the $LW\downarrow$ ~~in~~ equation (~~c.f.~~ ~~see Sect~~see Sect.~~.~~ 3.3.3), the model tended to overestimate melt in the accumulation zone and underestimate it in the ablation zone. The NSE was increased by 0.04 for b_w, 0.07 for b_s and 0.06 for b_a after modifying the parametrisation. The modelled b_w was underestimated in 2016 in the upper part of the glacier and overestimated in the lower part, suggesting that the precipitation gradient for that year significantly differed from the other years. This shows one limitation of the current model configuration, which uses a constant, average precipitation lapse rate to distribute precipitation over the glacier surface. 2016 was a dry year, with the ultrasonic gauge on the glacier AWS recording a small amount of snow accumulation during winter (25 cm in 2016 vs. 135 cm in ~~AWS:~~ 2015~~ ~~)~~=~~. ~~135 cm, 2016 = 25 cm). Data~~ Observations from ablation stakes are more limited, and despite the overall good model performance as seen by the linear relationship between observed and simulated b and the high NSE values, modelled b_s and b_a were slightly underestimated in 2014 and 2016 and overestimated in 2015 compared to ~~the~~ observations (Figure 6).

The simulated mass balance gradient compares generally well with observations for the three years with available b_a measurements (Figure 6d). Overestimation of ablation at the two ablation stakes from 2014 is apparent, however, leading to underestimated mass balance (b_a) in the upper glacier for that year. The equilibrium line altitude (ELA) was ~2600 m for 2014-2016, which is near the average ELA of 2587 m simulated for the entire 1979-2016 period. The mean simulated mass balance gradient for the three validation years (2014-2016) was 0.98 ~~c~~m w.e. 100 m^{-1} in the ablation zone, with a steeper inflection below the ELA, and decreasing to 0.32~~1~~ ~~c~~m w.e. 100 m^{-1} in the accumulation zone (up to 2900 m, where the model is constrained by observations, see Figure 6d). Long-term values were 0.96 ~~c~~m w.e. 100 m^{-1} and 0.31~~29~~ ~~c~~m w.e. 100 m^{-1} for 1979-2016, yielding a balance ratio (BR: the ratio of ablation to accumulation area balance gradients) of 3.10~~34~~. A higher BR value implies that a smaller ablation area is needed to balance inputs in the accumulation area (Benn and Evans, 2014). ~~This~~ The BR value simulated for Saskatchewan Glacier ~~value~~ is rather high, i.e. triple that computed by Rea (2009) for the 'North America – Eastern Rockies' region (mean BR ± std = 1.11 ± 0.1). The simulated BR ~~and~~ is ~~closer~~within the range, but still on the high side, of ~~to typical~~ values found ~~(BR = 2.09 ± 0.93)~~ for 'North America West Coast' glaciers (mean BR ± std = 2.09 ± 0.93) which have a more humid climate ~~than 'North America – Eastern Rockies' (BR = 1.11 ± 0.1)~~ (Rea, 2009). ~~(Demuth and Horne, 2018; Tennant and Menounos, 2013)This high value implies that a smaller ablation area is needed to balance inputs in the accumulation area (Benn and Evans, 2014).~~

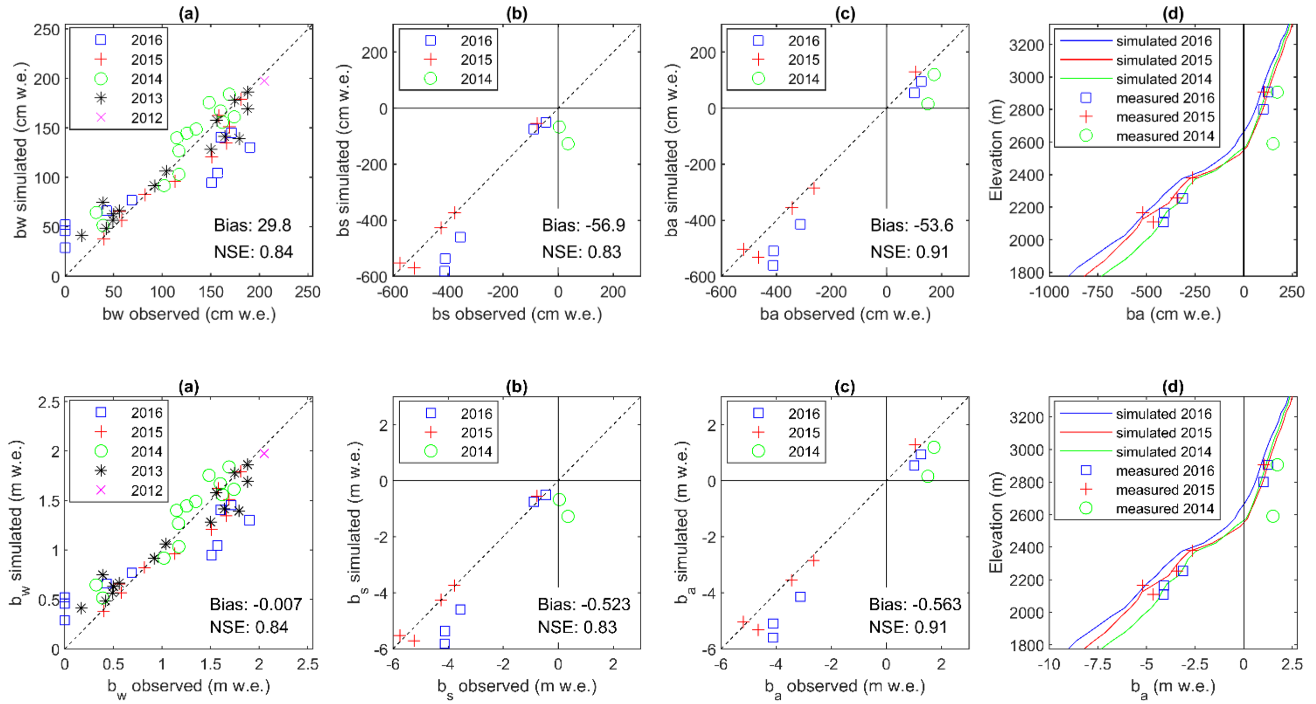

Figure 6. Simulated mass balance compared with point mass balance observations available between 2012 and 2016. (a) Winter balance (b_w); (b) summer balance (b_s, only available since 2014); (c) annual balance (b_a, since 2014). ~~Mass balance is expressed in centimeters water equivalent (cm w.e.).~~ The dashed line is the 1:1 relationship. (e) Simulated vs. observed annual mass balance gradient between 2014 and 2016.

4.5 Mass balance reconstruction and comparison with geodetics estimates

The simulated annual specific (glacier-wide) conventional mass balance (B_{a_c}) was overall negative throughout the period (mean = -0.72 m w.e. a^{-1}) with pronounced interannual variability (std = 0.57 m w.e. a^{-1}) (Figure 7a). The cumulative conventional mass balance simulated with the multitemporal DEMs agrees well with the geodetic estimates (Figure 7b). The simulated and geodetic cumulative mass balance were -26.79 m w.e. and -25.59 ± 8.44 m w.e., respectively, for 1979-2016. The cumulative error in the geodetic estimates increases in 1999 due to the large error in the SRTM DEM, even though it was coregistered to the high-quality WV2 2010 DEM (Supplementary Material).

The ~~static~~ simulation with the 1979 reference DEM (B_{a_r1979}), when the glacier was thicker and larger, results in a larger cumulative mass loss (~ -3 m w.e. over 37 years) than when using the 2010 DEM (B_{a_r2010}~~w~~) with the smallest historical extent (Figure 7b). The difference essentially arises from the larger extent in 1979 which provides more area available for melting at lower elevations. The ~~dynamic~~conventional mass balance ~~(B_{a_c})~~simulation remains between the limits of the two-endmember ~~static~~reference simulations, with a difference in cumulative mass loss of ~ ± 1.4 m w.e at the end of the period. ~~(Figure 7a).~~

The effect of dynamical adjustment on B_{a_c} was obtained ~~as the difference~~by ~~differentiating between the dynamical simulation (multitemporal DEMs),, which account for the dynamical response of the glacier, and with the 1979 static simulation (fixed 1979 DEM)~~subtracting B_{a_r1979} from B_{a_c}. The effect was overall small from 1986 (first DEM update) onward (mean = 0.06 m w.e. a^{-1}), but accelerated over the last 15 years (Figure 7a). ~~(Figure 7a). The simulated mass balance with the multitemporal DEMs is in good general agreement with the geodetic estimates (Figure 7b). The cumulative error if the geodetic estimates increases in 1999 due to the large error in the SRTM DEM, even though it was coregistered to the high-quality WV2 2010 DEM (supplementary material). The static simulation with the 1979 DEM, when the glacier was thicker and larger, results in a larger cumulative mass loss (~ -3 m w.e. over 37 years) than when using the 2010 DEM with the smallest historical extent. Essentially the larger extent in 1979 provides more area available for melting at lower altitudes~~elevations~~. The dynamic mass balance simulation remains between the limits of the two-endmember static simulations, with a difference in cumulative mass loss of ~ ± 1.4 m w.e at the end of the period.~~

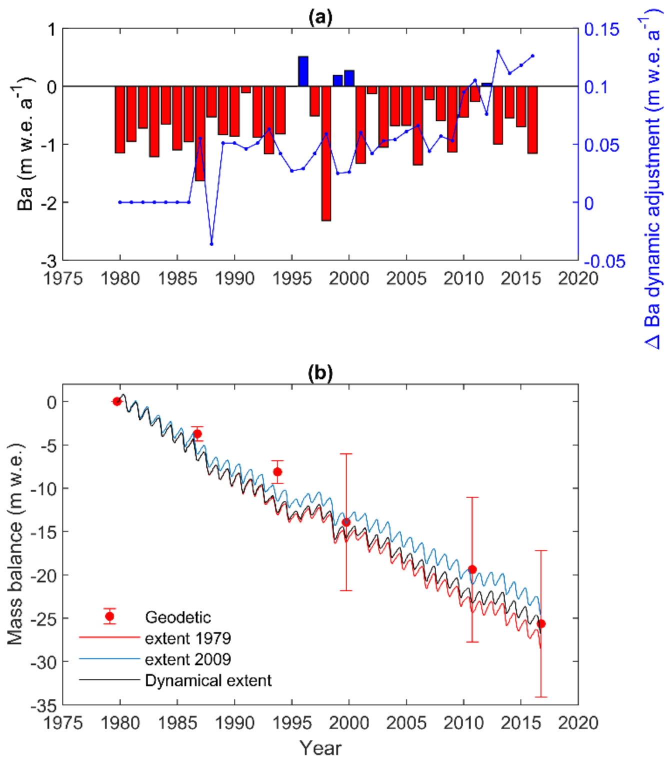

Figure 7. Simulated mass balance compared with geodetic estimates. (a) Conventional a~~A~~nnual glacier-wide mass balance (B_{a_c}) from the dynamical simulation (multitemporal DEMs). The blue curve represents the effect of dynamical adjustment on B_{a_c}. (b) Cumulative mass balance from ~~static~~reference (red: 1979, blue: 2010) and ~~dynamic~~conventional (black: multitemporal DEM) simulations. Error bars represent one-sigma cumulative confidence intervals around the cumulative geodetic mass balance. ~~The green trace represents the simulation forced with topographically-corrected NARR Ta and P, but without bias correction. (c)~~

~~**Sensitivity of simulated mass balance to parameter uncertainty. Coloured envelopes represent the cumulative uncertainty and the coloured error bars on the right show the effect of parameter uncertainty on the 1979-2016 cumulative mass balance.**~~

4.6 Model s~~S~~ensitivity to uncertainties in parameters ~~uncertainty~~ and NARR ~~downscaling~~forcings

~~4.6~~4.6.1 Sensitivity to NARR interpolation and bias correction method

Forcing the mass balance with the nearest ~~raw~~ NARR grid cell or with the bilinearly-interpolated NARR forcings resulted in negligible differences on the simulated cumulative balance, when both types of NARR forcings were bias-corrected by station observations (Figure 8a). However, when station data were not used for bias correction and the NARR precipitation and air temperature were only lapsed to the station elevations using the mean observed lapses rates, the simulated mass loss was overestimated relative to geodetic observations. However, the lapsed interpolated NARR forcings resulted in a closer agreement with the geodetic observations than when using the lapsed NARR forcings from the nearest gridcell.~~, after correcting $_{NARR}$ Ta and P_{NARR} P for the elevation difference between the NARR gridpoint and the reference weather station, resulted in a significant cumulative error in simulated B_a;, with the cumulative B_a in 2016 being more negative by 15 m w.e. compared with the simulation with the bias-corrected NARR (Figure 8Figure 7b).~~

~~**Sensitivity to NARR bias correction**~~

…

4.6.2 Sensitivity to NARR forcings

The model sensitivity to the type of NARR variable used for forcing was investigated for the glaciological year 2014-2015, when both complete on-glacier AWS data and point mass balance were available (Figure 8b, c). Results show that the model was most sensitive to air temperature, ~~while~~whereas replacing the other NARR forcings (RH_{NARR}, WS_{NARR}, G_{NARR}) by their AWS counterparts had a comparatively small effects on the ~~simulated point mass balance~~mass balance validation against observations~~s~~. Hence, despite the good correlation between NARR and AWS air temperatures and the low errors following bias-correction (Figure 3), the model remains most sensitive to air temperature while it is less sensitive to other variables that showed comparatively higher errors with respect to AWS observations, such as wind speed (Figure 3).

4.6.3 Sensitivity to model parameters

The model parameter sensitivity analysis shows that the simulated mass balance ~~is~~was most sensitive to the uncertainty in the precipitation lapse rate (±4% 100 m^{-1}) followed by the ice aerodynamic roughness length (z_{0_ice}: ±1 mm) (Figure 8d). The sensitivity to uncertainties in ice albedo (α_{ice}: ±0.03) and the snow aerodynamic roughness length (z_{0_snow}: ±1 mm) were smaller and of similar magnitude. Large changes in simulated cumulative mass balance occurred when considering an order of magnitude change on aerodynamic roughness lengths. While spatial variability in z_0 of that order is possible across a single glacier due to heterogeneous snow, an even more so ice surface morphology (Chambers et al., 2020), the resulting uncertainty on the glacier wide average ~~(glacier wide)~~ z_0 ~~is~~ would be much lower (Brock et al., 2006; Chambers et al., 2020; Munro, 1989)~~{Munro, 1989 #75}. {Brock, 2006 #74{Munro, 1989 #75} {Chambers, 2020 #94}74}~~Nonetheless, these results clearly show that a careful assessment of the precipitation lapse rate and ice aerodynamic roughness length are crucial to derive a reliable long-term mass balance reconstruction. Constraining these two parameters as well as the ice albedo and the snow aerodynamic roughness length against observations and ancillary information is thus pivotal to reliably simulate the recent direct mass balance observations (Figure 6) and long-term geodetic estimates (Figure 8).

~~Sensitivity to model parameters~~

~~Results from the parameter sensitivity analysis show that the simulated mass balance is most sensitive to the uncertainty in the precipitation lapse rate (±4% 100 m^{-1}) followed by the ice aerodynamic roughness length (z_{0_ice}: ±1 mm) (Figure 8Figure 7c). The sensitivity to uncertainties in ice albedo (α_{ice}: ±0.03) and the snow aerodynamic roughness length (z_{0_snow}: ±1 mm) were smaller and of similar magnitude (refer to the overlap of the coloured envelopes in (Figure 7Figure 8c). These results clearly show that a careful assessment of the precipitation lapse rate and ice aerodynamic roughness length are needed to derive a~~

~~reliable long-term mass balance reconstruction. Constraining these two parameters as well as the ice albedo and the snow aerodynamic roughness length against the observations is thus pivotal to replicating the recent direct mass balance observations (Figure 6) and long-term geodetic estimates (~~Figure 8~~Figure 7).~~

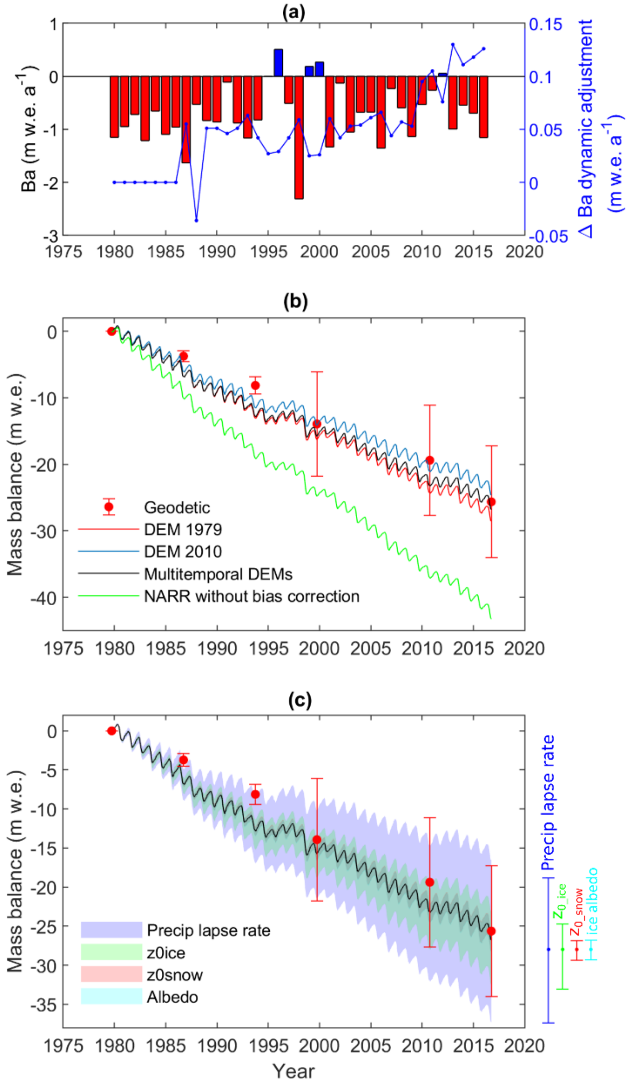

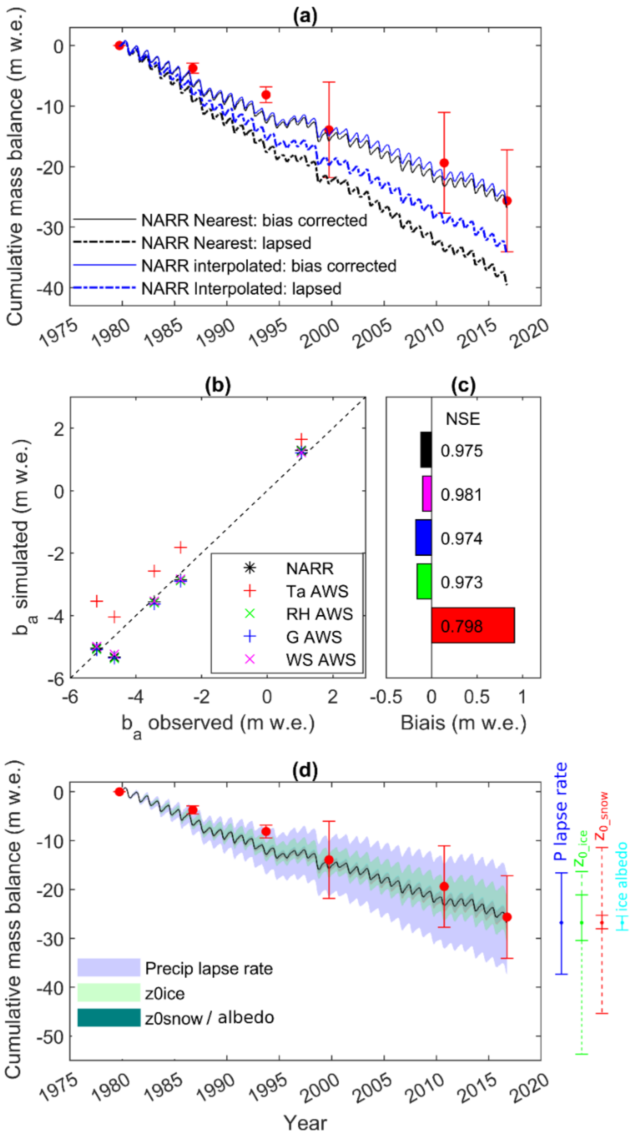

Figure 8. Model sensitivity to NARR forcings and ~~meteorological forcings and~~ model parameters uncertainty. (a) Sensitivity to NARR interpolation method (nearest gridcell: black, vs. bilinear interpolation: blue) and bias correction method (continuous line: bias corrected with AWS, vs. stippled line: P_{NARR} and $T_{a,\ NARR}$ ~~Ta~~ lapsed to the DEM). (b) Sensitivity to NARR forcings: measured vs. simulated point mass balance for glaciological year 2014-2015 after replacing NARR ~~meteorological~~forcings ~~variables~~ ($T_{a,\ NARR}$~~Ta~~, RH_{NARR}, G_{NARR}, WS_{NARR}) one at a time by AWS observations; (c) corresponding mean error (bias, m w.e., coloured bars) and Nash-Sutcliffe efficiency scores (labels). (d) Sensitivity to model parameter uncertainty. Coloured envelopes represent the cumulative uncertainty; coloured error bars on the right show the effect of parameter uncertainty on the cumulative mass balance in 2016. Error bars for ice (green) and snow (red) roughness lengths correspond to a ± 1mm measurement uncertainty; the dotted error bars extend the uncertainty to ± one order of magnitude.

~~**Figure 7. Simulated mass balance compared with geodetic estimates. (a) Annual glacier-wide mass balance (*Ba*) from the dynamical simulation (multitemporal DEMs). The blue curve represents the effect of dynamical adjustment on *Ba*. (b) Cumulative mass balance from static (red: 1979, blue: 2010) and dynamic (black: multitemporal DEM) simulations. Error bars represent one-sigma cumulative confidence intervals around the cumulative geodetic mass balance. The green trace represents the simulation forced with topographically-corrected NARR Ta and P, but without bias correction. (c) Sensitivity of simulated mass balance to parameter uncertainty. Coloured envelopes represent the cumulative uncertainty and the coloured error bars on the right show the effect of parameter uncertainty on the 1979-2016 cumulative mass balance.**~~

4.7 Energy and mass fluxes

Monthly energy balance shows that the sensible heat flux (Q_S) ~~(Q_S)~~ dominates~~s~~ energy gains throughout most of the year (Figure 9). The contribution of Q_S ~~Q_S~~ is fairly constant throughout the year, increasing only slightly in July-August and decreasing slightly in spring (March-May). The contribution of the net solar radiation flux (SW^*) increases systematically from low values in winter (November-February) when the sun angle is low and the glacier is covered by highly reflective snow, to peak values in July-August when the sun angle is high and low-albedo ice is exposed in the ablation area. Only in July and August does the net solar radiation (SW*) becomes the dominant energy source. The latent heat flux (Q_L ~~Q_L~~) is small over Saskatchewan Glacier, due to the generally high relative humidity (see Figure 2). Q_L ~~Q_L~~ is positive on average and highest in summer, reflecting the predominance of deposition and condensation processes over sublimation. Q_L ~~Q_L~~ represents a small, but non-negligible (7%) heat gain throughout the year, which reaches 11.5% in July-August. Energy loss occurs mainly by radiative cooling, i.e. through a negative net longwave radiation flux (LW^*). Lower air and surface temperature respectively reduce the incoming atmospheric longwave radiation and outgoing longwave emissions from the glacier surface, thereby reducing LW^* in winter. LW^* increases somewhat in summer (June-August), mainly because the glacier surface is near its melting point, limiting longwave radiation losses. The energy supplied by rain (Q_R ~~Q_R~~) has a negligible influence on the energy balance. Melting (Q_M ~~Q_M~~) predominantly occurs between May and October and peaks in July-August, due to the elevated SW^*, Q_S ~~Q_S~~ and Q_L ~~Q_L~~ fluxes, and radiative cooling ($LW\uparrow$ ~~out~~) limited by the melting surface.

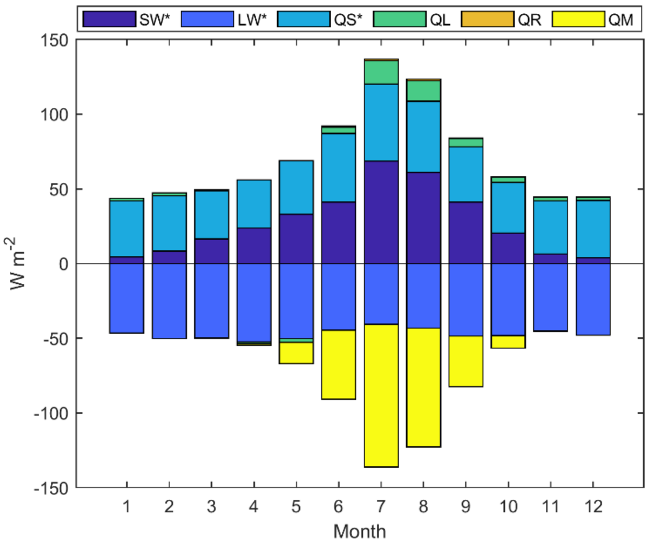

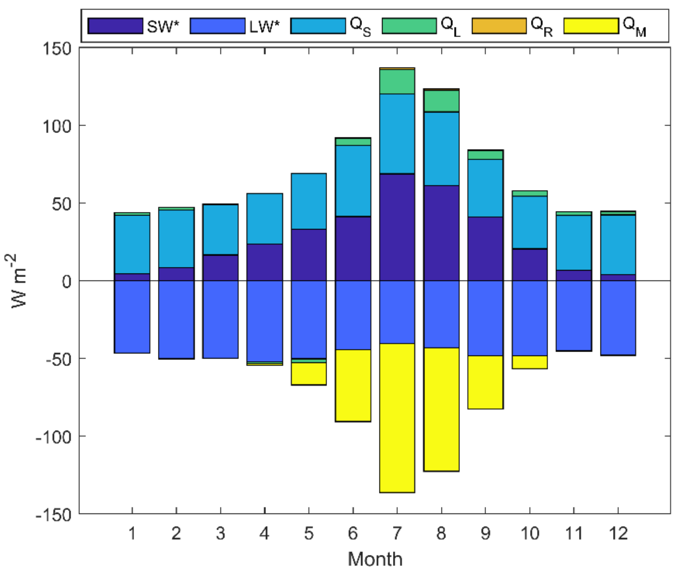

Figure 9. Mean seasonal cycle of simulated surface energy balance on Saskatchewan Glacier between 1979-2016 from the multi-temporal DEM simulation.

Four processes influence mass balance during the year (Figure 10a). Snowfall and snow accumulation dominate during the accumulation season (October-April). Melt mainly occurs from May to October and peaks in July-August in response to the positive surface energy balance (Figure 9). Deposition/condensation and sublimation fluxes are small. Net deposition predominates while net sublimation occurs in the spring (April-June), when there is high incoming radiation and the upper reaches of the glacier have not yet reached the melting point (Figure 10a). Although the Q_L ~~QL~~ heat flux was found to be ~~non~~

~~negligible~~non-negligible during summer (Figure 9), the resulting mass loss is itself negligible compared to melting because the latent heat of sublimation/deposition is seven times larger than that for melting. Moreover, the latent heat flux has a pronounced diurnal cycle, switching from deposition at night when cooling of moist air causes the vapour pressure to increase relative to the melting glacier surface, while daytime heating reverses the vapour gradient between the glacier surface and the atmosphere, causing sublimation (Figure 10b). Hence the two regimes tend to compensate each other but~~. Nevertheless, the~~ nighttime deposition slightly dominates daytime sublimation, leading to a net positive deposition/condensation flux on average to the glacier surface.

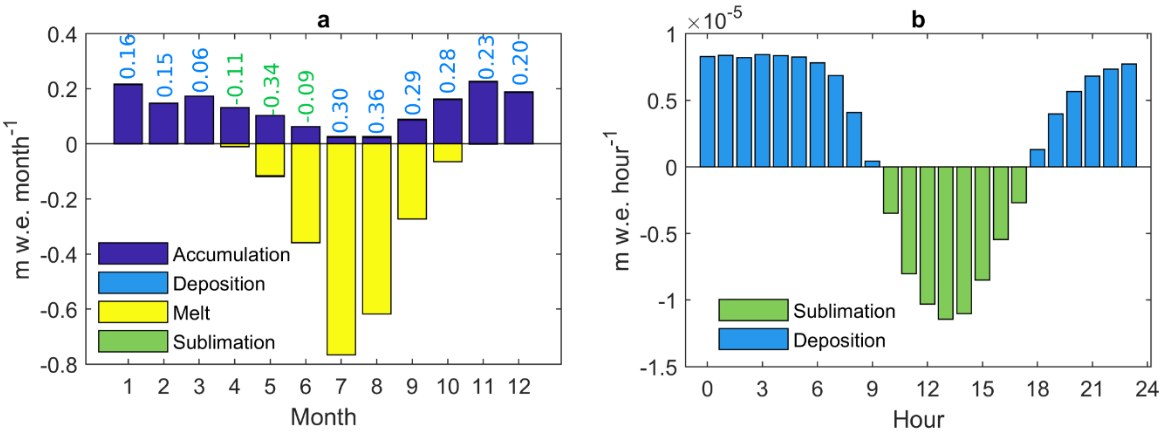

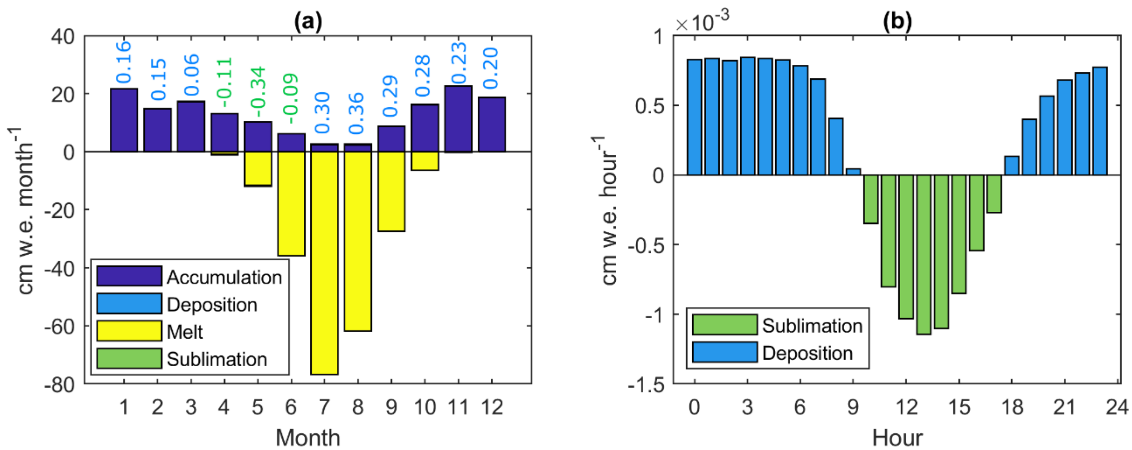

Figure 10. Mean simulated mass fluxes on Saskatchewan Glacier between 1979-2016 ~~using~~ using the multi-temporal DEMs. (a) Mean monthly fluxes; deposition and sublimation fluxes being much smaller, they are ~~also~~ indicated as numbers in ~~(~~cm w.e. month $^{-1}$~~)~~. (b) Mean diurnal cycle in deposition/condensation and sublimation.

~~Simulated spatial~~Spatial ~~mass balance~~ patterns of the simulated reference mass balance (B_{a_r2010}) (Figure 11) show an annual average snowfall ~~average~~ of 1.54 ~~c~~m w.e over the glacier with a minimum of 0.30 ~~c~~m w.e near the toe, to ~3~~00~~ ~~c~~m w.e. over the upper reaches. Annual ~~ice~~ melt can reach 7.86 ~~c~~m w.e. a^{-1} at the glacier margin and 0.54 ~~c~~m w.e. a^{-1} in the upper accumulation zone. Net deposition/condensation predominates on average over the glacier, but fluxes are small (< 0.03 ~~c~~m w.e. a^{-1}), while net sublimation only occurs on the upper reaches of the glacier, mostly in the Spring (Figure 11c, Figure 10a), corresponding to areas with high incoming solar radiation (Supplementary Figure S4). On average, melting losses (mean = -2.22 ~~c~~m w.e. a^{-1}) exceed snow precipitation gains (~~+~~1.54 ~~c~~m w.e. a^{-1}) and the small condensation gain (mean = 0.0~~+~~1 ~~c~~m w.e. a^{-1}), yielding a mean negative reference annual balance (B_{a_r2010}) of ~~-~~-0.67~~7~~ ~~c~~m w.e. a^{-1}.~~).~~

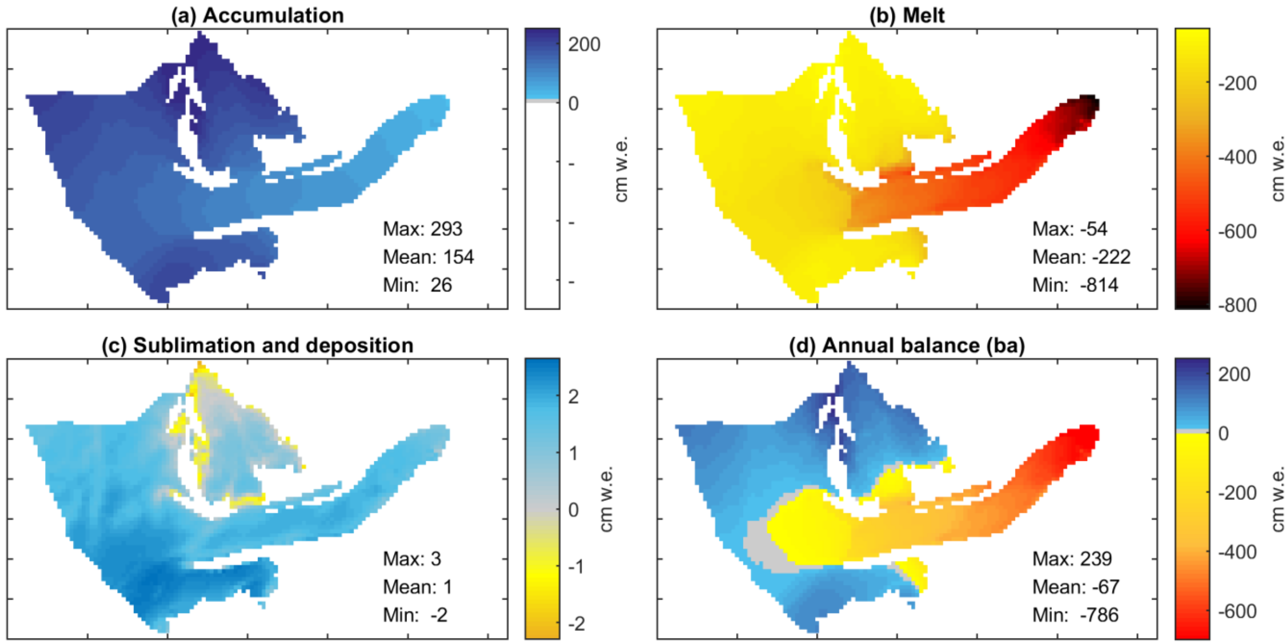

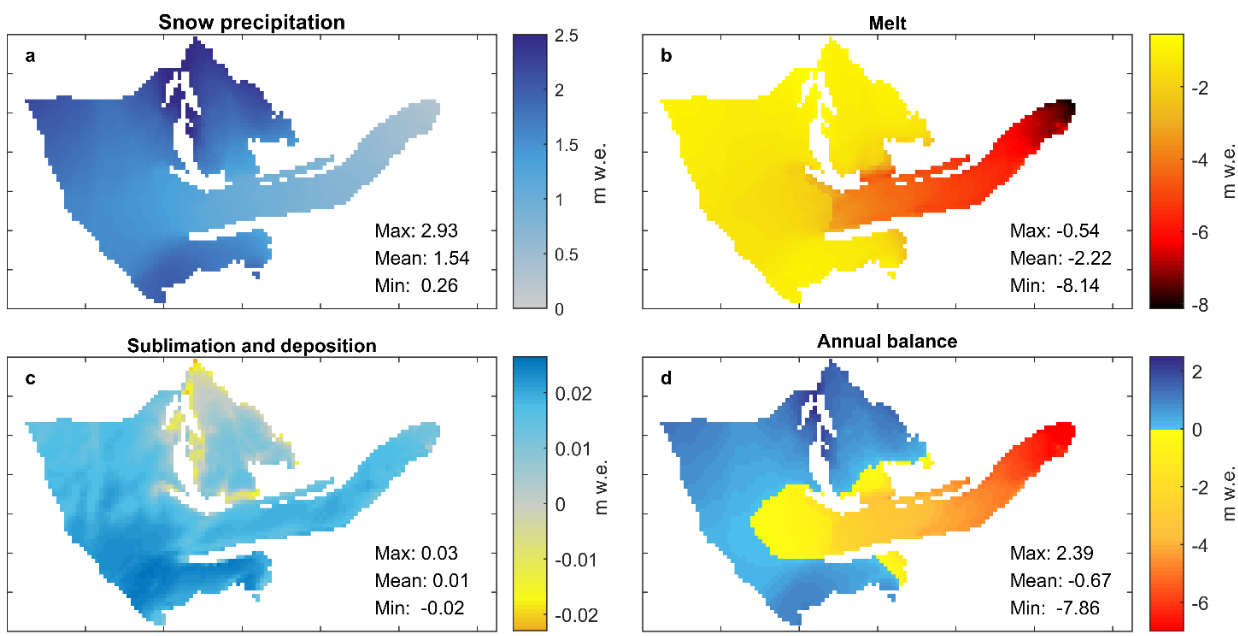

Figure 11. Simulated average spatial patterns of reference annual mass balance (B_{a_r2010}, in cm w.e.) on Saskatchewan Glacier between 1979-2016. (a) Snow accumulation; (b) melt; (c) sublimation and deposition; (d) annual balance. The accumulation zone on

(d) is delineated by the positive blue colour scale, the ablation zone by the negative yellow/red scale~~ and the area of neutral balance in grey ($b_a = 0$)~~.

4.8 Climate sensitivity analysis

The static sensitivity of mean mass balance (B_{a_r2010}) components to ~~various~~ climate perturbations (ΔT_a~~Ta~~ = 0 to +7 °C and ΔP = -20 to +20%) ~~was examined using the 2010 DEM as reference glacier geometry~~is shown in ~~(~~Figure 12~~)~~. The reference scenario (1981-2010) yields an average annual mass loss ~~(B_a)~~ of -0.68 m w.e. a^{-1} (Figure 12c). The response surface for B_{a_r2010} ~~B_a~~ shows that the glacier-wide mass balance is sensitive to changes in air temperature, and much less sensitive to changes in precipitation (Figure 12c). The ΔB_a contours also become steeper and narrower with increased warming, which indicates a reduced sensitivity to precipitation and increased sensitivity to temperature, respectively. The seasonal mass balance response sufaces help to understand the B_{a_r2010} ~~B_a~~ sensitivities (Figure 12a,b). The B_{w_r2010} response surface shows that a precipitation increase of +20% can buffer the negative impact of warming on B_w up to +3 °C of warming, but only up to +0.5 °C ~~only~~ for B_{a_r2010}. Moreover, a warming of more than +6 °C with no change in precipitation would supress net accumulation in winter, given the current glacier extent (2010) (Figure 12a). The sensitivity of winter mass balance to temperature changes also increases markedly with warming, as seen by the progresive tightening of the contours in Figure 12a. This is interpreted to result from decreasing accumulation due to the increasing shift from snowfall to rainfall and increased ablation during winter (Oct.-April) due to earlier disapearance of the snow cover under more pronouced warming. Convers~~ea~~ly, the temperature sensitivity of summer mass balance (B_{s_r2010}) increases only slightly with the warming scenario, and the steep contours in Figure 12b suggest a small sensitivity to precipitation changes. The increased temperature sensitivity of ~~B_a~~B_{a_r2010} with warming indicated in Figure 12c is therefore mainly attributed to decreasing accumulation from reduced snowfall fraction and increased winter ablation as the climate warms and the snow cover retreats up-glacier earlier in the Spring (Figure 12a).

The IPCC RCP scenarios for the mid (2041-2070) and late (2071-2100) 21st century were overlain~~pped~~ onto the response surfaces to show the most likely future climate trajectories~~ given by the latest projections from climate models~~. The RCP projection have significant uncertainities, as shown by their wide ~~5-95%~~ confidence intervals, and the annual mass balance change can vary by as much as ±3 m ~~.~~w.e. a^{-1} within a single scenario. This illustrates the usefulness of scenario-free response surfaces to assess glacier mass balance sensitivity to climate as a background to evolving climate projections (Aygün et al., 2020b; Prudhomme et al., 2010). Nontheless, given the current ensemble climate scenarios, the reference ~~(static)~~ mass balance could decrease by -0.5 to -2.0 m w.e a^{-1} by the mid-century, and by -0.5 to -4 m w.e a^{-1} by the end of the century, relative to baseline conditions (B_{a_r2010} = -0.68 m w.e. a^{-1}) and depending on the RCP scenario considered.

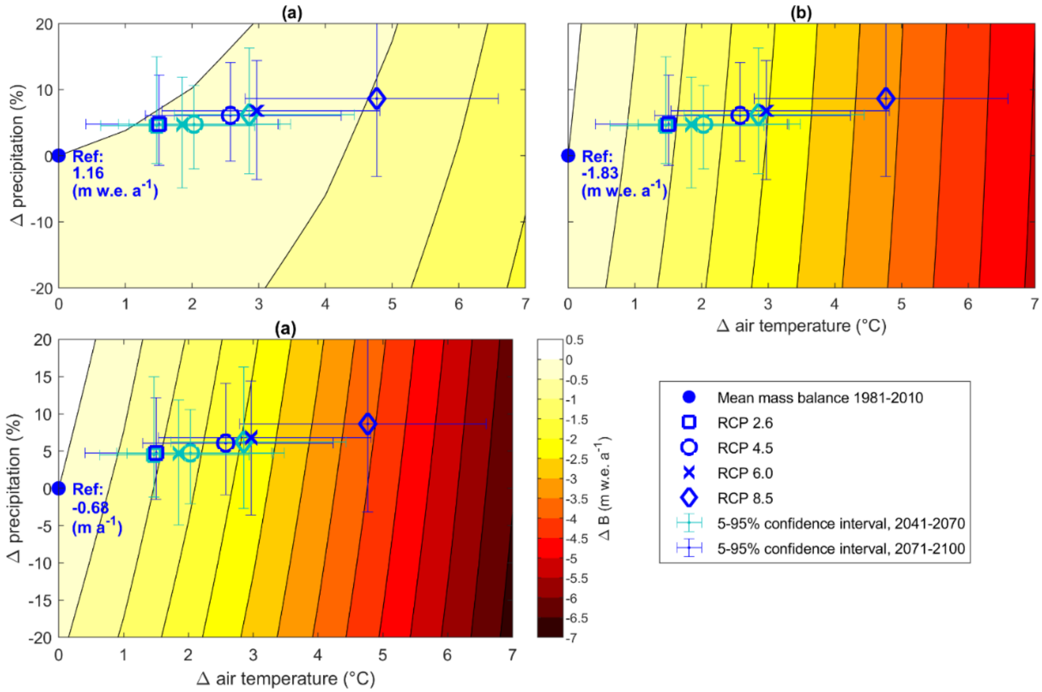

Figure 12. ~~Static~~ Reference (2010 ~~DEM~~) mass balance sensitivity to prescribed changes in regional mean air temperature between 0 to 7 °C and precipitation between -20 to +20%, which encompass IPCC ~~representative concentration pathways (~~RCP~~)~~ ensemble scenarios ~~+~~2.6, ~~+~~4.5, ~~+~~6.0 and ~~+~~8.5 for the mid (2041-2070: dark blue) and late (2071-2100: light blue) 21st century. The mean seasonal and annual mass balance are shown for the reference period 1981-2010. (a) Winter balance (B_{w_r2010}); (b) summer balance (B_{s_r2010}); (c) annual balance (B_{a_r2010}).

Since ~~B_a~~ mass balance displays a large sensitivity to temperature and because glacier melt is the outcome of complex glacier-atmosphere energy exchanges, the sensitivity of energy and mass fluxes to warming alone was further investigated in ~~(~~Figure 13~~)~~. ~~Under~~ The ~~warming scenarios with no changes in precipitation, a~~increasingly more negative mass balance in response to warming is dominated by increased melting (~93%), while increasing condensation/deposition accounts for ~ -3% (mass gain) of the net annual mass changes in response to warming (Figure 13a, b). Warming alters the precipitation phase, with the snowfall ratio decreasing non-linearly from 0.80 under present climate to 0.47 at ΔT_a ~~Ta~~ +7°C (Figure 13c). This progressive conversion ~~from~~ of snowfall to rainfall accounts for ~10 % of the mass changes in response to warming (Figure 13b).

The total energy input to the glacier surface increases with warming temperatures, and thise ~~increased~~ energy surplus is predominantly used for melting (Q_M), ~~QM),~~ which shows a non-linear increase with respect to warming (Figure 13d, e). Interestingly, the increase in energy supply with warming is mainly driven by an increase in net solar radiation (SW*) and latent heat flux (Q_L ~~QL~~), with more subdued increases in the temperature-dependent sensible heat (Q_S ~~QS~~) and net longwave radiation fluxes (LW*) (Figure 13e). Since cloud cover remained unchanged in the sensitivity experiments, the increase in SW* with warming is entirely driven by the decreasing albedo, as snow cover duration on the glacier decreases (Figure 13c). Since the relative humidity also remained~~s~~ constant in our sensitivity analyses, warming leads to higher atmospheric vapor pressures ~~and~~ since ~~because warming increases~~ the saturated vapor pressure of the air increases with warming~~, warming leads to higher atmospheric vapor pressures~~. Since the glacier surface is contrained to the melting temperature (0 °C) during a large part of the year, the increase in surface saturated vapor pressure in response to warming will, on average, be less than that of the atmosphere, causing the vapor pressure gradient to increase and boost Q_L ~~QL~~ fluxes (condensation/deposition) to the surface. Similar reasoning applies to Q_S ~~QS~~, i.e., the near surface temperature gradient will increase in response to atmospheric warming. While the rainfall ratio increases with warming, its influence on the energy balance is insignificant (Figure 13e), but the reduced snowfall greatly impacts winter accumulation (Figure 12a). Increasing net solar radiation (SW*) contributes from 51% to 42% of the increase in Q_M ~~QM~~ (ΔQ_M $\cancel{\Delta Q}$), with ~~the~~ this contribution decreasing with warming. The $\cancel{Q_L}$ ~~QL~~ contribution of Q_L to ΔQ_M $\cancel{\Delta Q}$ increases from 27 to 29% in response to warming, while that of LW* increases from 5 to 9%. The contributions of Q_S ~~QS~~ (~19%) and Q_R ~~QR~~ (~1%) are more constant across the warming spectrum (Figure 13f).

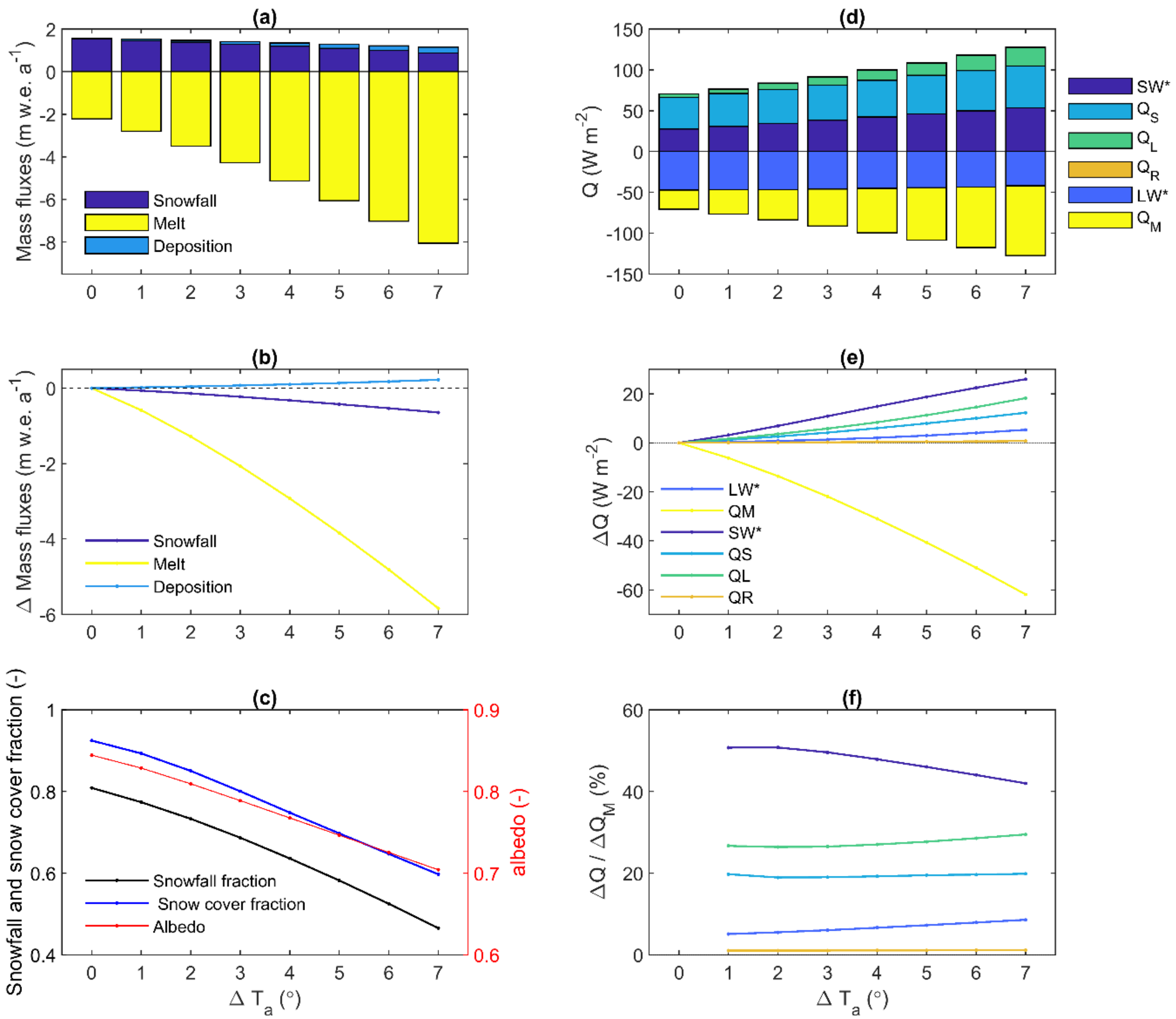

(a)
Mass fluxes (m w.e. a^{-1})
Snowfall
Melt
Deposition
(b)
Δ Mass fluxes (m w.e. a^{-1})
Snowfall
Melt
Deposition
(c)
Snowfall and snow cover fraction (-)
albedo (-)
Snowfall fraction
Snow cover fraction
Albedo
Δ T_a (°)
(d)
Q (W m^{-2})
SW*
Q_S
Q_L
Q_R
LW*
Q_M
(e)
ΔQ (W m^{-2})
LW*
QM
SW*
QS
QL
QR
(f)
ΔQ / ΔQ_M (%)
Δ T_a (°)

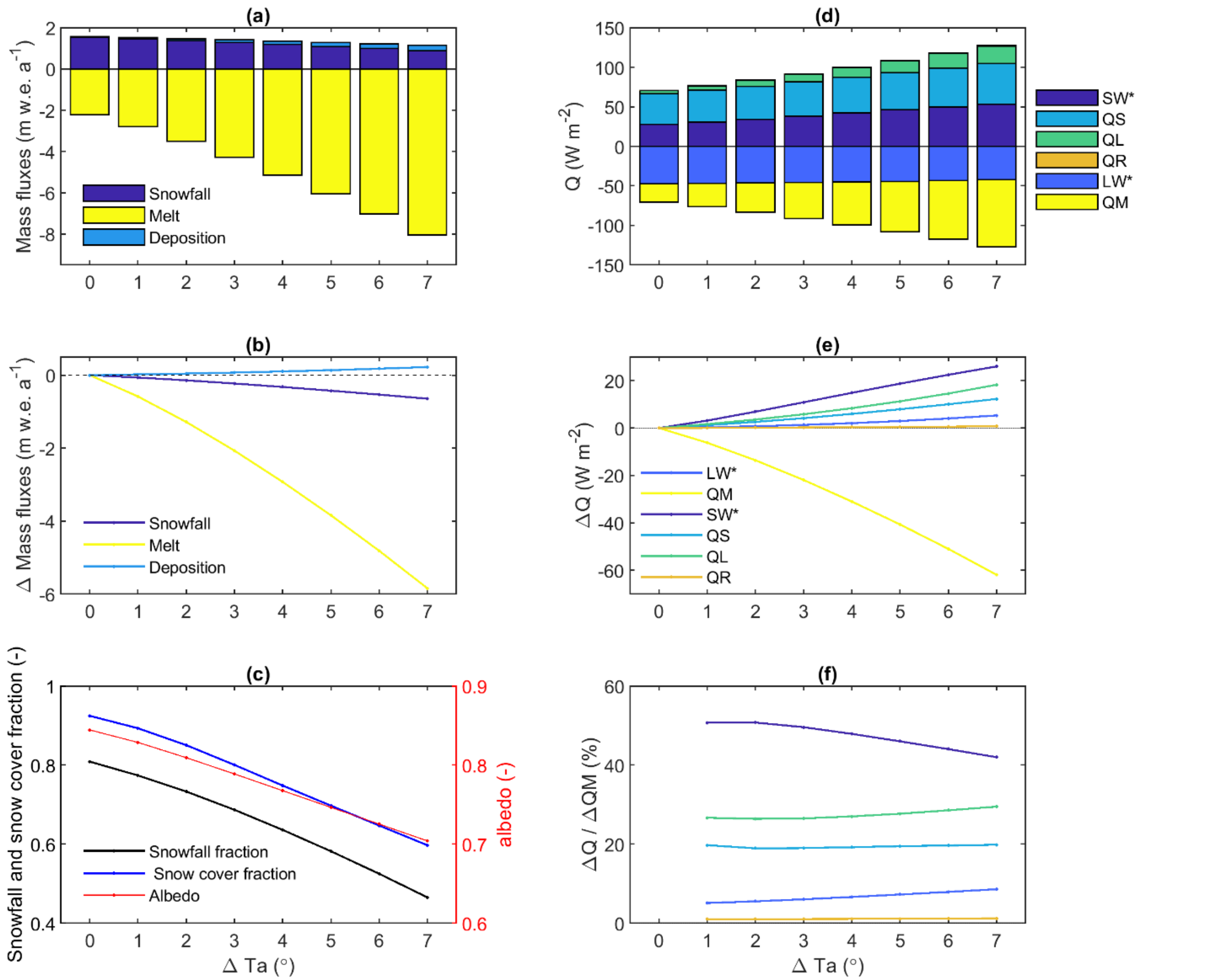

Figure 13. ~~**Static**~~ **Reference (2010) mass and energy balance sensitivity to changes in regional mean air temperature between 0 to 7 °C. (a) Annual m~~M~~ass balance; (b) changes in mass balance relative to baseline (ΔT_a ~~Ta~~ = 0); (c) changes in snowfall to total precipitation ratio, snow cover~~,~~ and albedo; (d) energy balance; (b) changes in energy balance relative to baseline (ΔT_a ~~Ta~~ = 0); (e) Changes in energy fluxes scaled by the changes in melt energy (Q_m). All fluxes and variables represent mean annual values averaged over the whole glacier surface and over the baseline 1981-2010 period with mean air temperature perturbed from 0 to 7 °C.**

The results in Figure 13 allow apportioning the mass balance sensitivity to warming to four different processes (Table 1): (i) atmospheric warming, which causes an increase in the temperature-dependent fluxes ($\Delta LW^* + \Delta Q_S$) and contributes on average 24.3% to the mass balance sensitivity to warming; (ii) a precipitation phase change feedback, which contributes 10.3%; (iii) an albedo feedback, which contributes 44%, and (iv) a humidity feedback which contributes 22.3%. While the contributions from atmospheric warming and the humidity feedback increase with the level of warming, the precipitation phase feedback remains constant, while the albedo feedback decreases over time (Table 1).

Table 1. Contribution of different processes to the sensitivity of glacier mass balance to warming from +1°C to +7°C.

Process~~Contribution to ΔB_a (%)~~	Equation	Relative contribution to ΔB_a +1°C (%)	+2°C (%)	+3°C (%)	+4°C (%)	+5°C (%)	+6°C (%)	+7°C (%)	**Mean (%)**
Atmospheric warming	$-(\Delta LW^* + \Delta Q_S)/(L_f \Delta B_a)$	23.0	22.7	23.3	24.0	24.9	25.7	26.5	**24.3**
Precipitation phase change	$\Delta P_S/\Delta B_a$	10.4	10.3	10.3	10.3	10.3	10.3	10.3	**10.3**
Albedo	$-\Delta SW^*/(L_f \Delta B_a)$	47.1	47.1	46.1	44.5	42.8	41.0	39.2	**44.0**
Humidity	$\left(\frac{-\Delta Q_L}{L_f} + \Delta S\right)/\Delta B_a$	21.6	21.4	21.5	21.9	22.5	23.2	24.0	**22.3**

L_f = latent heat of fusion, P_S = snowfall, S = deposition/condensation

5 Discussion

5.1 Suitability of NARR for model forcing

~~The present~~This study focused on reconstructing the mass balance of a glacier using a physically-based model constrained by a sparse set of glacio-meteorological data without calibration. This situation is common to many mountain glaciers of the world where logistical and financial constrains preclude continuous monitoring programs. In this context, the outputs of reanalysis ~~or numerical weather models~~products represent a~~n attractive~~ useful alternative for driving glaciological models. ~~The NAAR reanalysis product, with its high spatial (32 km) and temporal (3-hourly) resolution can provide accurate meteorological information, especially for 2 m temperature and 10 m wind in comparison with other global reanalysis datasets (Mesinger et al., 2006).~~ Several previous studies have used ~~NARR~~ reanalyses to force hydrological and glaciological models in mountainous region using ~~simple~~ statistical downscaling. Among the downscaling ~~While dynamical downscaling does not introduce additional uncertainties associated with statistical calibration, the technique is computationally intensive~~ ~~(Collier et al., 2013; Mölg and Kaser, 2011; Réveillet et al., 2020).~~strategies used, some did not rely on situ observations, such as such as the linear theory of orographic precipitation used by Jarosch et al. (2012) and Clarke et al. (2015) and the extrapolation to the glacier surface of the vertical structure of air temperature in reanalysis products ~~to the glacier surface~~ (Fiddes and Gruber, 2014; Jarosch et al., 2012). Hofer at al. (2010; 2012; 2015), on the other hand, used station-based downscaling and found that combining different types of reanalysis variables and spatial averaging of reanalyses gridcells~~points~~ led to superior downscaling performance. Earlier work by Radic and Hock (2006) used temperature and precipitation from ERA-40 reanalyses to force a mass balance model for Storglaciären, Sweden. They used bilinearly interpolation of the nine gridcells centered on the glacier and obtained good mass balance simulation results after correcting the ERA-40 temperature bias with a lapse rate tuned to optimise the mass balance simulation, but no correction on ERA-40 precipitation. Koppes et al (2011) also used a simple approach by regressing temperature and precipitation from the closest NCEP-NCAR reanalysis gridcell ~~point~~ against station data~~,~~ in Patagonia. The station-based scaling approach used in this study to correct biases in NARR is simple compared to station-free (e.g., Jarosch et al., 2012) or multivariate regression (Hofer et al., 2010) approaches, but is similar to the station-based methods used by Radic and Hock (2006) and Koppes et al. (2011). ~~(Jarosch et al., 2012{Clarke, 2015 #40}~~ ~~(Clarke et al., 2015; Ebrahimi and Marshall, 2016; Hofer et al., 2010) or dynamical downscaling (Arritt and Rummukainen, 2011; Erler et al., 2015; Giorgi, 2006). While dynamical downscaling does not introduce additional uncertainties associated with statistical calibration, the technique is computationally intensive (Mölg and Kaser, 2011). The quality of meteorological observations used for statistical downscaling, however, will determine the quality of the downscaling results, due to the necessary calibration step. In our study,~~ T~~t~~he comparison between NARR and station observations was reasonably good (r = 0.31-0.98) given the short AWS record used for comparison. ~~Even without downscaling~~T~~,~~ three variables (T_a ~~Ta~~, *RH*, *SW*↓~~in~~) showed ~~good~~ strong correlations (r~~R~~ ~~=>~~ 0.85-0.98) between NARR and AWS observations, and the simple scaling bias correction removed much of the biases present (Figure 3). Moreover, the cold bias in NARR air temperature was consistent with the elevation difference between the AWS and the NARR gridcell ~~point~~ and the local temperature lapse rate. The low bias and high correlation for NARR air temperature and relative humidity, and solar radiation ~~*SW*↓in~~ to a lesser extent (Figure 3)~~, (**Erreur ! Source du renvoi introuvable.Erreur ! Source du renvoi introuvable.**),~~ are consistent with previous findings from Trubilowicz et al. (2016) who showed that these variables agreed well with measured values at high-elevation stations in the southern Coast Mountains of British Columbia, Canada. Wind speed (*WS*) on Saskatchewan Glacier was however poorly represented (r = 0.37-0.38), most probably because thermal winds (katabatic and valley winds) are not represented at the coarse ~~32 ×~~ 32 km spatial resolution of the NARR ~~(Dadic et al., 2010)~~. Trubilowicz et al. (2016) also reported lower and site-dependent accuracy for NARR wind speeds. More sophisticated wind downscaling (e.g. Vionnet et al., 2021; Wagenbrenner et al., 2016) could help improve further modelling at this site and other upland icefield-outlet valley glacier settings.

The positive bias in NARR precipitation ~~appeared~~ was consistent with the higher elevation of the NARR grid point relative to the ~~homogenized~~ merged precipitation record (Figure 3)~~. (**Erreur ! Source du renvoi introuvable.Erreur ! Source du renvoi introuvable.**).~~ However, once the effect of the elevation difference ~~is~~ was corrected using the calibrated precipitation lapse rate (15.6% 100 m^{-1}), the NAAR ~~is~~ was found to underestimate observations by 10%. This is consistent with the recent study by Hunter et al. (2020) who showed that NARR underestimates precipitation in the mountain regions of British-Columbia, Canada. The NARR precipitation also correlated rather poorly with the off-glacier daily historical precipitation record (r~~R~~ = 0.30-0.31), showing that the daily variability in NARR precipitation is not well represented. Precipitation is notoriously more difficult to represent in reanalysis products, especially in complex terrain with steep orographic gradients and localized convective activity (Hofer et al., 2010; Mesinger et al., 2006). Ebrahimi and Marshall (2016) also reported that the NARR precipitation for ~~the~~ Haig Glacier, also in the Canadian Rocky Mountains, poorly represented~~s~~ the observed winter accumulation totals. Nevertheless, NARR precipitation has been found to be reliable at the monthly scale and to represent a useful input for hydrological modelling in North America generally (Chen and Brissette, 2017). Our results suggest this finding also applies for glaciological modelling, given that bias-correction is applied. The underestimation of precipitation in NARR combined with the positive bias in the raw NARR global radiation mostly explain the exaggerated mass loss simulated by the mass balance model when forced with the lapsed ~~biased~~ NARR, i.e., when only precipitation and temperature are ~~lapsed~~corrected to the elevation of the reference stations (Figure 8a). ~~elevations~~ More elaborate topographic corrections of solar radiation (Fiddes and Gruber, 2014) could improve the downscaling of NARR solar radiation in the absence of ground observations, but precipitations biases remain difficult to correct in this situation.

The choice of the NARR spatial interpolation method for downscaling to ~~the~~ stations had an overall ~~positive but~~ small effect on the comparison with station data (Figure 3). The bias and RMSE were slightly reduced when using bilinear interpolation of nine gridcells, compared with the nearest gridcell method. However, following bias correction against station data, both interpolation methods resulted in similar cumulative mass balance simulation (Figure 8a).

Despite the low correlation between NARR and AWS wind speed, the simulated ~~stake~~point mass balance in 2015 was ~~very~~not sensitive to using either the downscaled NARR or AWS wind speed ~~data~~forcings (Figure 8b, c). Replacing the downscaled NARR global radiation and relative humidity by their AWS counterparts had also a ~~small~~small effect on the model validation. Despite its strong correlation with AWS observations and low residual error after bias correction, the simulated point mass balance in 2015 was most sensitive to downscaled NARR air temperature (Figure 8b, c). This shows that air temperature have a large influence on the energy balance calculations, and that the simple scaling correction could probably be improved to better represent the effect of the glacier wind on air temperature on the glacier (Shea and Moore, 2010).

The approach used in this study could be extended to other reanalysis products, especially the new global ERA5 reanalyses (Hersbach and Dee, 2016). While its spatial resolution (0.25° ~28 km) is only slightly finer than NARR (0.30° ~32 km), ERA5 has an hourly resolution compared to the 3-hourly NARR resolution.

5.2 Model performance and parameter sensitivity

Despite the physical nature of the model, some ~~Despite some simplistic model~~ assumptions remain simplistic, such as~~,~~ ~~the primary one being~~ a constant precipitation lapse rate and ~~,~~spatially invariant ice albedo, aerodynamic roughness and wind speeds. Despite these limitations, the interannual variability in mass balance was relatively well simulated by the model, with NSE values of 0.83 to 0.91 for direct point observations (Figure 6). Point mass balance measurements with the glaciological method are affected by several uncertainties related to errors in ablation stake height measurements, stake self-drilling into the ice or firn and snow/firn density measurements (Zemp et al., 2013). Errors ~~in point measurements~~ can range from 0.14 ~~c~~m w.e. a^{-1} for ablation measurements on ice, 0.27 ~~c~~m w.e. a^{-1} for ablation measurements on firn and 0.21 ~~c~~m w.e. a^{-1} for snow measurements in the accumulation area (Thibert et al., 2008). The root-mean-squared-error (RMSE) on the simulated b_w ~~is~~ was 0.24~~.2~~ ~~c~~m w.e. a^{-1}- (median relative error of 15%) – on the same order as the typical measurement error for snow and firn. ~~.~~RMSE values, however, ~~are~~ were higher than typical measurement errors for b_s (0.87 ~~.0~~ ~~c~~m w.e. a^{-1}, relative error = 22%) and b_a (0.77~~.6~~ ~~c~~m w.e. a^{-1}, relative error = 24%), due in part to the restricted number of available observations for validation (Figure 6). The reconstructed mass balance also compared favorably against the independent geodetic estimates (~~c.f.~~see sect. 4.5 and~~,~~ Figure 8). The simulated cumulative mass loss (-26.79 m w.e.) was close to the geodetic estimate (-25.59 ± 8.44 m w.e)~~s~~, despite the large uncertainties in the geodetic balance introduced from 2000 onward due to vertical uncertainties in the SRTM DEM. The long-term consistency between geodetic and modelled mass balance gives further confidence that the bias-corrected NARR forcings do not suffer from systematic biases. ~~were and~~

The model sensitivity to uncertain model parameters showed that the simulated mass balance was most sensitive to uncertainties in the precipitation lapse rate, followed by the ice aerodynamic roughness, while the sensitivity to the snow aerodynamic roughness and ice albedo were lower. This demonstrates that the precipitation lapse rate must be carefully evaluated using ancillary meteorological data, which can be difficult in regions with no permanent weather station network nearby, a conclusion also reached in the Himalayas by Immerzeel et al. (2014) ~~.~~ As the model only accepted a constant lapse rate, we used a value (15.6 ±4%) representative of the period during which most of the snow accumulation occurs, i.e. when the glacier toe is above the zero-degree isotherm (Supplementary Figure S1). Including shoulder months (April and September) which have mixed precipitations would slightly lower this gradient. The extrapolation of the gradient beyond the highest weather station (2000 m) is also a common but hazardous practice, and validation against snow courses (Avanzi et al., 2021) or winter mass balance surveys (Carturan et al., 2012) offers a way to check the validity of the gradient. The gradient used in this study resulted in accurate simulations of winter mass balance (Figure 6a), which strengthens our confidence in extrapolating the gradient to the glacier. However, there were no observations beyond 2900 m to constrain the gradient further. The area of the glacier above 2900 m represents only 8.8 % of the total area, so extrapolation errors in this unsampled area would have a small impact on the glacier-wide mass balance. Further development of the model should also consider including a time-varying precipitation lapse rates, as it was shown for example that the lapse rates was smaller during the 2016 dry year (Figure 6a).

A high sensitivity to the ice aerodynamic roughness has been reported in several studies (e.g. Brock et al., 2000; Hock and Holmgren, 1996; MacDonell et al., 2013; Munro, 1989). It remains one of the most challenging parameters to constrain in glacier mass balance models, and the assumption of a spatially and temporally constant z_0 value is a simplistic representation of reality (Fitzpatrick et al., 2019). This parameter is indeed often calibrated in the absence of direct observations (Hock, 2005). In this study, observations from the nearby Peyto Glacier allowed using a representative value which yielded good results; however the uncertainty range in the values reported by Munro (1989) (± 1 mm) was sufficient to induce a ± 17% error in the simulated cumulative balance (Figure 8d). Advances in deriving aerodynamic roughness from remote sensing could help in the future to improve the calculation of turbulent fluxes in distributed glacier models (Chambers et al., 2020; Fitzpatrick et al., 2019; Smith et al., 2020). The use of remotely sensed albedo maps also contributed to constrain a representative value for ice albedo (~~c.f.~~~~see~~see Sect. 3.3.2) ~~and~~ but the simulated mass balance was not very sensitive to the uncertainty around this estimate (Figure 8d). Nevertheless, only an average value was used, when in fact significant heterogeneity was found within the ablation zone (~~supplementary material~~Supplementary Material). Decreasing ice albedo can occur over the course of the melt season due to impurities of geogenic origin concentrating at the surface (Cuffey and Paterson, 2010), cryoconite development (Takeuchi et al., 2001) and more discrete events not taken into account in the model, such as algal mat development (Lutz et al., 2014) or wildfires that bring black carbon and ash onto the glacier and decrease the albedo (Marshall and Miller, 2020). Long-term darkening has also been observed on glaciers of the European Alps, which questions the use of fixed albedo values in long historical and future mass balance simulations (Oerlemans et al., 2009). Further efforts could look to assimilate such remotely sensed albedo maps within distributed models.

5.3 Impact of glacier recession on mass balance

The multi-temporal DEMs used in the study allowed quantifying the impact of glacier elevation changes on long-term mass balance (Figure 7). The ~~dynamic~~ conventional mass balance simulation with the multitemporal DEMs showed a maximum difference of ~~in cumulative mass balance of~~ ~1.5 m w.e., or 5.6% of the 1979 reference ~~static~~ cumulative balance. This is a small difference overall, which shows that glacier recession has had a minor impact on the mass balance of Saskatchewan Glacier. This is expected~~,~~ for this setting in particular, since the glacier margin is at the bottom of the occupying valley and glacier retreat has occurred over a restricted ~~altitude~~ elevation range – thereby limiting negative feedback effects between glacier retreat and mass balance. ~~-~~This study has focused on the static climate sensitivity of mass balance, ~~ignoring~~ which ignores future dynamical feedbacks. Static, or ~~'~~reference~~'~~ mass balances calculated over a constant glacier hypsometry have been proposed to be better suited for climatic interpretation (Elsberg et al., 2001; Harrison et al., 2009). But from a hydrological perspective, future glacier retreat towards higher elevations would mitigate an increasing portion of the simulated mass loss, gradually increasing the difference between the ~~static~~ reference (2010) ~~surface)~~ and ~~dynamical~~ conventional mass balance, and progressively decreasing the volume of meltwater released annually (Huss and Hock, 2018; Huss et al., 2012). An increase in dynamical adjustments effects on mass balance ~~is~~ was already visible on Saskatchewan Glacier from 2000 onward (Figure 7a). ~~(Figure 8Figure 7a~~

5.4 Energy balance regime

The simulated glacier-wide energy balance regime of Saskatchewan Glacier showed that energy inputs are dominated by the sensible heat flux, flowed by net radiation and latent heat fluxes. This is different than commonly reported for mid-latitude glaciers in continental climates, where net radiation dominates over turbulent fluxes (e.g., see compilation by Smith et al., 2020). However, most studies reporting energy flux partitioning relied on summer observations in the ablation zones of glaciers. Hence, the often-reported high contribution of net radiation to melting energy is biased by the season (values are commonly reported for July/August – when net radiation is high), and to the ablation zone of glaciers, where most micrometeorological studies have been done and where again net radiation is higher due the lower albedo. Year-round, glacier-wide values are rarely published, and only available from distributed energy balance models. On Saskatchewan Glacier, the glacier-wide contribution to melting energy was 26.1% for net radiation, 57% for sensible heat (Q_S) and 16.9% for the latent heat flux (Q_L) during the ablation period (July-August). The energy partitioning was quite different when looking at the ablation zone only, with net radiation contributing 57%, Q_S 32%, and Q_L 11% of the melting energy at the AWS, midway up the ablation zone. The lower glacier-wide contribution of net radiation reflects the fact that much of Saskatchewan Glacier is covered in snow, and later firn, in summer. This is also accordance with Klok and Oerlemans (2002), who showed that net radiation dominates over Q_S in the lower part of the glacier, while Q_S dominates in the higher part of Morteratschgletscher Glacier, Switzerland. Studies that reported glacier-wide energy partitioning include Storglaciären in Sweden (summer net radiation: 38-57%, Q_S: 42% Q_L: up to 17%) (Hock and Holmgren, 2005), Brewster glacier, New-Zealand (annual net radiation: 45%, Q_S + Q_L: 52%, turbulent fluxes dominating in summer) (Anderson et al., 2010), Haut Glacier d'Arolla, Switzerland (summer net radiation : 82%, Q_S: 25%) (Arnold et al., 1996), Donjek range glaciers in the Yukon, Canada (summer net radiation : 60-83%, Q_S: 20-45%, Q_L: -4 to -9%) (MacDougall and Flowers, 2011), and Haig Glacier in Alberta, Canada (summer net radiation: 70%, Q_S: 30%) (Marshall, 2014). Point measurements in late June/early July on nearby Peyto Glacier showed that net radiation contributed 63% and 42% of the melt energy over ice and snow surfaces, respectively, while sensible heat contributed 34% (ice) and 50% (snow) (Munro, 2006). Hence, the contribution of sensible and latent heat flux to summer melting on Saskatchewan Glacier is higher than common values for mid latitude temperate glaciers with a continental climate, and closer to that encountered for glaciers in more humid climates (Anderson et al., 2010; Smith et al., 2020). The contribution of turbulent fluxes to melting energy was however not so different from the earlier measurements reported by Munro (2006) at Peyto: 32-57% at Saskatchewan vs. 34-50% at Peyto for Q_S, and 11-17% vs. 3-9% for Q_L. The higher contribution of turbulent fluxes to melting on Saskatchewan Glacier, together with a simulated balance ratio (BR = 3.10, see Sect. 4.4.1) that is closer to values from more humid climates (Rea, 2009), may thus reflect the locally wetter and cloudier climate, and high accumulation rates, resulting from the efficient interception of moist polar maritime air masses from the west by the high and extensive plateau of the Columbia Icefield (Demuth and Horne, 2018; Tennant and Menounos, 2013). This 'icefield weather' frequently wraps the Columbia icefield in clouds while surrounding valleys are cloud-free.

~~5.4~~5.5 Climate sensitivity

The simulated mass balance sensitivity to a +1°C warming was -0.65 m w.e. °C^{-1}. This value is comparable to other mid-latitude glaciers: -0.60 m w.e. °C^{-1} for the Illecillewaet Glacier in the Selkirk Mountains of British Columbia (Hirose and Marshall, 2013), -0.66 m w.e. °C^{-1} for the Haig Glacier in the Canadian Rocky Mountains (Ebrahimi and Marshall, 2016), -0.65 ±0.05 m w.e. °C^{-1} for small (<0.5 km^2) glaciers in Switzerland (Huss and Fischer, 2016), -0.60 m w.e. °C^{-1} for the larger Morteratschgletscher, Switzerland (Klok and Oerlemans, 2004), and -0.61 m w.e. °C^{-1} for Storglaciären, Sweden (Hock et al., 2007). Higher sensitivities are found in more humid climates, e.g. -0.86 m w.e. °C^{-1} for the South Cascade Glacier, Washington (Anslow et al., 2008) and up to -2.0 m w.e. °C^{-1} on Brewster Glacier, New Zealand (Anderson et al., 2010), and lower sensitivities in drier climate, e.g. -0.44 m w.e. °C^{-1} on Urumqi River Glacier No.1 in the Chinese Tien Shan (Che et al., 2019)~~(Gascoin et al., 2019)~~. Earlier work by Braithwaite (2006), Oerlemans and Fortuin (1992) and Oerlemans (2001) showed that the mass balance sensitivity to temperature scales with mean annual precipitation, due to larger albedo and precipitation phase feedbacks and longer melt seasons on glaciers in wetter climates.

We ~~find~~ found that the albedo feedback is the main contributor (mean = 44%) to the temperature sensitivity of mass balance on Saskatchewan Glacier ~~the sensitivity of Saskatchewan Glacier mass balance to warming is dominated by increased melting (~90%) while the precipitation phase feedback only accounts for ~10%. We further find that the albedo feedback represents the main contributor to the temperature sensitivity for the Saskatchewan Glacier~~(Figure 13). Increases in net shortwave radiation caused by a reducing snow cover and ensuing decreased glacier albedo account for 39~~42~~-47~~51~~ % of the increase in melt energy across the various warming scenarios (Table 1). A similar finding was reported on Haig Glacier by Ebrahimi and Marshall (2016), who found that introducing albedo feedbacks doubles the net energy sensitivity to warming. This value (44%) is significantly high, but less than the 80% reported recently by Johnson and Rupper (2020) for the summer-accumulation type Chhota Shigri Glacier in High Mountain Asia. As shown by Fujita (2008) , higher sensitivities are found for glaciers located in a summer-precipitation climate, where albedo feedbacks on ablation are stronger, than for glaciers located within a winter-precipitation climate.

Atmospheric warming itself contributed only 24.3% to the mass balance sensitivity to temperature across all warming scenarios, through sensible heat and longwave radiation transfer to the glacier (Table 1). ~~For the Saskatchewan Glacier,~~ A~~a~~ significant air humidity feedback was also found, with latent heat fluxes representing ~~contributing~~ an average of 22~~27-29~~% of the temperature sensitivity across all warming scenarios ~~the increased melting under warmer temperatures~~. Keeping the relative humidity constant under warming scenarios may be plausible for the high elevation Columbia Icefield. The icefield receives moist air masses from the British Columbia interior and the Pacific Ocean uplifted onto the icefield, as the region is subject to upslope conditions derived from convergent upper air masses as low-pressure systems spin by south of the region. Other glaciers subjected to subsiding air masses could experience drier weather in the future, which would decrease their melt sensitivity to warming (Ebrahimi and Marshall, 2016). The large contribution of latent heat fluxes to melting under warming scenarios points to the necessity of considering changes in specific air humidity when simulating glacier melt under future climates. This conclusion is in line with the recent findings by Harpold et al. (2018) who showed that atmospheric humidity plays a critical role in local energy balance and snowpack ablation under warmer climates, with latent and longwave radiant fluxes cooling the snowpack under dry conditions and warming it under humid conditions. The precipitation phase feedback, on the other hand, contributed the remaining 10% of the mass balance temperature sensitivity (Table 1).

The mass balance sensitivity of Saskatchewan Glacier to a ±10% change in precipitation under the current temperature regime was 1.01 (unitless; m w.e. of mass change per m w.e. of precipitation change). A value of 1 would occur if all precipitation were snowfall and there were no albedo feedbacks on B_a ~~(Oerlemans, 2001)~~. The snowfall fraction is 0.81 u~~U~~nder the present climate~~, the snowfall fraction is 0.81~~ (Figure 13c), and ~~thereby~~ therefore the albedo feedback on ablation contributes ~~0.20~~19% to the mass balance sensitivity to precipitation. With the mean annual precipitation on the glacier being 1880 mm for the 1981-2010 reference period, the maximum +20% precipitation increase projected from ensemble climate scenarios for the end of the century would add a maximum of 0.4 m w.e. a^{-1} if all new precipitation falls as snow,~~,~~ which is small compared to the mean temperature sensitivity of -0.65 m w.e. °C^{-1}. As such, precipitation increases can only buffer up to +0.5 °C^{-1} of warming on Saskatchewan Glacier. As warming causes snowfall to shift to rainfall at a rate of ∼~~-~~5% °C^{-1} (Figure 13c), ~~this limits~~ the buffering effect of a +20% ~~increasing~~ increase precipitation would decrease accordingly, ~~under warming scenarios, and accounts for~~ i.e. from 0.29~~1~~ m w.e. a^{-1} for a +1°C warming to 0.17 m w.e a^{-1}~~°C^{-1}~~ for a +7°C warming~~of the mean temperature sensitivity~~.

6 Conclusions

Despite their physical basis, energy-balance models often struggle to replicate mass-balance observations, due to the difficulty in constraining their numerous parameters and obtaining reliable meteorological forcings (Gabbi et al., 2014; Réveillet et al., 2018). Our study showed that a physically-based, distributed mass balance model forced by regional reanalysis data can adequately reproduce the recent and long-term evolution of glacier mass balance when forcings and key model parameters are judiciously constrained with available observations and ancillary data. This is a key requirement for the effective application of such models, since parameters from distributed energy balance models dot not necessarily transfer well between sites (MacDougall and Flowers, 2011). While reanalysis data can provide realistic climate forcings for glacier models, bias-correction with in situ observations remains ~~desirable~~ideal when such measurements are available. Adopting this approach, however, ~~requires~~ entails a significant amount of work, which would be hard to implement at the mountain range scale. While ancillary data were key to constraining key model parameters, model sensitivity analyses showed that the precipitation gradient and the aerodynamic roughness lengths were sensitive parameters that need to be carefully prescribed.

The reconstructed mass balance of Saskatchewan Glacier shows a cumulative loss of -26.79 m w.e. over the period 1979-2016, in good agreement with independent geodetic estimates (-25.59 ± 8.44 m w.e). Glacier retreat has had a small impact overall on glacier mass balance, but the effect of dynamical adjustment has been increasing in recent years. Climate sensitivity experiments showed that future changes in precipitation would have a small impact on glacier mass-balance, while the temperature sensitivity increases with warming, from -0.65 to -0.93 m w.e. °C^{-1}. Increased melting accounted for 90% of the temperature sensitivity while precipitation phase feedbacks accounted for 10%. ~~Roughly~~ Close to half (44%) ~~half~~ of the ~~melt~~ mass balance response to warming was driven by reductions in glacier albedo as the snow cover on the glacier thins and recedes earlier in response to warming (positive albedo feedback).~~,~~ Atmospheric warming directly accounted for about one quarter (24%) of the mas balance sensitivity to warming. ~~while about one quarter~~The remaining ~~of the~~ mass balance response to warming was driven by latent heat energy gains (positive humidity feedback) and conversion of snowfall to rainfall (positive precipitation phase feedback).~~.~~ Our study therefore underlines the key role of albedo and air humidity in modulating the response of winter-accumulation type mountain glaciers and upland icefield-outlet glacier settings to climate.

7 Code availability

The glacier mass balance model code is available at https://regine.github.io/meltmodel/

8 Data availability

Downscaled NARR forcings, geodetic mass balance estimates and reconstructed mass balance are available from the corresponding author.

9 Author contribution

Conceptualisation: CK, MND. Formal analysis: ~~OL,~~ CK, OL; Supervision: CK; Data Curation: MND, BM; Writing – original draft preparation: OL, CK; Writing – review & editing: CK, OL, MND, BM.

10 Competing interests

The authors declare that they have no conflict of interest.

11 Acknowledgements

CK was supported and funded by the Fonds de recherche du Québec – Nature et Technologies, the National Sciences and Engineering Research Council of Canada and the Canada Research Chair Program. MND was supported and funded by Natural Resources Canada's Climate Change Geoscience Program and the NSERC-CCAR Changing Cold Regions Network (CCRN). The authors thank Steve Bertollo, Eric Courtin, May Guan, Gabriel Meunier-Cardinal and Anthony Pothier-Champagne for assisting with field data collection. Jasper and Banff National Parks of Canada are thanked for supporting this work under Permit JNP-2010-4694.

12 References

Anderson, B., Mackintosh, A., Stumm, D., George, L., Kerr, T., Winter-Billington, A., and Fitzsimons, S.: Climate sensitivity of a high-precipitation glacier in New Zealand, Journal of Glaciology, 56, 114-128, 2010.

Anderson, S. and Radić, V.: Identification of local water resource vulnerability to rapid deglaciation in Alberta, Nature Climate Change, 10, 933-938, 2020.

Anslow, F. S., Hostetler, S., Bidlake, W. R., and Clark, P. U.: Distributed energy balance modeling of South Cascade Glacier, Washington and assessment of model uncertainty, Journal of Geophysical Research: Earth Surface, 113, 2008.

Arnold, N., Willis, I., Sharp, M., Richards, K., and Lawson, W.: A distributed surface energy-balance model for a small valley glacier. I. Development and testing for Haut Glacier d'Arolla, Valais, Switzerland, Journal of Glaciology, 42, 77-89, 1996.

Arnold, N. S., Rees, W. G., Hodson, A. J., and Kohler, J.: Topographic controls on the surface energy balance of a high Arctic valley glacier, Journal of Geophysical Research: Earth Surface, 111, 2006.

Avanzi, F., Ercolani, G., Gabellani, S., Cremonese, E., Pogliotti, P., Filippa, G., Morra di Cella, U., Ratto, S., Stevenin, H., Cauduro, M., and Juglair, S.: Learning about precipitation lapse rates from snow course data improves water balance modeling, Hydrol. Earth Syst. Sci., 25, 2109-2131, 2021.

Ayala, A., Pellicciotti, F., Peleg, N., and Burlando, P.: Melt and surface sublimation across a glacier in a dry environment: distributed energy-balance modelling of Juncal Norte Glacier, Chile, Journal of Glaciology, 63, 803-822, 2017.

Aygün, O., Kinnard, C., and Campeau, S.: Impacts of climate change on the hydrology of northern midlatitude cold regions, Prog. Phys. Geogr.: Earth Environ., 44, 338-375, 2020a.

Aygün, O., Kinnard, C., Campeau, S., and Krogh, S. A.: Shifting Hydrological Processes in a Canadian Agroforested Catchment due to a Warmer and Wetter Climate, Water, 12, 739, 2020b.

Barnett, T. P., Adam, J. C., and Lettenmaier, D. P.: Potential impacts of a warming climate on water availability in snow-dominated regions, Nature, 438, 303-309, 2005.

Benn, D. and Evans, D. J.: Glaciers and glaciation, Routledge, 2014.

Bonekamp, P. N., de Kok, R. J., Collier, E., and Immerzeel, W. W.: Contrasting meteorological drivers of the glacier mass balance between the Karakoram and central Himalaya, Frontiers in Earth Science, 7, 107, 2019.

Braithwaite, R. J.: Measuring and Modelling the Mass Balance of Glaciers for Global Change. In: Glacier Science and Environmental Change, 2006.

Braithwaite, R. J. and Raper, S. C.: Glaciers and their contribution to sea level change, Physics and Chemistry of the Earth, Parts A/B/C, 27, 1445-1454, 2002.

Brock, B. W., Willis, I. C., and Sharp, M. J.: Measurement and parameterization of aerodynamic roughness length variations at Haut Glacier d'Arolla, Switzerland, Journal of Glaciology, 52, 281-297, 2006.

Brock, B. W., Willis, I. C., Sharp, M. J., and Arnold, N. S.: Modelling seasonal and spatial variations in the surface energy balance of Haut Glacier d'Arolla, Switzerland, Annals of Glaciology, 31, 53-62, 2000.

Bukovsky, M. S. and Karoly, D. J.: A Brief Evaluation of Precipitation from the North American Regional Reanalysis, Journal of Hydrometeorology, 8, 837-846, 2007.

Carenzo, M., Pellicciotti, F., Rimkus, S., and Burlando, P.: Assessing the transferability and robustness of an enhanced temperature-index glacier-melt model, Journal of Glaciology, 55, 258-274, 2009.

Carturan, L., Dalla Fontana, G., and Borga, M.: Estimation of winter precipitation in a high-altitude catchment of the Eastern Italian Alps: validation by means of glacier mass balance observations, Geogr. Fis. Din. Quat, 35, 37-48, 2012.

Chambers, J. R., Smith, M. W., Quincey, D. J., Carrivick, J. L., Ross, A. N., and James, M. R.: Glacial Aerodynamic Roughness Estimates: Uncertainty, Sensitivity, and Precision in Field Measurements, Journal of Geophysical Research: Earth Surface, 125, e2019JF005167, 2020.

Che, Y., Zhang, M., Li, Z., Wei, Y., Nan, Z., Li, H., Wang, S., and Su, B.: Energy balance model of mass balance and its sensitivity to meteorological variability on Urumqi River Glacier No.1 in the Chinese Tien Shan, Scientific Reports, 9, 13958, 2019.

Chen, J. and Brissette, F. P.: Hydrological modelling using proxies for gauged precipitation and temperature, Hydrological Processes, 31, 3881-3897, 2017.

Clarke, G. K., Jarosch, A. H., Anslow, F. S., Radić, V., and Menounos, B.: Projected deglaciation of western Canada in the twenty-first century, Nature Geoscience, 2015. 2015.

Cofiño, A., Cano, R., Sordo, C., Primo, C., and Gutiérrez, J.: MeteoLab, a software library for Matlab>= 5 implementing statistical and data mining techniques for Meteorology, Applied Meteorology Group. Universidad de Cantabria, 2004. 2004.

Cogley, J. G.: Geodetic and direct mass-balance measurements: comparison and joint analysis, Annals of Glaciology, 50, 96-100, 2009.

Cogley, J. G. and Adams, W.: Mass balance of glaciers other than the ice sheets, Journal of Glaciology, 44, 315-325, 1998.

Comeau, L. E. L., Pietroniro, A., and Demuth, M. N.: Glacier contribution to the North and South Saskatchewan Rivers, Hydrological Processes, 23, 2640-2653, 2009.

Conway, J. P., Helgason, W. D., Pomeroy, J. W., and Sicart, J. E.: Icefield Breezes: Mesoscale Diurnal Circulation in the Atmospheric Boundary Layer Over an Outlet of the Columbia Icefield, Canadian Rockies, Journal of Geophysical Research: Atmospheres, 126, e2020JD034225, 2021.

Cuffey, K. M. and Paterson, W. S. B.: The physics of glaciers, Butterworth-Heinemann/Elsevier, Burlington, Mass., 2010.

Demuth, M.: Glaciers/Mountains as Monuments. In: 2018 State of the Mountains Report, Volume 1, Changing Glaciers, Changing Rivers, L, P., Z, R., and D, K. (Eds.), Alpine Club of Canada, 2018.

Demuth, M. and Horne, G.: Decadal-centenary glacier mass changes and their variability, Jasper National Park, Alberta, including the Columbia Icefield region. Geological Survey of Canada Open File 8229, 2018.

Demuth, M., Munro, D., and Young, G. (Eds.): Peyto Glacier: One Century of Science, National Hydrology Research Institute Science Report 8, Environment Canada, Natural Resources Canada and Alberta Environment, 2006.

Demuth, M. and Pietroniro, A.: The impact of climate change on the glaciers of the Canadian Rocky Mountain eastern slopes and implications for water resource adaptation in the Canadian prairies., 162 pp., 2002.

Déry, S. J., Stahl, K., Moore, R., Whitfield, P., Menounos, B., and Burford, J. E.: Detection of runoff timing changes in pluvial, nival, and glacial rivers of western Canada, Water Resources Research, 45, 2009.

Dittmer, K.: Changing streamflow on Columbia basin tribal lands—climate change and salmon, Climatic Change, 120, 627-641, 2013.
Ebrahimi, S. and Marshall, S. J.: Surface energy balance sensitivity to meteorological variability on Haig Glacier, Canadian Rocky Mountains, The Cryosphere, 10, 2799-2819, 2016.
Ednie, M., Demuth, M., and Shepherd, B.: Mass balance of the Athabasca and Saskatchewan sectors of the Columbia Icefield, Alberta for 2015 and 2016. Geological Survey of Canada, 2017.
Elsberg, D. H., Harrison, W. D., Echelmeyer, K. A., and Krimmel, R. M.: Quantifying the effects of climate and surface change on glacier mass balance, Journal of Glaciology, 47, 649-658, 2001.
Engelhardt, M., Schuler, T. V., and Andreassen, L. M.: Sensitivities of glacier mass balance and runoff to climate perturbations in Norway, Annals of Glaciology, 56, 79-88, 2015.
Escanilla-Minchel, R., Alcayaga, H., Soto-Alvarez, M., Kinnard, C., and Urrutia, R.: Evaluation of the Impact of Climate Change on Runoff Generation in an Andean Glacier Watershed, Water, 12, 3547, 2020.
Fiddes, J. and Gruber, S.: TopoSCALE v. 1.0: downscaling gridded climate data in complex terrain, Geoscientific Model Development, 7, 387-405, 2014.
Fitzpatrick, N., Radić, V., and Menounos, B.: A multi-season investigation of glacier surface roughness lengths through in situ and remote observation, The Cryosphere, 13, 1051-1071, 2019.
Fujita, K.: Effect of precipitation seasonality on climatic sensitivity of glacier mass balance, Earth and Planetary Science Letters, 276, 14-19, 2008.
Gabbi, J., Carenzo, M., Pellicciotti, F., Bauder, A., and Funk, M.: A comparison of empirical and physically based glacier surface melt models for long-term simulations of glacier response, Journal of Glaciology, 60, 1140-1154, 2014.
Gerbaux, M., Genthon, C., Etchevers, P., Vincent, C., and Dedieu, J.: Surface mass balance of glaciers in the French Alps: distributed modeling and sensitivity to climate change, Journal of Glaciology, 51, 561-572, 2005.
Grah, O. and Beaulieu, J.: The effect of climate change on glacier ablation and baseflow support in the Nooksack River basin and implications on Pacific salmonid species protection and recovery, Climatic Change, 120, 657-670, 2013.
Harpold, A. A. and Brooks, P. D.: Humidity determines snowpack ablation under a warming climate, Proceedings of the National Academy of Sciences, 115, 1215-1220, 2018.
Harrison, W., Cox, L., Hock, R., March, R., and Pettit, E.: Implications for the dynamic health of a glacier from comparison of conventional and reference-surface balances, Annals of Glaciology, 50, 25-30, 2009.
Hersbach, H. and Dee, D.: ERA5 reanalysis is in production, ECMWF newsletter, 147, 5-6, 2016.
Hirose, J. and Marshall, S.: Glacier meltwater contributions and glaciometeorological regime of the Illecillewaet River Basin, British Columbia, Canada, Atmosphere-ocean, 51, 416-435, 2013.
Hock, R.: A distributed temperature-index ice-and snowmelt model including potential direct solar radiation, Journal of Glaciology, 45, 101-111, 1999.
Hock, R.: Glacier melt: a review of processes and their modelling, Progress in Physical Geography: Earth and Environment, 29, 362-391, 2005.
Hock, R.: Temperature index melt modelling in mountain areas, Journal of Hydrology, 282, 104-115, 2003.
Hock, R., Bliss, A., Marzeion, B., Giesen, R. H., Hirabayashi, Y., Huss, M., Radić, V., and Slangen, A. B.: GlacierMIP–A model intercomparison of global-scale glacier mass-balance models and projections, Journal of Glaciology, 65, 453-467, 2019.
Hock, R. and Holmgren, B.: A distributed surface energy-balance model for complex topography and its application to Storglaciären, Sweden, Journal of Glaciology, 51, 25-36, 2005.
Hock, R. and Holmgren, B.: Some aspects of energy balance and ablation of Storglaciären, northern Sweden, Geografiska Annaler: Series A, Physical Geography, 78, 121-131, 1996.
Hock, R. and Huss, M.: Chapter 9 - Glaciers and climate change. In: Climate Change (Third Edition), Letcher, T. M. (Ed.), Elsevier, 2021.
Hock, R., Radić, V., and De Woul, M.: Climate sensitivity of Storglaciären, Sweden: an intercomparison of mass-balance models using ERA-40 re-analysis and regional climate model data, Annals of Glaciology, 46, 342-348, 2007.
Hofer, M., Marzeion, B., and Mölg, T.: Comparing the skill of different reanalyses and their ensembles as predictors for daily air temperature on a glaciated mountain (Peru), Clim. Dyn., 39, 1969-1980, 2012.

Hofer, M., Marzeion, B., and Mölg, T.: A statistical downscaling method for daily air temperature in data-sparse, glaciated mountain environments, Geosci. Model Dev., 8, 579-593, 2015.
Hofer, M., Mölg, T., Marzeion, B., and Kaser, G.: Empirical-statistical downscaling of reanalysis data to high-resolution air temperature and specific humidity above a glacier surface (Cordillera Blanca, Peru), Journal of Geophysical Research: Atmospheres, 115, 2010.
Hunter, C., Moore, R. D., and McKendry, I.: Evaluation of the North American Regional Reanalysis (NARR) precipitation fields in a topographically complex domain, Hydrological Sciences Journal, 65, 786-799, 2020.
Huss, M., Bookhagen, B., Huggel, C., Jacobsen, D., Bradley, R. S., Clague, J. J., Vuille, M., Buytaert, W., Cayan, D. R., Greenwood, G., Mark, B. G., Milner, A. M., Weingartner, R., and Winder, M.: Toward mountains without permanent snow and ice, Earth's Future, 5, 418-435, 2017.
Huss, M. and Fischer, M.: Sensitivity of Very Small Glaciers in the Swiss Alps to Future Climate Change, Frontiers in Earth Science, 4, 2016.
Huss, M. and Hock, R.: Global-scale hydrological response to future glacier mass loss, Nature Climate Change, 8, 135-140, 2018.
Huss, M. and Hock, R.: A new model for global glacier change and sea-level rise, Frontiers in Earth Science, 3, 2015.
Huss, M., Hock, R., Bauder, A., and Funk, M.: Conventional versus reference-surface mass balance, Journal of Glaciology, 58, 278-286, 2012.
Immerzeel, W. W., Petersen, L., Ragettli, S., and Pellicciotti, F.: The importance of observed gradients of air temperature and precipitation for modeling runoff from a glacierized watershed in the Nepalese Himalayas, Water Resources Research, 50, 2212-2226, 2014.
IPCC: 2013: Climate Change 2013: The Physical Science Basis. Contribution of Working Group I to the Fifth Assessment Report of the Intergovernmental Panel on Climate Change [Stocker, T.F., D. Qin, G.-K. Plattner, M. Tignor, S.K. Allen, J. Boschung, A. Nauels, Y. Xia, V. Bex and P.M. Midgley (eds.)]. Cambridge University Press, Cambridge, United Kingdom and New York, NY, USA, 1535 pp., Cambridge university press, 2013.
Jarosch, A. H., Anslow, F. S., and Clarke, G. K. C.: High-resolution precipitation and temperature downscaling for glacier models, Clim. Dyn., 38, 391-409, 2012.
Jennings, K. S., Winchell, T. S., Livneh, B., and Molotch, N. P.: Spatial variation of the rain–snow temperature threshold across the Northern Hemisphere, Nature Communications, 9, 1148, 2018.
Johnson, E. and Rupper, S.: An Examination of Physical Processes That Trigger the Albedo-Feedback on Glacier Surfaces and Implications for Regional Glacier Mass Balance Across High Mountain Asia, Frontiers in Earth Science, 8, 2020.
Jones, P. A.: Cloud-Cover Distributions and Correlations, Journal of Applied Meteorology and Climatology, 31, 732-741, 1992.
Kinnard, C., Ginot, P., Surazakov, A., MacDonell, S., Nicholson, L., Patris, N., Rabatel, A., Rivera, A., and Squeo, F. A.: Mass Balance and Climate History of a High-Altitude Glacier, Desert Andes of Chile, Frontiers in Earth Science, 8, 2020.
Klok, E. and Oerlemans, J.: Model study of the spatial distribution of the energy and mass balance of Morteratschgletscher, Switzerland, Journal of Glaciology, 48, 505-518, 2002.
Klok, E. and Oerlemans, J.: Modelled climate sensitivity of the mass balance of Morteratschgletscher and its dependence on albedo parameterization, International Journal of Climatology: A Journal of the Royal Meteorological Society, 24, 231-245, 2004.
Knap, W., Reijmer, C., and Oerlemans, J.: Narrowband to broadband conversion of Landsat TM glacier albedos, International Journal of Remote Sensing, 20, 2091-2110, 1999.
Koppes, M., Conway, H., Rasmussen, L. A., and Chernos, M.: Deriving mass balance and calving variations from reanalysis data and sparse observations, Glaciar San Rafael, northern Patagonia, 1950–2005, The Cryosphere, 5, 791-808, 2011.
Kronenberg, M., Barandun, M., Hoelzle, M., Huss, M., Farinotti, D., Azisov, E., Usubaliev, R., Gafurov, A., Petrakov, D., and Kääb, A.: Mass-balance reconstruction for Glacier No. 354, Tien Shan, from 2003 to 2014, Annals of Glaciology, 57, 92-102, 2016.
Lutz, S., Anesio, A. M., Jorge Villar, S. E., and Benning, L. G.: Variations of algal communities cause darkening of a Greenland glacier, FEMS Microbiology Ecology, 89, 402-414, 2014.

MacDonell, S., Kinnard, C., Mölg, T., Nicholson, L., and Abermann, J.: Meteorological drivers of ablation processes on a cold glacier in the semi-arid Andes of Chile, The Cryosphere, 7, 1513-1526, 2013.

MacDougall, A. H. and Flowers, G. E.: Spatial and Temporal Transferability of a Distributed Energy-Balance Glacier Melt Model, Journal of Climate, 24, 1480-1498, 2011.

Machguth, H., Paul, F., Kotlarski, S., and Hoelzle, M.: Calculating distributed glacier mass balance for the Swiss Alps from regional climate model output: A methodical description and interpretation of the results, Journal of Geophysical Research: Atmospheres, 114, 2009.

Machguth, H., Purves, R. S., Oerlemans, J., Hoelzle, M., and Paul, F.: Exploring uncertainty in glacier mass balance modelling with Monte Carlo simulation, The Cryosphere, 2, 191-204, 2008.

Marshall, S. J.: Meltwater run-off from Haig Glacier, Canadian Rocky Mountains, 2002–2013, Hydrol. Earth Syst. Sci., 18, 5181-5200, 2014.

Marshall, S. J. and Miller, K.: Seasonal and interannual variability of melt-season albedo at Haig Glacier, Canadian Rocky Mountains, The Cryosphere, 14, 3249-3267, 2020.

Marshall, S. J., White, E. C., Demuth, M. N., Bolch, T., Wheate, R., Menounos, B., Beedle, M. J., and Shea, J. M.: Glacier water resources on the eastern slopes of the Canadian Rocky Mountains, Canadian Water Resources Journal, 36, 109-134, 2011.

Marzeion, B., Jarosch, A. H., and Hofer, M.: Past and future sea-level change from the surface mass balance of glaciers, The Cryosphere, 6, 1295-1322, 2012.

Menounos, B., Hugonnet, R., Shean, D., Gardner, A., Howat, I., Berthier, E., Pelto, B., Tennant, C., Shea, J., and Noh, M. J.: Heterogeneous changes in western North American glaciers linked to decadal variability in zonal wind strength, Geophysical Research Letters, 46, 200-209, 2019.

Mesinger, F., DiMego, G., Kalnay, E., Mitchell, K., Shafran, P. C., Ebisuzaki, W., Jović, D., Woollen, J., Rogers, E., and Berbery, E. H.: North American regional reanalysis, Bulletin of the American Meteorological Society, 87, 343-360, 2006.

Milner, A. M., Khamis, K., Battin, T. J., Brittain, J. E., Barrand, N. E., Füreder, L., Cauvy-Fraunié, S., Gíslason, G. M., Jacobsen, D., Hannah, D. M., Hodson, A. J., Hood, E., Lencioni, V., Ólafsson, J. S., Robinson, C. T., Tranter, M., and Brown, L. E.: Glacier shrinkage driving global changes in downstream systems, Proceedings of the National Academy of Sciences, 114, 9770-9778, 2017.

Mölg, T., Cullen, N. J., Hardy, D. R., Kaser, G., and Klok, L.: Mass balance of a slope glacier on Kilimanjaro and its sensitivity to climate, International Journal of Climatology: A Journal of the Royal Meteorological Society, 28, 881-892, 2008.

Mölg, T., Großhauser, M., Hemp, A., Hofer, M., and Marzeion, B.: Limited forcing of glacier loss through land-cover change on Kilimanjaro, Nature Climate Change, 2, 254, 2012.

Moore, R., Fleming, S., Menounos, B., Wheate, R., Fountain, A., Stahl, K., Holm, K., and Jakob, M.: Glacier change in western North America: influences on hydrology, geomorphic hazards and water quality, Hydrological Processes: An International Journal, 23, 42-61, 2009.

Munro, D. S.: Linking the weather to glacier hydrology and mass balance at Peyto glacier, 2006. 2006.

Munro, D. S.: Surface roughness and bulk heat transfer on a glacier: comparison with eddy correlation, Journal of Glaciology, 35, 343-348, 1989.

Nash, J. E. and Sutcliffe, J. V.: River flow forecasting through conceptual models part I—A discussion of principles, Journal of hydrology, 10, 282-290, 1970.

Oerlemans, J.: Glaciers and climate change, CRC Press, 2001.

Oerlemans, J., Anderson, B., Hubbard, A., Huybrechts, P., Johannesson, T., Knap, W., Schmeits, M., Stroeven, A., Van de Wal, R., and Wallinga, J.: Modelling the response of glaciers to climate warming, Climate dynamics, 14, 267-274, 1998.

Oerlemans, J., Giesen, R., and Van den Broeke, M.: Retreating alpine glaciers: increased melt rates due to accumulation of dust (Vadret da Morteratsch, Switzerland), Journal of Glaciology, 55, 729-736, 2009.

Oerlemans, J. and Knap, W.: A 1 year record of global radiation and albedo in the ablation zone of Morteratschgletscher, Switzerland, Journal of Glaciology, 44, 231-238, 1998.

Oke, T.: Boundary layer climates, 0415043190, 1987.

Orsolini, Y., Wegmann, M., Dutra, E., Liu, B., Balsamo, G., Yang, K., de Rosnay, P., Zhu, C., Wang, W., Senan, R., and Arduini, G.: Evaluation of snow depth and snow cover over the Tibetan Plateau in global reanalyses using in situ and satellite remote sensing observations, The Cryosphere, 13, 2221-2239, 2019.
Østby, T. I., Schuler, T., Hagen, J. O. M., Hock, R., Kohler, J., and Reijmer, C.: Diagnosing the decline in climatic mass balance of glaciers in Svalbard over 1957-2014, The Cryosphere, 11, 191-215, 2017.
Paul, F. and Kotlarski, S.: Forcing a Distributed Glacier Mass Balance Model with the Regional Climate Model REMO. Part II: Downscaling Strategy and Results for Two Swiss Glaciers, J. Clim., 23, 1607-1620, 2010.
Petersen, L. and Pellicciotti, F.: Spatial and temporal variability of air temperature on a melting glacier: Atmospheric controls, extrapolation methods and their effect on melt modeling, Juncal Norte Glacier, Chile, Journal of Geophysical Research: Atmospheres, 116, 2011.
Petts, G., Gurnell, A., and Milner, A.: Eco-hydrology: new opportunities for research on glacier-fed rivers, Peyto Glacier: One Century of Science, 8, 255-275, 2006.
Plüss, C. and Ohmura, A.: Longwave Radiation on Snow-Covered Mountainous Surfaces, Journal of Applied Meteorology, 36, 818-824, 1997.
Prudhomme, C., Wilby, R. L., Crooks, S., Kay, A. L., and Reynard, N. S.: Scenario-neutral approach to climate change impact studies: application to flood risk, Journal of Hydrology, 390, 198-209, 2010.
Radić, V., Bliss, A., Beedlow, A. C., Hock, R., Miles, E., and Cogley, J. G.: Regional and global projections of twenty-first century glacier mass changes in response to climate scenarios from global climate models, Climate Dynamics, 42, 37-58, 2014.
Radić, V. and Hock, R.: Modeling future glacier mass balance and volume changes using ERA-40 reanalysis and climate models: A sensitivity study at Storglaciären, Sweden, Journal of Geophysical Research: Earth Surface, 111, 2006.
Radic, V., Tessema, M., Menounos, B., and Fitzpatrick, N.: Evaluation of Dynamically Downscaled Near-surface Mass and Energy Fluxes for Three Mountain Glaciers, British Columbia, Canada, 2018.
Rea, B. R.: Defining modern day Area-Altitude Balance Ratios (AABRs) and their use in glacier-climate reconstructions, Quaternary Science Reviews, 28, 237-248, 2009.
Réveillet, M., Six, D., Vincent, C., Rabatel, A., Dumont, M., Lafaysse, M., Morin, S., Vionnet, V., and Litt, M.: Relative performance of empirical and physical models in assessing the seasonal and annual glacier surface mass balance of Saint-Sorlin Glacier (French Alps), The Cryosphere, 12, 1367-1386, 2018.
Réveillet, M., Vincent, C., Six, D., and Rabatel, A.: Which empirical model is best suited to simulate glacier mass balances?, Journal of Glaciology, 63, 39-54, 2017.
Rupper, S. and Roe, G.: Glacier Changes and Regional Climate: A Mass and Energy Balance Approach, J. Clim., 21, 5384-5401, 2008.
Rye, C. J., Arnold, N. S., Willis, I. C., and Kohler, J.: Modeling the surface mass balance of a high Arctic glacier using the ERA-40 reanalysis, Journal of Geophysical Research: Earth Surface, 115, 2010.
Sandford, R. W.: The Columbia Icefield–3rd Edition, Rocky Mountain Books Ltd, 2016.
Schindler, D. W. and Donahue, W. F.: An impending water crisis in Canada's western prairie provinces, Proceedings of the National Academy of Sciences, 103, 7210-7216, 2006.
Shea, J. M. and Moore, R. D.: Prediction of spatially distributed regional-scale fields of air temperature and vapor pressure over mountain glaciers, Journal of Geophysical Research: Atmospheres, 115, 2010.
Shean, D. E., Alexandrov, O., Moratto, Z. M., Smith, B. E., Joughin, I. R., Porter, C., and Morin, P.: An automated, open-source pipeline for mass production of digital elevation models (DEMs) from very-high-resolution commercial stereo satellite imagery, ISPRS Journal of Photogrammetry and Remote Sensing, 116, 101-117, 2016.
Smith, T., Smith, M. W., Chambers, J. R., Sailer, R., Nicholson, L., Mertes, J., Quincey, D. J., Carrivick, J. L., and Stiperski, I.: A scale-dependent model to represent changing aerodynamic roughness of ablating glacier ice based on repeat topographic surveys, Journal of Glaciology, 66, 950-964, 2020.
Sunako, S., Fujita, K., Sakai, A., and Kayastha, R. B.: Mass balance of Trambau Glacier, Rolwaling region, Nepal Himalaya: in-situ observations, long-term reconstruction and mass-balance sensitivity, Journal of Glaciology, 65, 605-616, 2019.

Takeuchi, N., Kohshima, S., and Seko, K.: Structure, formation, and darkening process of albedo-reducing material (cryoconite) on a Himalayan glacier: a granular algal mat growing on the glacier, Arctic, Antarctic, and Alpine Research, 33, 115-122, 2001.

Tennant, C. and Menounos, B.: Glacier change of the Columbia Icefield, Canadian Rocky Mountains, 1919–2009, Journal of Glaciology, 59, 671-686, 2013.

Teutschbein, C. and Seibert, J.: Bias correction of regional climate model simulations for hydrological climate-change impact studies: Review and evaluation of different methods, Journal of Hydrology, 456-457, 12-29, 2012.

Thibert, E., Blanc, R., Vincent, C., and Eckert, N.: Glaciological and volumetric mass-balance measurements: error analysis over 51 years for Glacier de Sarennes, French Alps, Journal of Glaciology, 54, 522-532, 2008.

Trouet, V. and Van Oldenborgh, G. J.: KNMI Climate Explorer: a web-based research tool for high-resolution paleoclimatology, Tree-Ring Research, 69, 3-13, 2013.

Trubilowicz, J. W., Shea, J. M., Jost, G., and Moore, R. D.: Suitability of North American Regional Reanalysis (NARR) output for hydrologic modelling and analysis in mountainous terrain, Hydrological Processes, 30, 2332-2347, 2016.

Vionnet, V., Marsh, C. B., Menounos, B., Gascoin, S., Wayand, N. E., Shea, J., Mukherjee, K., and Pomeroy, J. W.: Multi-scale snowdrift-permitting modelling of mountain snowpack, The Cryosphere, 15, 743-769, 2021.

Wagenbrenner, N. S., Forthofer, J. M., Lamb, B. K., Shannon, K. S., and Butler, B. W.: Downscaling surface wind predictions from numerical weather prediction models in complex terrain with WindNinja, Atmos. Chem. Phys., 16, 5229-5241, 2016.

Wetterhall, F., Pappenberger, F., He, Y., Freer, J., and Cloke, H. L.: Conditioning model output statistics of regional climate model precipitation on circulation patterns, Nonlin. Processes Geophys., 19, 623-633, 2012.

Wheler, B. A.: Glacier melt modelling in the Donjek Range, St. Elias Mountains, Yukon Territory, 2009. Dept. of Earth Sciences-Simon Fraser University, 2009.

Yang, M., Li, Z., Anjum, M. N., Zhang, X., Gao, Y., and Xu, C.: On the importance of subsurface heat flux for estimating the mass balance of alpine glaciers, Global Planet. Change, 207, 103651, 2021.

Yang, W., Yao, T., Guo, X., Zhu, M., Li, S., and Kattel, D. B.: Mass balance of a maritime glacier on the southeast Tibetan Plateau and its climatic sensitivity, Journal of Geophysical Research: Atmospheres, 118, 9579-9594, 2013.

Zemp, M., Hoelzle, M., and Haeberli, W.: Six decades of glacier mass-balance observations: a review of the worldwide monitoring network, Annals of Glaciology, 50, 101-111, 2009.

Zemp, M., Thibert, E., Huss, M., Stumm, D., Denby, C. R., Nuth, C., Nussbaumer, S., Moholdt, G., Mercer, A., and Mayer, C.: Uncertainties and re-analysis of glacier mass balance measurements, The Cryosphere Discussions, 7, 789-839, 2013.

Zolles, T., Maussion, F., Galos, S. P., Gurgiser, W., and Nicholson, L.: Robust uncertainty assessment of the spatio-temporal transferability of glacier mass and energy balance models, The Cryosphere, 13, 469-489, 2019.